

Linking Morphology and Multi-Physical Transport in Structured Electrodes

Thèse N° 9394

Présentée le 5 avril 2019

à la Faculté des sciences et techniques de l'ingénieur
Laboratoire de la science et de l'ingénierie de l'énergie renouvelable
Programme doctoral en énergie

pour l'obtention du grade de Docteur ès Sciences

par

Silvan SUTER

Acceptée sur proposition du jury

Prof. J. Luterbacher, président du jury
Prof. S. Haussener, directrice de thèse
Prof. A. Rothschild, rapporteur
Prof. R. Marschall, rapporteur
Prof. R. Buonsanti, rapporteuse

2019

Acknowledgements

First and foremost, I would like to express my sincere gratitude to my advisor Prof. Sophia Haussener for her continuous support throughout my academic path starting from my Master's Thesis to my Ph.D. studies. Her goal-oriented work, persistence and positive attitude were very motivating for me to pursue my research. Thank you for all the advice, discussions, brainstorming and openness for new ideas.

I would like to thank Marco Cantoni from the Centre Interdisciplinaire de Microscopie Électronique (CIME, EPFL) for the advice, support, and training regarding the nanotomography. Without his expertise and the countless hours that we spent together in front of the microscope, the acquired 3D data would not have reached this high level of quality. Also, being part of the evaluation process for a new FIB-SEM machine was a valuable learning experience. A special thanks to Danièle Laub for the training in the sample preparation.

I am grateful for the access to the world-class clean room facilities at the Center of MicroNanotechnology (CMI, EPFL). The advice, training, and problem-solving support were always professional and helpful. The fruitful discussions and brainstorming with Cyrille Hibert catalyzed the innovative process that led to the template-stripping fabrication process flows.

I would like to thank Ludmilla Steier for the collaboration on the hematite deposition at the Laboratory of Photonics and Interfaces (LPI, EPFL). The ability to use the spray pyrolysis and ALD setup was crucial for the progress of my research. The same applies to the most recent collaborations with Daniel Grave and Anton Tsyganok from the Israel Institute of Technology (Technion) with their expertise on PLD hematite deposition.

Individual thanks go to Simone Pokrant, Yogi Surendranath and Youngmin Yoon for the in-depth discussions at meetings and conferences.

A sincere thanks to Diana Moreno García and Rafael Graf for their outstanding work during their Master's Thesis and Semester Project, respectively.

A special thanks go to my colleagues at the Laboratory of Renewable Energy Science and Engineering for all the stimulating discussions and for creating a motivating work environment. The regular lunch breaks and recreational activities with my colleagues balanced out all the hard work. Many thanks go especially to my colleague Yannick Gaudy for all our exchanges that truly helped my research progress.

An dieser Stelle möchte ich auch meiner Familie und meinen Freunden danken. Meine Geschwister waren schon immer Vorbilder für mich in den verschiedensten Bereichen, und ich konnte von jedem von euch etwas lernen und abschauen. Einen innigen Dank gilt meinen Eltern, die mich in jeder Lebenslage und bei allen Entscheidungen unterstützt haben. Eure Hingabe hat mir in meinem Leben soviel ermöglicht und dafür danke ich euch.

I would like to take the chance to express my heartfelt gratitude to my wife, Jacqueline. You inspire my life and the way I see the world. Thank you for your patience and continuous support. You motivated me when I needed words of encouragement and shared a laugh in moments of joy. You always followed my research with curiosity and took the time to read through my thesis in order to give suggestions and advice. Thank you!

Abstract

Motivated to advance the renewable energy production and diversify the technologies for storable energy carriers, my work is concentrated on the characterization and the optimization of electrode morphologies applicable in photoelectrochemical water-splitting and electrochemical carbon dioxide reduction. The geometry of the electrode-electrolyte interface affects the multi-physical transport properties in a chemical energy conversion device. The structuring of the solid-liquid interface can improve the light management and assist to overcome the limiting charge transport in a semiconductor electrode. However, it also has implications on the species concentration, the pH and the diffusive mass transport in the electrolyte. Characterizing and quantifying the link between the morphology and those multi-physical transport processes are fundamental to design electrode geometries that enhance the energy conversion efficiency.

In order to study photoelectrodes with complex and anisotropic morphologies, accurate representations of the 3D electrode structures are required. A coupled experimental-numerical approach was developed to digitalize the morphology of two photoelectrodes, a particle-based lanthanum titanium oxynitride (LTON) and a ‘cauliflower-like’ structured hematite (α -Fe₂O₃) electrode, using high-resolution FIB-SEM tomography. Key morphological parameters were extracted from the digital model.

Simulations using the exact geometry of the LTON electrode investigated the correlation between the morphology and the multi-physical transport properties in a photoelectrochemical water-splitting device. Light absorption, local current densities and ion concentration distributions in the electrolyte have been computed to link material bulk properties to the incident-light-to-charge-transfer-rate-conversion by morphology-dependent parameters.

The developed numerical tools were adapted for electrochemical carbon dioxide reduction on an inverse-opal silver electrode, where concentration gradients played a more significant role. The species mass transport in the electrolyte determined the selectivity of the competing surface reactions, where mesoporous structuring of the electrode favored the carbon dioxide reduction. The calculations reproduced experimental results from the literature, supporting and quantifying the intrinsic pH-dependency of the unwanted water-splitting reaction.

Lastly, the light management in thin film metal oxide photoelectrodes for water-splitting was optimized by numerical simulations of electromagnetic wave propagation. Wedge patterns of thin film hematite with a reflective backing layer on a flexible polyimide substrate were used to enhance the light absorption by resonant and geometric light trapping. In order to fabricate the patterned thin film photoelectrodes with precise control over the microstructure, an experimental platform was developed based on a template-stripping method.

In conclusion, the methods developed in this work have been proven to characterize and quantify the effects of the morphology on multi-physical transport. Furthermore, design guidelines on the morphology and the operating conditions were derived from the numerical results in order to optimize the electrode performance. Novel electrode architectures were proposed to enhance the reaction selectivity in mesoporous electrodes for the CO₂ reduction and improve the light trapping in thin film water-splitting photoelectrodes.

Keywords: Photoelectrochemical water-splitting, Electrochemical CO₂ reduction, Morphology, FIB-SEM tomography, Pore-level simulation, Electromagnetic wave propagation, Mass transport, Design guidelines, Template-stripping, Light trapping

Zusammenfassung

Motiviert, die Produktion erneuerbarer Energien voranzutreiben und die Technologien für speicherbare Energieträger zu diversifizieren, konzentriert sich meine Arbeit auf die Charakterisierung und Optimierung von Elektrodenmorphologien, die bei der photoelektrochemischen Wasserspaltung und elektrochemischen Kohlendioxidreduktion anwendbar sind. Die Geometrie der Elektroden-Elektrolyt-Grenzfläche beeinflusst die multiphysikalischen Transporteigenschaften in einer electrochemischen Zelle. Die Strukturierung der Elektrodenoberfläche kann das Lichtmanagement verbessern und helfen, den begrenzten Ladungstransport in einer Halbleiterelektrode zu überwinden. Es hat aber auch Auswirkungen auf die Konzentration der chemischen Spezies, den pH-Wert und den diffusiven Massentransport im Elektrolyten. Die Charakterisierung und Quantifizierung des Zusammenhangs zwischen der Morphologie und diesen multiphysikalischen Transportprozessen ist grundlegend für das Design von Elektrodengeometrien, die die Effizienz der Energieumwandlung verbessern.

Um Photoelektroden mit komplexen und anisotropen Morphologien zu untersuchen, sind genaue Darstellungen der 3D-Elektrodenstrukturen erforderlich. Ein gekoppelter experimentell-numerischer Ansatz wurde entwickelt, um die Morphologie von zwei Photoelektroden, einem partikelbasierten Lanthan-Titanoxinitrid (LTON) und einer "blumenkohlartig" strukturierten Hämatitelektrode ($\alpha\text{-Fe}_2\text{O}_3$), mittels hochauflösender FIB-SEM-Tomographie zu digitalisieren. Die wichtigsten morphologischen Parameter wurden aus dem digitalen Modell extrahiert.

Simulationen mit der genauen Geometrie der LTON-Elektrode untersuchten den Zusammenhang zwischen der Morphologie und den multiphysikalischen Transporteigenschaften

in einer photoelektrochemischen Zelle. Lichtabsorption, lokale Stromdichten und Ionenkonzentrationsverteilungen im Elektrolyten wurden berechnet, um die Materialeigenschaften und die Leistungsfähigkeit der Photoelektrode durch morphologische Parameter zu verknüpfen.

Die entwickelten numerischen Werkzeuge wurden für die Simulation von elektrochemischer Kohlendioxidreduktion an einer inversen opalen Silberelektrode angepasst, wobei Konzentrationsgradienten eine bedeutendere Rolle spielen. Der Massentransport im Elektrolyten bestimmte die Selektivität der konkurrierenden Oberflächenreaktionen, wobei die mesoporöse Strukturierung der Elektrode die Kohlendioxidreduktion begünstigt. Die Berechnungen reproduzierten experimentelle Ergebnisse aus der Literatur und quantifizierten die intrinsische pH-Abhängigkeit der unerwünschten Wasserspaltungsreaktion.

Schließlich wurde durch numerische Simulationen von elektromagnetischen Wellen das Lichtmanagement in Dünnschicht-Metalloxid-Halbleitern für die Wasserspaltung optimiert. Keilmuster aus einem flexiblen Polyimidsubstrat mit dünnem Hämatit auf einer reflektierenden Rückschicht wurden verwendet um die Lichtabsorption zu verbessern. Um die strukturierten Dünnschichtphotoelektroden mit präziser Steuerung der Mikrostruktur herzustellen, wurde eine experimentelle Plattform auf der Basis eines Template-Stripping Verfahrens entwickelt.

Abschließend ist festzustellen, dass die in dieser Arbeit entwickelten Methoden erwiesenermaßen zur Charakterisierung und Quantifizierung von den Auswirkungen der Morphologie auf den multiphysikalischen Transport beitragen. Darüber hinaus wurden aus den numerischen Ergebnissen Designrichtlinien zur Morphologie und den Betriebsbedingungen abgeleitet, um die Elektrodenleistung zu optimieren. Neue Elektrodenarchitekturen wurden vorgeschlagen, um die Reaktionsselektivität in mesoporösen Elektroden für die CO₂-Reduktion zu erhöhen und die Lichtabsorption in wasserspaltenden Dünnschicht-Fotoelektroden zu verbessern.

Schlüsselwörter: Photoelektrochemisches Wasserspalten, Elektrochemische CO₂-Reduktion, Morphologie, FIB-SEM-Tomographie, Pore-Level-Simulation, Elektromagnetische Wellenausbreitung, Massentransport, Designrichtlinien, Template-Stripping, Light Trapping

Table of Contents

Acknowledgements	i
Abstract	iii
Zusammenfassung	v
Table of Contents	vii
List of Figures	xi
List of Tables	xxi
List of Symbols	xxiii
1 Introduction	1
2 Quantitative Structural Analysis of Morphologically Complex Electrodes	9
2.1 Introduction	9
2.2 Digitalization of the Morphology	11
2.2.1 Materials and Sample Preparation	11
2.2.2 FIB-SEM Nanotomography	13
2.2.3 Digital Reconstruction	14
2.3 Methodology for the Morphological Characterization	19
2.3.1 Volume Fraction Profile	19
2.3.2 Surface Area	19
2.3.3 Size Distributions	19

Table of Contents

2.3.4 Particle Properties	20
2.3.5 Nano-Pore Characterization	21
2.4 Results and Discussion	22
2.4.1 Mesoscopic Structural Characterization	22
2.4.2 Feature Characterization on Multiple Scales	27
2.5 Conclusions	34
2.6 References	36
3 Linking Morphology and Multi-Physical Transport in LTON Photoanodes	39
3.1 Introduction	39
3.2 Morphology and Representative Volumes	41
3.3 Governing Equations and Methodology	43
3.3.1 Electron-Hole Pair Generation Rate	44
3.3.2 Local Current Density	45
3.3.3 Mass Transport	46
3.4 Results and Discussion	49
3.4.1 Light Absorption and Local Current Density	49
3.4.2 Mass Transport and Local Species Concentrations	51
3.4.3 Tortuosity	56
3.5 Conclusions	58
3.6 References	60
4 Optimizing Reaction Selectivity by the Mesostructuring of Silver Catalysts	63
4.1 Introduction	63
4.2 Model Description and Governing Equations	66
4.3 Results and Discussion	71
4.3.1 Empirical Parameters and Model Validation	71
4.3.2 Local Current Densities and Species Concentrations	75
4.3.3 Pore Size vs. Film Thickness	76

4.3.4 Additional Diffusion Layer	80
4.4 Conclusions	84
4.5 References	86
5 Implementing Light Trapping on Thin Film, Mesostructured Fe₂O₃ Photoanodes	89
5.1 Introduction	89
5.2 Resonant and Geometric Light Trapping in Thin Films on Wedge Structures	92
5.2.1 Model Description and Governing Equations	92
5.2.2 Results and Discussion	99
5.3 Fabrication of Patterned, Thin Film Photoanode through Template-Stripping	111
5.3.1 Process Flow	111
5.3.2 Choice of Materials	113
5.3.3 Experimental Methods	114
5.3.4 Characterization of Fabricated Electrodes	119
5.3.5 Improvements	123
5.4 Conclusions	125
5.5 References	127
6 Conclusions and Prospects	131
Curriculum Vitae	139

List of Figures

- Figure 2.1 SEM images of the two analyzed photoelectrodes. (a) Hematite ($\alpha\text{-Fe}_2\text{O}_3$) was deposited on an FTO glass by atmospheric pressure chemical vapor deposition. The image was reprinted with permission from reference [7]. (b) The LaTiO_2N particles were stacked on an FTO glass by electrophoretic deposition, followed by dip coating to establish TiO_2 necking bonds between the particles..... 12
- Figure 2.2 Scheme of the FIB-SEM tomography. The sample is embedded in epoxy as a structural support medium and to define a clear contrast between the semiconductor and the void phase. The close-up circle shows the V-shaped alignment grooves in the Pt layer, which run perpendicular to the cross-sections. The sample is covered by gold to reduce charging effects for the electron beam. The ion beam and electron beam column are at an angle of 52° . The ion beam mills perpendicular to the sample surface to expose cross-section by cross-section. The electron beam scans the cross-sections continuously, acquiring one image per cross-section. 13
- Figure 2.3 (a) Close-up of a cross-section image after the registration process. Air bubbles in the epoxy formed on the LTON surface or in the small channels between the particles. (b) The same cross-section image after eliminating the air bubbles. Also, the TiO_2 necking phase was identified and colored in yellow. (c) The final stage after the segmentation process. The three phases are separated in white = LTON, yellow = TiO_2 and black = void. (d) Identification and 3D rendering of all separated TiO_2 necking bonds in a subsection of the measured domain. Connected TiO_2 phases were given the same color. 16

List of Figures

- Figure 2.4 3D renderings of the analyzed photoelectrode morphologies with close-up views on the first cross-sections of the acquired volumes. (a) The α -Fe₂O₃ photoanode was measured with an isotropic voxel edge size of 4 nm. (b) The resolution of the LTON photoanode was an isotropic voxel edge size of 8 nm. 18
- Figure 2.5 Scheme of triangular mesh generation using the marching cube algorithm. Three examples are shown for grey values 0 (black) and 255 (white). The algorithm was applied to data sets with continuous grey values between 0 and 255..... 19
- Figure 2.6 Volume fraction profiles through the normalized thickness of the photoelectrode films. The morphology of the α -Fe₂O₃ electrode was much denser than the LTON film. The purple curves show the LTON volume fraction without TiO₂ necking. The yellow curve shows the volume fraction of only the necking phase (TiO₂). The FTO substrate was located at $z=0$. The film thickness of the hematite sample was $t=652$ nm. The LTON sample was 7.568 μ m thick. 23
- Figure 2.7 (a) Surface area per flat area (roughness factor) and per solid volume for α -Fe₂O₃, and LTON. LTON (I): surface areas of nano-pores not connected to the bulk electrolyte were neglected, LTON (II): surface areas of LTON particles, neglecting the contributions of nano-pores, LTON (III): LTON particles without nano-pores and necking. The error bounds indicate a lower bound segmentation threshold (α -Fe₂O₃: 100, LTON: 78) and an upper bound segmentation threshold (α -Fe₂O₃: 150, LTON: 106), to quantify the effect of the uncertainty in the segmentation process. (b) Mesh density study of surface area calculations. For subsamples (500 x 500 x 500 voxels) of the LTON and LTON (II), the surface area per solid volume is shown for different mesh densities. 24
- Figure 2.8 Cumulative opening size distribution (left y-axis) and probability opening size distribution (right y-axis) of the semiconductor films. (a) α -Fe₂O₃ semiconducting phase (blue) and pore space (yellow). (b) LTON semiconducting phase with necking (violet), pore space (yellow), and TiO₂ necking phase without LTON phase (green). The TiO₂ probability opening size distribution has been scaled down by a factor of 5..... 26
- Figure 2.9 3D rendering of ellipsoids fitted into the particles of the LTON photoelectrode. Particles that crossed the boundary of the measured domain were not considered. The ellipsoids were used to characterize the LTON particles in the photoelectrode film..... 28
- Figure 2.10 LTON particle characterization based on ellipsoids. (a) Size distribution of the three ellipsoid diameters with lognormal distributions: $d_{s,mean}=272$ nm, $d_{s,SD}=88$ nm; $d_{i,mean}=932$ nm, $d_{i,SD}=427$ nm; $d_{l,mean}=1789$ nm, $d_{l,SD}=773$ nm. (b) Shape analysis of the computed

ellipsoids. The ellipsoids are divided into 4 classes based on the length of the intermediate diameter. The mean value shifts from prolate to oblate shapes for classes with larger d_i . Overall, the ratio d_s/d_l stays constant. Isolines for d_s/d_l are shown for the mean= $0.18 \pm \text{SD}$. (c) Particle volume distribution (volumes of the smallest box in which the ellipsoid fits). Lognormal distribution: mean = $0.521 \mu\text{m}^3$, SD= $0.544 \mu\text{m}^3$, median= $0.338 \mu\text{m}^3$. (d) Box surrounding an ellipsoid. Surface fractions of the correlated crystallographic planes integrated over all considered particles. (e) Particle orientation determined by the direction of the smallest diameter. Elevation angle= 90° : particle lies flat on the FTO glass, and elevation angle= 0° : particle stands upright relative to the FTO glass. The scatter plot demonstrates no trend of particle orientation as a function of x -position. 29

Figure 2.11 Results reprinted with permission from reference [27]. (a) (i) Scanning transmission electron microscopy (STEM) image of LTON particle, (ii) patterns measured by selected-area diffraction (SAD). (iii) simulated diffraction patterns in [100] direction. (b) (i) STEM image of particle viewed in [210] direction, (ii) SAD pattern, (iii) dimensions of a pore. (c) Projection of a typically-shaped monocrystalline LTON particle in [100] direction consisting of three unit cells in [001], two unit cells in [010] and two unit cells in [001] direction. Green are the La positions, blue are the O positions and orange are the N positions; the red are the Ti atoms. O and N share unit cell positions. The pore elongation direction [011] is shown. 31

Figure 2.12 (a) Rendering of an ellipsoid (blue) fitted into a LTON particle. Nano-pores within the ellipsoid were identified and labeled. The semi-axes correspond to crystallography directions of $x=[010]$, $y=[001]$, and $z=[100]$. An azimuth and an elevation angle of 0° corresponds to the direction of the x-axis. The pores in the network were separated using water-shedding and visualized with individual colors. (b) 2D histogram of the nano-pore orientations in 4 different LTON particles relative to the orientation of the hosting particle. Three crystallography directions are indicated. The nano-pores are most frequently elongated in the [011] direction. 33

Figure 3.1 (a) For the LTON electrode, a subvolume is representative with a volume larger than $64.176 \mu\text{m}^3$ (RV: width= $5.73 \mu\text{m}$, depth= $1.4 \mu\text{m}$). The aspect ratio of the volume width to the volume depth is 4:1, and the error threshold is $\pm 3\%$. For comparison, the RV study is shown for the $\alpha\text{-Fe}_2\text{O}_3$ film. (b) The volume fractions of three equally sized subsamples (1000 x 1000 x 1000 voxels) are compared to the volume fraction of the overall film. Subsample 1 represents the overall sample well with a mean absolute percentage deviation of 8% for the volume fraction distribution. 42

List of Figures

- Figure 3.2 Scheme showing the local current densities on the semiconductor-electrolyte interface for simulated back illumination. The species concentrations of OH⁻ ions are shown in the pore space between the LTON particles. The electrolyte is stagnant in the pore space and by a Sherwood correlation, the contributions of the hydrodynamic boundary layer in a flow cell setup is taken into account to correlate the intermediate concentration c_i to the bulk concentration c_{bulk} 43
- Figure 3.3 Calculated absorption coefficient for LTON, based on measurements and corrected by the solid volume fraction profile. 45
- Figure 3.4 An intermediate concentration c_i was set as a top boundary condition. The side walls had symmetry boundary conditions and the bottom, which was covered by FTO had a no-flux boundary condition. The calculated local current density was applied as a reactant sink boundary condition onto the electrolyte-semiconductor interface. The boundary flux was given as a step function. For $c_{\text{Boundary}} > 0$, the reactant sink rate was equal to the charge flux calculated by the generation rate for a boundary concentration. For $c_{\text{Boundary}} = 0$, the sink rate became zero. 48
- Figure 3.5 (a) Calculated generation rates for front and back illuminations integrated over all the discretized columns in x- and y-direction. The generation rates for the measured, wavelength-dependent absorption coefficient is shown in a green dotted line for front and back illumination. The mean deviation from the exact profile to a constant, wavelength-averaged absorption coefficient of $1.4 \cdot 10^4 \text{ cm}^{-1}$ is 1.1% and 1.6% for front and back illumination, respectively. The profiles for an additional 4 constant absorption coefficients are shown. (b) Local current density distribution for front and back illumination with constant, wavelength-dependent absorption coefficients. 50
- Figure 3.6 Simulated values for the absorbed-light-to-charge-transfer-conversion (ALCC) as a function of the intermediate concentration and the diffusion coefficient for front and back illumination. Two sets of parameters for front and back illumination could fit Equation (3.9) to the simulated values. 52
- Figure 3.7 Simulation values and fit of ALCC vs. intermediate concentration for different, wavelength-averaged absorption coefficients: (a) front illumination and (b) back illumination. For increasing absorption coefficients, the curves merge asymptotically, as the generation rate profile, and therefore the ALCC, is only dependent on the morphology. 53
- Figure 3.8 (a) The ALCC correlated to the bulk pH for different flow regimes of a flow cell water splitting device with NaOH as an electrolyte. The bulk pH, for which the mass transport

through the macroscopic concentration boundary layer begins to be limiting, is indicated with a vertical dotted line. (b) The surface fraction of local surface concentrations for a given bulk pH and a flow regime of $Re=4$ 54

Figure 3.9 The surface concentration distributions, c_s , at the semiconductor-electrolyte interface at different ALCC values for 3 diffusion coefficients for front and back illumination. The histogram bars are binned with a logarithmic scale and the square above the bar indicates the intermediate concentration c_i corresponding to the ALCC. 56

Figure 3.10 (a) The tortuosity, τ , at different ALCC values for 3 diffusion coefficients for front and back illumination. The tortuosity corresponds to the mean path length of the reactants divided by the film thickness. The error bars indicate the standard deviations of the normal distributed tortuosity. (b) Diffusion paths of the reactants in a side view of a 3D rendered LTON photoanode..... 57

Figure 4.1 (a) SEM cross-section of Ag-IO reprinted with permission from reference [17]. (b) Illustration of the mass transport model for electrochemical reduction of CO_2 on Ag-IO. 67

Figure 4.2 Roughness factor as a function of the Ag-IO film thickness. The experimental data were taken from Yoon et al.[17]. The roughness factor of the model is a linear function. The model values are in general smaller than the experimentally determined values. Most probably, there is a micro roughness on the pore level that is not considered in the model. 70

Figure 4.3 Partial current density for the CO_2 and water reduction reaction, normalized by the electrochemical active surface area (ECSA). The experimental data from Yoon et al.[17] is shown with markers. The computed results are shown with a dashed ($m=n=1$) and a solid line ($m=n=1.2$). The lines and markers are color coded based on their roughness factor RF. 72

Figure 4.4 CO faradaic efficiency on Ag films, with differing RF, as a function of applied potential. The legend and color code is the same as in Figure 4.3. 72

Figure 4.5 A sensitivity study for the model with a RF=109. The partial current densities and the CO faradaic efficiency are shown for $\pm 10\%$ in pore and channel diameter. The water reduction is more sensitive to the changes in morphology than the CO_2 reduction. Reducing the pore diameter decreases the CO faradaic selectivity, whereas a reduction in the channel diameter enhances the selectivity. 74

List of Figures

- Figure 4.6 (a) Local current density profiles of CO and H₂ evolution along the \tilde{x} -axis of Ag-IO electrodes with RF=4, 43, 78, 109 and thickness $t=0$ (planar), 1.7, 3.1, 6.2 μm . (b) Concentration profiles along the \tilde{x} -axis of OH⁻, CO₃²⁻, HCO₃⁻ and CO₂ versus their bulk concentration. Both Figures are at a potential of -0.8 V vs. RHE..... 75
- Figure 4.7 (a) Illustration of the horizontal and vertical cut line through the space of a pore at $\tilde{x}=1 \mu\text{m}$ for an Ag-IO with RF=109 at -0.8 V vs. RHE. (b)-(e) Concentration profiles of CO₂, HCO₃⁻, CO₃²⁻ and OH⁻ along the cut lines, with the star indicating the end position. (f) Contour plot of the OH⁻ concentration on the x-y cut plane. 78
- Figure 4.8 (a) Partial CO current density for Ag-IO with pore diameters of 150-400 nm and film thickness of 3 and 15 μm . (b) CO faradaic efficiency for electrodes with the same pore diameters and film thickness of 3, 6 and 15 μm . (c) The values of the maximum CO faradaic efficiency in the contour plot as a function of the film thickness t and the roughness factor RF. Also, the linear relation between RF and t is shown for the different pore diameters. (d) The potentials vs. RHE for the maximum CO faradaic efficiency as a function of the film thickness t and the roughness factor RF. 79
- Figure 4.9 The tortuosity is defined as the diffusion path length through the entire Ag-IO film divided by the thickness t . Results for a film thickness of 3, 6, 10, and 15 μm are shown for films with pore diameters of 100, 200 and 400 nm..... 80
- Figure 4.10 (a) The gain factor in the maximum CO faradaic efficiency by adding a passive layer with the same mesoporous structure on top of the Ag-IO. The added layer has a thickness between 0.5 and 3 μm . The maximum CO faradaic efficiency of the bare electrode (without a passive layer) is shown on the top x -axis. (b) The CO and H₂ evolution current density distribution along the \tilde{x} -axis for a 3 μm thick Ag-IO at -0.7 V vs. RHE with no added layer (dashed line) and passive layers (colored lines)..... 81
- Figure 4.11 The gain factor in the maximum CO faradaic efficiency by an additional porous diffusion layer on top of the Ag-IO. p (<1) is the factor by which the diffusion coefficients are reduced in the porous media and t_{diff} is the thickness of the diffusion layer..... 83
- Figure 5.1 2D simulation domains for a photoanode with a wedge structure. Solar irradiation (AM1.5G) enters the water domain at an angle α_i , propagates through the absorbing water, semiconductor, and backing film, with reflections at the interfaces. Resonant light trapping in the thin semiconductor film, as well as geometric light trapping due to the wedge structure are expected. The Floquet periodicity is applied at the lateral boundaries, and the

input boundary is backed by a perfect matching layer to eliminate reflected waves crossing the input boundary..... 93

Figure 5.2 (a) Internal quantum efficiency for different film thicknesses as a function of the depth y in the film for empirical parameters: $\Phi=0.74$, $P_F=0.95$, $P_B=1$, and $L=20$ nm. (b) Integration points..... 97

Figure 5.3 Complex refractive indices. (a) water [28], (b) α -Fe₂O₃ [13], (c-d) Pt [29] and Pt on ultrathin SnO₂ [13], (e-f) Ag on ultrathin SiO₂ [30] and Ag on ultrathin SnO₂. 98

Figure 5.4 Solar spectrum at AM1.5G with $d\lambda=4$ nm..... 99

Figure 5.5 Photogenerated current densities for the α -Fe₂O₃ film on (a) an Ag or (b) a Pt reflective layer. Using the complex refractive indices from Dotan et al. [13], the model is validated. A complex refractive index for Pt without considering the ultrathin SnO₂ layer from Werner et al. [29] leads to much higher photogenerated current densities..... 100

Figure 5.6 Absorbed photon flux maps per unit time, unit area and unit film thickness for four different film thicknesses. The film thicknesses are normalized for visualization purposes. Electrodes stacks with α -Fe₂O₃ films on planar, (a) perfectly transparent, (b) perfectly reflective, (c) Ag, (d) Pt current collector. Symmetry unit cell of the wedge structure with an α -Fe₂O₃ film on (e) perfectly transparent, (f) perfectly reflective, (g) Ag, (h) Pt current collector. 102

Figure 5.7 Integrated absorbed photon flux profiles as a function of the film thickness. The indicated photogenerated current density assumes an IQE=1. (a) Comparing a wedge structure ($\gamma=54^\circ$, $R_w=0.8$) (blue) to planar electrodes (black) for perfect reflective (dashed), transparent (dotted), Ag (solid), and Pt (dash-dot) current collectors. (b) Gain factors with the planar, transparent current collector as a reference. Flux profiles for wedge structures with different angles, γ , and aspect ratios, R_w , with (c) perfect reflective, and transparent, and (d) Ag, and Pt current collectors. The planar, transparent reference case is also included in (d). All close-up windows are not in scale..... 104

Figure 5.8 Photocurrent densities for ideal forward-injection of minority carriers ($\Phi=1$, $P_F=1$). All photocurrent densities are normalized by the section width, d_{sc} . Planar and wedge structures on (a) transparent (dotted), perfect reflective (dashed), (b) Ag (solid), and Pt (dash-dot) current collectors. All close-up windows are not in scale..... 105

Figure 5.9 Gain of maximum photocurrent through geometric light trapping as a function of the wedge angle, γ , and aspect ratio, R_w . The gain is quantified for wedge structures with (a)

List of Figures

transparent, (b) perfect reflective, (c) Ag, and (d) Pt layer compared to their planar configuration counterparts.....	107
Figure 5.10 Surface roughness factor as a function of the wedge angle, γ , and aspect ratio, R_w . The surface roughness factor is defined as the surface area divided by the projected area (section width, $2d_{sc}$).....	108
Figure 5.11 (a) Photocurrent density for different incoming light angles, taking into account the reduction of the incoming power and the change of incident angle through the air-glass and glass-water interfaces. Parameters for the IQE probability model are ($\Phi=0.74$, $P_F=0.95$, $P_B=1$, and $L=20$ nm). The results for a planar and two wedge structures on an Ag current collector are compared to a 25nm thick α -Fe ₂ O ₃ film. (b) The relative improvement in the photocurrent compared to the planar configuration. (c) Photocurrent densities for different wedge dimensions.	110
Figure 5.12 <i>Master Template</i> : Direct laser lithography and dry etching are used to create a mask layout with a SiO ₂ layer on a silicon wafer. Subsequent wet etching in KOH converts the SiO ₂ mask layout into 3D wedge structures. <i>Process Flow A</i>] “Strip then Deposit”: Polyimide is applied, cured and stripped by peeling. The patterned polyimide is then used as a substrate to deposit a transparent or reflective, conductive layer, followed the deposition and annealing of the desired semiconductor. <i>Process Flow B</i>] “Deposit then Strip”: Depositing WTi and the sacrificial Al layer, followed by the electrode stack in reverse order, starting with the semiconductor film. This approach allows higher annealing temperatures. Subsequently, a transparent or reflective conductive layer is deposited, followed by a backing layer. The photoelectrode is stripped from the silicon template by anodic dissolution of the Al in 2 M NaCl solution. For both process flows, the silicon master template can be reused.	112
Figure 5.13 (a) Photolithography template layouts for inverse pyramids (left) and wedges (right). (b) Anisotropic silicon etching in KOH. The SiO ₂ mask is shown in black.	115
Figure 5.14 Multilayer stacks for (a) process flow A], and (b) process flow B].	118
Figure 5.15 <i>Process Flow A</i>]: Wedge structure transferred to a polyimide layer and coated with an ITO, SnO ₂ and a α -Fe ₂ O ₃ film. (a) SEM images and (b) photograph. Size of electrode = 1 x 2 cm ² . <i>Process Flow B</i>]: Multilayer (α -Fe ₂ O ₃ /SnO ₂ /TiN/Au/Ag/Ti/TiN/Ti/Polyimide) deposited onto a wedge structure and released by anodic dissolution of Al. (c) SEM images and (d) photograph. Size of electrode = 1 x 1 cm ²	120

Figure 5.16 Silicon master template sputtered with 100 nm WTi and 400 nm Al. 121

Figure 5.17 Photoelectrochemical characterization in 1M NaOH of fabricated electrodes under simulated AM1.5G irradiation. Planar (light blue) and microstructured (dark blue) electrodes fabricated according to process flow A] with a transparent current collector. Planar (yellow) and microstructured (red) electrodes fabricated according to process flow b] with a reflective current collector. α -Fe₂O₃ deposited on an FTO glass as a reference configuration. 122

Figure 5.18 Photographs of the silicon template wafer after the deposition of Fe₂O₃ by (a) USP and (b) ALD. SEM images of the stripped microstructure following the process flow B] for Fe₂O₃ deposited by (c) USP and (d) ALD. 124

Figure 5.19 Detailed view on a stripped array of micro-pyramids following the process flow B] for Fe₂O₃ deposited by ALD. 124

List of Tables

Table 4.1 Rate constants for reactions (4.1) and (4.2) at 25°C [20], [32].	67
Table 4.2 Species bulk concentrations in 0.1 M KHCO ₃ at 25°C [14].	67
Table 4.3 Diffusion coefficients of species in water at 25°C. The values have been corrected with the Stokes-Einstein equation [4].	67
Table 4.4 Empirical parameters fitted to the experimental data of a planar Ag electrode.	73

List of Symbols

A	Absorptance	[-]
A_p	Projected flat area	[m ²]
a	Morphological fitting parameter	[m ³ mol ⁻¹]
α	Absorption coefficient	[m ⁻¹]
α^*	Effective absorption coefficient	[m ⁻¹]
α_i	Incident angle	[°]
B	Width of flow cell	[m]
b	Morphological fitting parameter	[m ³ mol ⁻¹]
β	Charge transfer coefficient	[-]
c	Speed of light	[m s ⁻¹]
c_{bulk}	Bulk concentration	[M]
c_i	Intermediate concentration	[M]
c_s	Local surface concentration	[M]
D	Diffusion coefficient	[m ² s ⁻¹]
d	Diameter	[m]
d_s	Shortest diameter of the ellipsoid	[m]
d_h	Intermediate ellipsoid diameter	[m]
d_l	Longest ellipsoid diameter	[m]
d_{SC}	Section width	[m]
d_{film}	Film thickness	[m]
dr	Sphere overlap	[m]

List of Symbols

ε	Porosity	[-]
ε_0	Permittivity in vacuum	[F m ⁻¹]
η	Overpotential	[V]
E	Electric field intensity	[V m ⁻¹]
F	Probability density function	[-]
	Faraday constant	[C mol ⁻¹]
f	Size distribution function	[m ⁻¹]
G	Generation rate per volume	[m ⁻³ s ⁻¹]
γ	Aspect ratio flow cell	[-]
	Wedge angle	[°]
H	Product of the eigenvalue and eigenvector matrices	[-]
H	Magnetic field intensity	[A m ⁻¹]
h	Planck constant	[J s]
i	Current density	[A m ⁻²]
i_0	Exchange current density	[A m ⁻²]
i_{lim}	Limiting current density	[A m ⁻²]
i_w	Current density without mass transport limit	[A m ⁻²]
K	Equilibrium constant	[M ⁻¹]
k	Imaginary part of refractive index	[-]
k_y	Local mass transfer coefficient	[m s ⁻¹]
k_f	Forward rate constant	[M ⁻¹ s ⁻¹]
k_r	Reverse rate constant	[s ⁻¹]
L	Length flow cell	[m]
L_p	Length wedge	[m]
L_g	Length gap	[m]
λ	Wavelength	[m]
m	Reaction order	[-]
μ	Complex permeability	[H m ⁻¹]
N	Total species flux	[mol s ⁻¹]
n	Number of transferred charges	[-]
	Reaction order	[-]
	Real part of refractive index	[-]
n_{pores}	Number of pores	[-]
$\Phi_{>Eg}$	Integral of the incoming photon flux	[m ⁻² s ⁻¹]
p	Reduction factor	[-]

P	Incident power	[W nm ⁻¹]
q	Elementary charge	[C]
R	Gas constant	[J mol ⁻¹ K ⁻¹]
R_w	Aspect ratio	[-]
Re	Reynolds number	[-]
r_{pore}	Pore radius	[m]
ρ	Spectral reflectance	[-]
	Density	[kg m ⁻³]
S	Height of the flow cell	[m]
Sh	Schmidt number	[-]
σ	Electrical conductivity	[S m ⁻¹]
T	Temperature	[K]
t	Film thickness	[m]
t^*	Effective film thickness	[m]
τ	Transmittance	[-]
	Tortuosity	[-]
$V(z)$	Volume fraction	[-]
X	Vector test point	[-]
X_0	Vector centroid	[-]
x	Coordinate	[m]
ξ	Normalized photon flux	[-]
y	Coordinate	[m]
z	Coordinate	[m]

Acronyms

ALCC	Absorbed-light-to-charge-transfer-rate-conversion
ALD	Atomic layer deposition
AM1.5G	Air mass 1.5 global
BSE	Backscattered electron
ECSA	Electrochemical active surface area
FCC	Face centered cubic
FIB-SEM	Focused ion beam scanning electron microscope

List of Symbols

FTO	Fluorine doped tin oxide
ILCC	Light-to-charge-transfer-rate-conversion
IO	Inverse opals
IQE	Internal quantum efficiency
ITO	Indium tin oxide
KOH	Potassium hydroxide
LTON	Lanthanum titanium oxynitride
LTO	Lanthanum titanium oxide
mP	Micro-pores
nP	Nano-pores
PEC	Photoelectrochemical
PML	Perfect matching layer
PLD	Pulsed laser deposition
RF	Roughness factor
RHE	Reversible hydrogen electrode
RMS	Root mean square
RV	Representative volume
SAD	Selected-area diffraction
SE	Secondary electron
SEM	Scanning electron microscope
SSE	Sum of square errors
STEM	Scanning transmission electron microscopy
STH	Solar-to-hydrogen
TE	Transverse electric
TEM	Transmission electron microscopy
TM	Transverse magnetic
TX	Average of TE and TM
USP	Ultrasonic spray pyrolysis

Introduction

The current rate of greenhouse gas emissions and pollution of the environment caused by human activities pose a real and urgent threat to the health and future of the planet and humanity. We as a society have to drastically change paths and become more resourceful in all aspects of life in order to preserve our livelihood. At the same time, living standards of millions of people need to be raised, as one-in-eight of the world's population have no access to electricity [1], and the world's population is rising until the predicted plateau at around 11.2 billion people by the year 2100 [2]. Together with living standards, the demand for electricity, consumer goods and mobility are rising. According to the International Panel on Climate Change, 35% of the current greenhouse gas emissions are caused by the energy sector and 14% by the transport sector [3]. In order to halt the increasing greenhouse gas levels in the atmosphere and to limit temperature changes to about 2° C, drastic and immediate measures are needed. Governments and multinational corporations have the responsibility to accomplish a fast transition from fossil fuel powered energy generation facilities and combustion systems towards sustainable and renewable energy technologies. Newly installed energy infrastructure should take advantage of locally available renewable energy sources, and decentral power generation should provide energy security without long transmission paths. The global potential for sustainable power generation is immense. In a practical sense, there is an estimated reachable capacity of 1-2 TW from hydroelectric, 4 TW from wind and more than 20 TW from solar energy sources. To tap these mentioned potentials, wind turbines would have to be installed on 10-15% of the technically suitable on- and off-shore sites and 0.16% of the earth's surface would have to be covered with 10% efficient solar cells [4]. The task of installing such systems on a Terawatt scale is monumental and also comes with the challenge of dealing with the high variability of the generated power

Introduction

output, depending on factors like daytime and weather. Therefore, energy storage over a period of hours, days, or even throughout seasons, becomes essential. Storing electricity from renewable sources in energy-dense chemical bonds offers a path to generate power when sustainable energy sources are available and the ability to use them at a later time according to the demand.

The conversion of water into hydrogen is an attractive approach to store energy. The water-splitting reaction can be written as follows:



The reaction consists of a two-electron transfer reaction at the hydrogen evolving cathode and a four-electron transfer reaction at the oxygen producing anode. Water is an abundant and non-toxic source for a hydrogen energy storage system and is the only product after the conversion to electricity within a fuel cell. Another reaction considered for intermediate energy storage is the reduction of CO₂. As a feedstock, CO₂ is closing the loop of currently used hydrocarbon fuels, where the exhaust gas is regenerated into a chemical fuel. This approach would not reduce the CO₂ levels in the atmosphere, but would ideally stabilize it. The energy required to capture the CO₂ and to transfer six or eight electrons in the electrochemical half-reaction in order to produce methanol or methane, respectively, pose additional challenges. For both considered electrochemical paths to generate solar fuels, the energy to run the reaction can be provided in the form of electricity from a photovoltaic panel, another form of renewable energy source, or the electrodes themselves absorb light and photogenerate the charges for the reactions. The latter configuration is appealing due to its single component, all-in-one design that potentially could reduce the costs of the system [5]. However, the requirements for the electrode materials become much more stringent.

A semiconductor photoelectrode in an electrochemical water-splitting device needs to fulfill the following criteria: strong visible light absorption, efficient charge separation and transport, as well as a high stability in aqueous solution under reaction conditions [6]. Furthermore, the material should be abundant, non-toxic and cheap in order to make the system scalable. In the last decades, many semiconductors have been screened, but no material has been found to meet all of these aforementioned criteria [7]. However, if the bulk material exhibits some deficits in the required properties, modifications of the morphology could lead to improvements in the water-splitting efficiency. The most intuitive example is the trade-off between the light absorption length and the charge collection length. If a photoelectrode material needs a large thickness to absorb a substantial part of the solar spectrum, minority charges generated deep in the material might not be able to reach the semiconductor-electrolyte interface, as they are lost through recombination.

Micro- or nanostructuring is a common approach to decouple the length scale of light absorption from the charge carrier path. An illustrative example is Cu_2O that absorbs light in the first micrometers [8], but has an electron diffusion length of 20-200 nm [9]. Luo et al. [10] introduced a nanowire array of 3-5 μm long wires with a radius of approximately 150 nm. Compared to a planar electrode, the photocurrent density of the hydrogen generation reaction was improved by 25% to 10 mA/cm^2 . Thus, nanostructuring is an effective method to achieve photocurrents closer to the theoretical maximum (Cu_2O : 14.5 mA/cm^2).

Probably the most studied photoanode material in the photoelectrochemical water-splitting community is hematite ($\alpha\text{-Fe}_2\text{O}_3$), due to its stability in an aqueous environment and abundance [11]. However, it is also the minority charge collection length in the nanometer range that results in a neglectable photocurrent response for thick $\alpha\text{-Fe}_2\text{O}_3$ films [12]. Numerous studies have been conducted on the micro- and nano-structuring of the morphology with some improvements in efficiency. Photocurrents for mesoporous (1.1 mA/cm^2) [13], nanorods (1.24 mA/cm^2 , Sn-doped) [14], nanosheets (1.4 mA/cm^2 , Ge-doped) [15], nanotubes (1.41 mA/cm^2) [16], cauliflowers (2.1 mA/cm^2) [17], and nanocones (2.42 mA/cm^2 , Ti-doped) [18] at 1.23 vs. RHE (Reversible hydrogen electrode) were reported. However, even the performance of the best electrode is not even close the theoretical maximum of 12.6 mA/cm^2 . The reasons for the low photocurrents could be caused by recombination sites in the material and on the surface introduced during the deposition, but it could also be directly linked to the morphology. From the reported SEM images, it is difficult to assess the 3D structure and to quantify how many of the deposited nanostructures are connected to the current collector in the back. Furthermore, paths for minority charge carriers might be reduced by nano-structuring, but it is essential to know where the charges are photogenerated in the structure in order to draw further and quantitative conclusions. Also, due to the morphology, the local charge carrier fluxes at the semiconductor-electrolyte interface could be increased substantially, and they might cause high losses through recombination. The same uncertainty in identifying performance limits applies to another reported approach with a meso-structured host material covered by a thin $\alpha\text{-Fe}_2\text{O}_3$ film. Due to the thin semiconductor thickness, the photogenerated charges can reach the semiconductor-electrolyte interface, and the porosity of the guest material enables light absorption over several micrometers. Reported guest materials are porous TiO_2 template covered by niobium-doped tin oxide [19] or a WO_3 scaffold structure [20] with film thicknesses of 1-3 μm and pores in the order of hundreds of nanometers. The photocurrents of these electrodes were still below 2 mA/cm^2 , which poses the questions of how the morphology is linked to the electrode performance and what are the limiting factors. Besides the light absorption and the charge

transport, there is the transport of reactants and products in the electrolyte and pH gradients introduced by the electrode geometry that could limit the performance.

Understanding the effect of nano- and mesostructuring of electrodes has implications on various electrochemical energy storage applications [21]. Progress, in order to enhance the electrode performance by the structuring of the morphology, has been accomplished for batteries [22], dye-sensitized solar cells [23] and alkaline electrolyzers [24]. The developed methods in this thesis could also be applied to propose design-guidelines for those applications.

In this thesis, the link between the electrode morphology and multi-physical transport is investigated for photoelectrochemical water-splitting and electrochemical carbon dioxide reduction. Combined experimental-numerical methods are applied to characterize the influence of the morphology on the electrode performance. The feature sizes of the analyzed structured electrodes are in the range of nano- and micrometers and the focus for all the studies is on an accurate characterization and representation of the morphology. Due to the large range of the pore dimensions found in the investigated materials, the pore size characterization was not done according to the standard proposed by the International Union of Pure and Applied Chemistry (IUPAC). The IUPAC standard characterizes pores bigger than 50 nm already as macro-pores, whereas in this thesis, the pore characterizations were introduced in each chapter individually. Conclusions based on structural inspections and numerical transport simulations are translated into design guidelines for the fabrication of structured (photo-) electrodes.

In *Chapter 2*, a new quantitative approach for the 3D characterization of complex photoelectrodes is introduced. Focus ion beam and scanning electron microscope (FIB-SEM) tomography is for the first time applied to photoelectrodes of a water-splitting device. The method is demonstrated on two photoelectrodes, a particle-based lanthanum titanium oxynitride (LTON) and a ‘cauliflower-like’ structured hematite (α -Fe₂O₃) electrode, with feature sizes on multiple scales. The FIB-SEM tomography is destructive and ex-situ, capable of providing high resolution (voxel size down to 4 x 4 x 4 nm³) data over relatively large volumes (hundreds of cubic microns). The sample preparation, data acquisition and post-processing are discussed in detail. Algorithms are introduced to quantify and parameterize the morphology of the electrodes. Conclusions are drawn about the morphological parameters, the film structure and how the fabrication process can be improved.

The digitalized 3D geometry of the LTON electrode is then used in *Chapter 3* to run numerical multi-physics simulations. The discretization of the tomography data and the finite volume model are discussed. The light absorption is calculated by electromagnetic wave propagation simulations

using volume fraction profiles along the sample thickness. All the photogenerated charges are translated into photocurrent density maps along the semiconductor-electrolyte interface, which are used as a boundary condition for the subsequent ion diffusion calculations. The results reveal the operating conditions or material properties, for which the mass transport in the electrolyte is limiting. Furthermore, the ion concentration distributions and local pH values are quantified. This chapter demonstrates how vital the consideration of the morphology is regarding the reaction performance and introduces a robust methodology to run detailed simulations at the pore-level.

In *Chapter 4*, the developed numerical tools were adapted for electrochemical carbon dioxide reduction on an inverse-opal silver electrode, where concentration gradients play a more significant role. The catalytic selectivity towards the CO₂ reduction or the undesired water-splitting reaction is dependent on the local species concentrations in the electrolyte. Idealized inverse-opal geometries are parameterized and used for diffusion and electrochemical reaction simulations. The influence of the morphology on the selectivity towards CO evolution is quantified and discussed in detail. Based on the results, new concepts for mesoporous electrode architectures are introduced, and their benefits are further described.

In *Chapter 5*, a combined experimental-numerical platform is introduced where light absorption in thin film photoelectrodes is optimized. Simulations of the electromagnetic wave propagation on accurate microstructures are used to optimize the semiconductor film thickness and the electrode morphology for maximum light absorption. Local photocurrent densities at the semiconductor-electrolyte interface are calculated via a probabilistic charge collection model. A novel fabrication process based on template-stripping is developed in order to fabricate electrodes with precise control on the microstructure. This last chapter demonstrates how numerical calculations and innovative fabrication processes are fundamental to increase the photocurrents of structured water-splitting electrodes.

References

- [1] International Energy Agency, “World Energy Outlook Executive Summary,” 2018.
- [2] United Nations, “Volume I: World Population Prospects,” 2017.
- [3] C.B. *et al.*, “IPCC AR5 WGII Technical summary,” 2014.
- [4] R. van de Krol and M. Grätzel, *Photoelectrochemical hydrogen production*, vol. 102. New York: Springer, 2012.
- [5] T. J. Jacobsson, V. Fjällström, M. Edoff, and T. Edvinsson, “Sustainable solar hydrogen production: from photoelectrochemical cells to PV-electrolyzers and back again,” *Energy Environ. Sci.*, vol. 7, no. 7, p. 2056, 2014.
- [6] R. Van De Krol, Y. Liang, and J. Schoonman, “Solar hydrogen production with nanostructured metal oxides,” *J. Mater. Chem.*, vol. 18, no. 20, pp. 2311–2320, 2008.
- [7] J. Li and N. Wu, “Semiconductor-based photocatalysts and photoelectrochemical cells for solar fuel generation: a review,” *Catal. Sci. Technol.*, Sep. 2014.
- [8] C. Malerba, F. Biccari, C. Leonor Azanza Ricardo, M. D’Incau, P. Scardi, and A. Mittiga, “Absorption coefficient of bulk and thin film Cu₂O,” *Sol. Energy Mater. Sol. Cells*, vol. 95, no. 10, pp. 2848–2854, 2011.
- [9] A. Paracchino, J. C. Brauer, J. E. Moser, E. Thimsen, and M. Graetzel, “Synthesis and characterization of high-photoactivity electrodeposited Cu₂O solar absorber by photoelectrochemistry and ultrafast spectroscopy,” *J. Phys. Chem. C*, vol. 116, no. 13, pp. 7341–7350, 2012.
- [10] J. Luo, L. Steier, M. K. Son, M. Schreier, M. T. Mayer, and M. Grätzel, “Cu₂O Nanowire Photocathodes for Efficient and Durable Solar Water Splitting,” *Nano Lett.*, vol. 16, no. 3, pp. 1848–1857, 2016.
- [11] K. Sivula, F. Le Formal, and M. Grätzel, “Solar water splitting: progress using hematite (α -Fe₂O₃) photoelectrodes,” *ChemSusChem*, vol. 4, no. 4, pp. 432–49, Apr. 2011.
- [12] J. C. Chou, S. A. Lin, C. Y. Lee, and J. Y. Gan, “Effect of bulk doping and surface-trapped states on water splitting with hematite photoanodes,” *J. Mater. Chem. A*, vol. 1, no. 19, pp. 5908–5914, 2013.
- [13] R. H. Gonçalves, B. H. R. Lima, and E. R. Leite, “Magnetite colloidal nanocrystals: A facile pathway to prepare mesoporous hematite thin films for photoelectrochemical water splitting,” *J. Am. Chem. Soc.*, vol. 133, no. 15, pp. 6012–6019, 2011.
- [14] Y. Ling, G. Wang, D. A. Wheeler, J. Z. Zhang, and Y. Li, “Sn-doped hematite nanostructures for photoelectrochemical water splitting,” *Nano Lett.*, vol. 11, no. 5, pp.

- 2119–2125, 2011.
- [15] J. Liu *et al.*, “Highly oriented Ge-doped hematite nanosheet arrays for photoelectrochemical water oxidation,” *Nano Energy*, vol. 9, pp. 282–290, 2014.
- [16] S. K. Mohapatra, S. E. John, S. Banerjee, and M. Misra, “Water photooxidation by smooth and ultrathin R-Fe₂O₃ nanotube arrays,” *Chem. Mater.*, vol. 21, no. 14, pp. 3048–3055, 2009.
- [17] S. C. Warren *et al.*, “Identifying champion nanostructures for solar water-splitting,” *Nat. Mater.*, vol. 12, no. 9, pp. 842–9, 2013.
- [18] Y. Qiu *et al.*, “Efficient photoelectrochemical water splitting with ultrathin films of hematite on three-dimensional nanophotonic structures,” *Nano Lett.*, vol. 14, no. 4, pp. 2123–9, Apr. 2014.
- [19] M. Stefik, M. Cornuz, N. Mathews, T. Hisatomi, S. Mhaisalkar, and M. Grätzel, “Transparent, conducting Nb:SnO₂ for host-guest photoelectrochemistry,” *Nano Lett.*, vol. 12, no. 10, pp. 5431–5435, 2012.
- [20] A. Müller, I. Kondofersky, A. Folger, D. Fattakhova-Rohlfing, T. Bein, and C. Scheu, “Dual absorber Fe₂O₃/WO₃ host-guest architectures for improved charge generation and transfer in photoelectrochemical applications,” *Mater. Res. Express*, vol. 4, no. 1, 2017.
- [21] S. Buller and J. Strunk, “Nanostructure in energy conversion,” *J. Energy Chem.*, vol. 25, no. 2, pp. 171–190, 2016.
- [22] R. Zhang, N. Li, X. Cheng, Y. Yin, Q. Zhang, and Y. Guo, “Advanced Micro/Nanostructures for Lithium Metal Anodes,” *Adv. Sci.*, vol. 4, no. 3, p. 1600445, 2017.
- [23] X. Liu, J. Fang, Y. Liu, and T. Lin, “Progress in nanostructured photoanodes for dye-sensitized solar cells,” *Front. Mater. Sci.*, vol. 10, no. 3, pp. 225–237, 2016.
- [24] F. Ganci *et al.*, “Performance Enhancement of Alkaline Water Electrolyzer Using Nanostructured Electrodes Synthesized by Template Electrosynthesis,” *2018 IEEE 4th Int. Forum Res. Technol. Soc. Ind.*, pp. 1–4, 2018.

Quantitative Structural Analysis of Morphologically Complex Electrodes 2

The content of this chapter is adapted with permission from The Royal Society of Chemistry from an article by Silvan Suter, Marco Cantoni, Yannick Gaudy, Simone Pokrant and Sophia Haussener published 2018 in Sustainable Energy and Fuels [1].

2.1 Introduction

Mesoporous morphologies are common for semiconductor films in photoelectrochemical water splitting [2]. There are mainly two reasons for such morphologies: *i)* The mesoporous structure is desired and fabricated by intentional nano or micro-structuring of the semiconductor in order to circumvent some of the critical limitations of bulk material properties; or *ii)* the morphology is a nonintentional result of less controllable, and cheap and fast processing routes, such as dip or slurry coating of conducting substrates with photocatalytic particles [3]. In both cases, the morphologies are often irregular, anisotropic and complex [4], and it is difficult to quantify the contributions of the morphology and predict an optimum structure. However, the morphology of semiconductor photoelectrodes has been shown to affect the performance of photoelectrochemical water splitting devices significantly [5].

Examples of deposition methods that lead to complex morphologies are chemical vapor deposition or particle colloidal deposition methods. Atmospheric chemical vapor deposition with iron pentacarbonyl $\text{Fe}(\text{CO})_5$ as a precursor was reported to lead to a tree-like hematite array, consisting of ‘cauliflower’ shaped nanopillars with a complex surface area [6]. One performance

limiting factor was experimentally determined to be the crystallinity of the ‘cauliflowers’ [7]. However, so far the morphology has not been quantified, and an understanding of its influence on performance is limited. An example of mesoporous photoelectrodes is a multi-layered particle network fabricated via electrophoretic deposition of lanthanum titanium oxynitride single crystalline particles on FTO glass [8]. The porosity of the particles, their stacking, and especially their connectivity with the TiO_2 necking are all morphological characteristics that greatly influence the performance of this photoelectrode, but have not been quantified and studied in a fully assembled configuration.

Here we propose a combined experimental-numerical approach for complex 3D photoelectrode morphologies to characterize the exact structure and quantify the morphological features. In previous studies, [9], [10], we used a similar approach to digitalize a complex morphology in the micrometer range, using absorption-based X-ray tomography, to successfully characterize the morphology and to calculate transport properties on the exact structure. In the present case, we deal with feature sizes in the range of nanometers. Therefore, imaging methods with higher resolution were required. Non-destructive, in-situ imaging methods are currently limited to 20 nm resolution as demonstrated by the Argonne National Laboratory’s Advanced Photon Source [11]. To increase the resolution, we chose to acquire the exact 3D geometry of morphologically complex photoelectrode films destructively and ex-situ using FIB-SEM tomography. FIB-SEM tomography has so far been used in a variety of research fields to characterize and quantify material morphologies, including LiCoO_2 cathodes in Li-Ion batteries [12], pore-networks in clay materials [13], and mouse tissue in life science studies [14]. This tomography method provides high resolution (voxel size down to $4 \times 4 \times 4 \text{ nm}^3$) with the ability to measure relatively large volumes of interest (hundreds of cubic microns). Precise ion beam milling and advanced automated tracking systems allow the measurement of relatively thick samples using isotropic voxels, providing the same high resolution in the slicing direction as in the imaging plane. This allows the analysis of samples with feature sizes on multiple scales, and permits the resolution of pores or struts in the nanometer range, while also measuring volumes large enough to statistically represent feature sizes, such as particles in the micrometer scale. FIB-SEM tomography can acquire data in order to quantify the overall film structure of the photoelectrode, as well as the individual components of the film. In the present study, the methodology is demonstrated on hematite ‘cauliflower’ and colloidal lanthanum titanium oxynitride photoelectrodes. The outcome of this study gives insights into the mesoporous structure of photoanodes. The visualization and quantification of the morphology reveals valuable information to optimize the fabrication process to further enhance the performance of the photoelectrodes.

2.2 Digitalization of the Morphology

Exact 3D morphology is acquired by FIB-SEM tomography. A cubic sample volume of the photoelectrode, embedded in epoxy, is eroded layer by layer using an ion beam. Between each milling step, a scanning electron beam acquires an image of the sample cross-section. This procedure is repeated until the ion beam has milled away the entire volume of interest. This destructive FIB-SEM tomography results in a sequence of cross-section images that allow the digital reconstruction of the sample morphology. In the following sections, the workflow of the FIB-SEM tomography, consisting of the sample preparation, ion beam milling, image acquisition, and digital reconstruction are described.

2.2.1 Materials and Sample Preparation

Two structured photoelectrodes of different materials, deposition procedures, and characteristic feature sizes were analyzed. Their SEM images are shown in Figure 2.1. *Sample (i)* was a 650 nm thick hematite ($\alpha\text{-Fe}_2\text{O}_3$) photoelectrode consisting of ‘cauliflower’ shaped pillars deposited on FTO by atmospheric pressure chemical vapor deposition (APCVD). The detailed fabrication process of this electrode and its photoelectrochemical behavior were published by Kay et al. [6]. These authors demonstrated a maximum photocurrent of 2.2 mA/cm^2 at $1.23 \text{ V}_{\text{RHE}}$ in AM 1.5 G light of 1000 W/m^2 . The smallest feature size, a single branch of a pillar, is in the range of tens of nanometers. *Sample (ii)* was a 7570 nm thick lanthanum titanium oxynitride (LaTiO_2N , LTON) photoelectrode that was fabricated by electrophoretic deposition of LTON particles on FTO, followed by a dip coating step resulting in particle necking with TiO_2 . The detailed fabrication of LTO particles by solid-state synthesis, the thermal ammonolysis step to obtain LTON particles, the deposition method, and the photoelectrochemical response were published by Landsmann et al. [8]. They reported a maximum photocurrent of $0.8 \mu\text{A/cm}^2$ at $1.23 \text{ V}_{\text{RHE}}$ for bare LTON and improved it to 2.2 mA/cm^2 at $1.23 \text{ V}_{\text{RHE}}$ by adding a co-catalyst [15], both measured in AM 1.5 G light of 1000 W/m^2 . The LTON particle dimensions vary from hundreds of nanometers to micrometers, and the pores within the particles are in the range of a few nanometers.

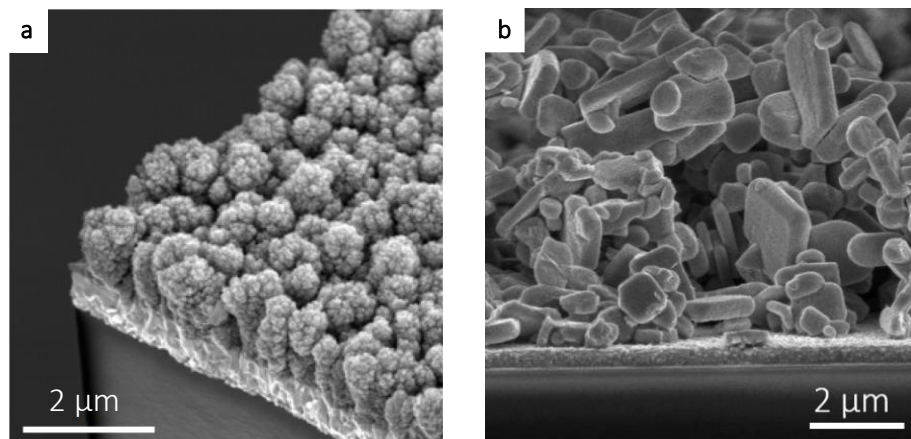


Figure 2.1 SEM images of the two analyzed photoelectrodes. (a) Hematite ($\alpha\text{-Fe}_2\text{O}_3$) was deposited on an FTO glass by atmospheric pressure chemical vapor deposition. The image was reprinted with permission from reference [7]. (b) The LaTiO_2N particles were stacked on an FTO glass by electrophoretic deposition, followed by dip coating to establish TiO_2 necking bonds between the particles.

For FIB-SEM tomography, the FTO glass with the deposited films were embedded in epoxy to increase the contrast of the SEM image. The effect of the epoxy is to provide mechanical support for free-standing structures, obscure the off-section features, in addition to increase contrast of the SEM image. The epoxy embedding medium was diluted with acetone at a ratio of 1:3 and the electrode was dip coated and put in a vacuum for 20 min. This step was repeated twice at an epoxy/acetone ratio of 2:2 and 3:1. The sample was then dip coated in pure resin, put in a vacuum for 20 min, and then polymerized for 24 h at 60° C. Subsequently, a wedge was polished with a tripod polishing tool using diamond lapping film discs of 6 μm, 3 μm, 1 μm, 0.5 μm roughness. The polishing was necessary to decrease the epoxy thickness to a few hundred nanometers above the volume of interest. The ion beam milling would have taken too long with a thick epoxy layer. A thin film of gold was sputtered onto the epoxy to diminish the charging effect during electron beam imaging. A fiducial platinum film was deposited in the FIB-SEM over the region of interest. Three V-shaped alignment reference grooves were milled into this film, perpendicular to the cross-sections. A 1 μm thick carbon layer was deposited on the top to increased the contrast of the alignment marks. The alignment marks and the deposited materials are shown in the close-up of Figure 2.2.

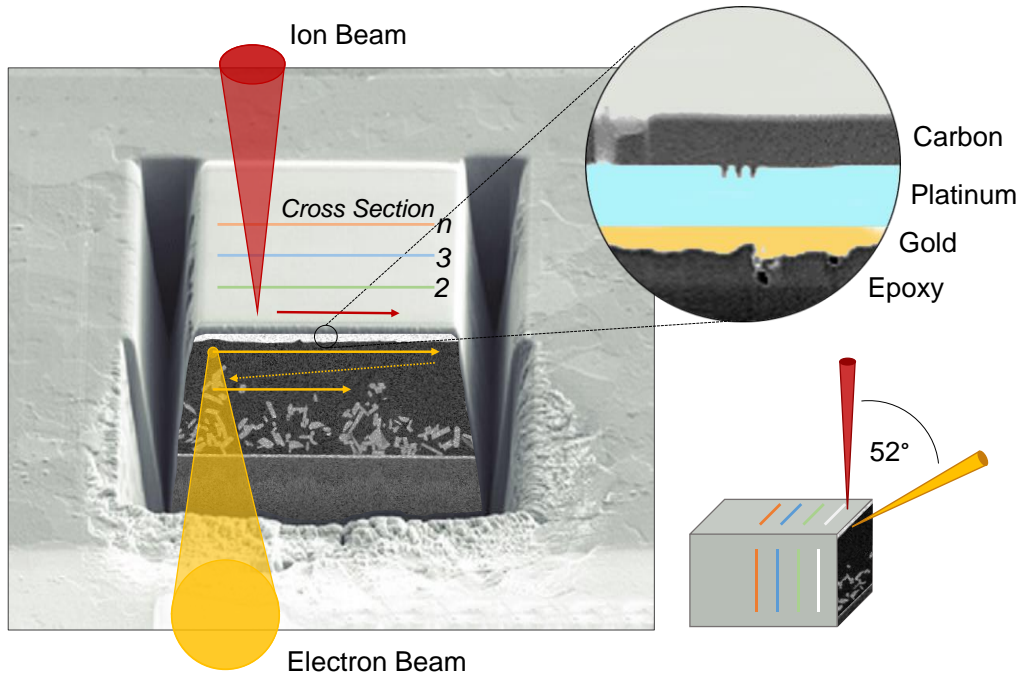


Figure 2.2 Scheme of the FIB-SEM tomography. The sample is embedded in epoxy as a structural support medium and to define a clear contrast between the semiconductor and the void phase. The close-up circle shows the V-shaped alignment grooves in the Pt layer, which run perpendicular to the cross-sections. The sample is covered by gold to reduce charging effects for the electron beam. The ion beam and electron beam column are at an angle of 52°. The ion beam mills perpendicular to the sample surface to expose cross-section by cross-section. The electron beam scans the cross-sections continuously, acquiring one image per cross-section.

2.2.2 FIB-SEM Nanotomography

We used a Zeiss NVision 40 Crossbeam system for the FIB-SEM tomography. The sample was mounted on the sample holder and tilted by 52° to align the ion beam column perpendicular to the sample surface. The ion beam was used to erode a trench in front of the volume of interest, allowing for accessibility and the acquisition of a first cross-section image by the scanning electron beam. The trench also prevents the redeposition of material on the cross-section area. A scheme of the FIB-SEM experimental setup is shown in Figure 2.2. Automated drift-correction and beam tuning (focus and stigmator) are needed in order to acquire stable sectioning of the sample for hundreds of images and to maintain spacing between the images in accord with SEM resolution (4 nm). The Atlas3D system (Fibics, Inc.), a scan generator and image acquisition system of Zeiss

devices, can cope with various drift phenomena (electron beam and ion beam), as well as a shift in imaging conditions, by assessing the position of the reference marks in the platinum layer. FIB milling and SEM imaging were done simultaneously to reduce overhead time. The ion beam continued to mill while the electron beam returned to start the scan of a new line (“fly-back”), and blanked when the electron beam acquired a line of the image in order to eliminate interference in the secondary electron images [16]. FIB milling was done at an acceleration voltage of 30 kV and a 300 pA beam current, and the SEM images were recorded with an acceleration voltage of 1.7 kV and 1 nA. We ran the FIB-SEM tomography for 24 h to obtain at least 1000 consecutive images of stable cross-sections. Secondary electron (SE) and backscattered electron (BSE) signals were recorded simultaneously.

2.2.3 Digital Reconstruction

The data for the hematite electrode was acquired with an isotropic voxel size of $4 \times 4 \times 4 \text{ nm}^3$ and consisted of 1354 images with the dimension of 6204×1000 pixels. The LTON electrode was measured with an isotropic voxel size of $8 \times 8 \times 8 \text{ nm}^3$. 1000 images with the dimension of 4065×1400 pixels were acquired. For the image post-processing, only the images from the SE signal were considered, and the algorithms were implemented in the open-source tool Fiji [17].

Image Registration

Despite the 3D tracking during the data acquisition, translational drift occurred. This remaining drift was corrected by a registration process of alignment marks, utilizing the three grooves milled into the platinum layer along the sectioning direction. The mark on the first cross-section image was used as a template and matched by a normalized correlation coefficient matching method to the following marks. Thus, the image translations were determined, and cross-sections were aligned using the plug-in Template Matching [18]. In the case of the relatively thick LTON sample, the cross-sections were inconsistently compressed in the height of the image due to charging effects that can deflect the electron beam. This compression was compensated for by first aligning the bottom of the FTO glass throughout the cross-section image stack. The alignment marks on top of the images were then taken to either expand or compress the individual images accordingly. Typical compression factors were in the range of 4 to 10 voxels.

Removal of Air Bubbles in Epoxy

A major challenge was the removal of air bubble artifacts in the cross-section images. The air bubbles formed in the epoxy during the sample preparation. In Figure 2.3a, the bubbles can be seen on the surface of the LTON particles, or in narrow gaps between the particles. For the image stack of cross-sections, a low pass filter was applied in the frequency domain, derived by a discrete Fourier transformation, to blur the pores in the particles. Features bigger than 3000 pixels were not affected by the filter. A histogram-based threshold segmentation (threshold = 88) and an erosion step, with a structuring disk of 5 pixels in diameter, was applied to the filtered images. By the erosion step, the artifacts were disconnected from the solid phase. Subsequently, only the larger connected solid volumes were identified by the algorithm, and a binary mask was obtained. Finally, the air bubble artifacts were removed from the original SEM images by merging the binary mask with the original images. Figure 2.3b shows the cross-section image after the post-processing.

Segmentation

We used a grey value histogram-based segmentation in order to differentiate between the solid and void domains and eventually digitalize the reconstructed dataset of grey values. A coarse segmentation of the structure for the two introduced photoelectrodes is straightforward. The epoxy filling of the void domain has a high carbon level with a large electron beam interaction volume, leading to a low signal to noise ratio, hence appearing black. However, the fine tuning of the segmentation was highly dependent on the quality and contrast of the acquired SEM images and needed to be adjusted for each measured dataset individually. For *sample (i)*, the smallest hematite features have a diameter of a few nanometers and suffer from edge effects. Edge effects appear when the scanning electron beam hits a small feature. Secondary electrons leave the feature through all surrounding edges, resulting in increased brightness, but a less sharp solid-void interface. We used an 8-bit threshold of 125 for the segmentation. This threshold laid symmetrically between the two extreme thresholds of 100, where all grey values except the background were included, and 150, where small features started to disconnect from the main solid phase. For *sample (ii)*, the outer interfaces between the LTON particles and void were well defined and sharp. However, the inner pores were not sufficiently filled with epoxy and showed weak contrast. The necking phase between the particles could be visually distinguished from the LTON by the texture and contrast in the electron beam image and was segmented by a machine-learning algorithm trained on manually selected image features using the *Trainable WEKA Segmentation* plug-in [19]. Before applying the plug-in, the contrast was improved by contrast limited adaptive histogram equalization [20] using the *Enhance Local Contrast (CLAHE)* plug-in in

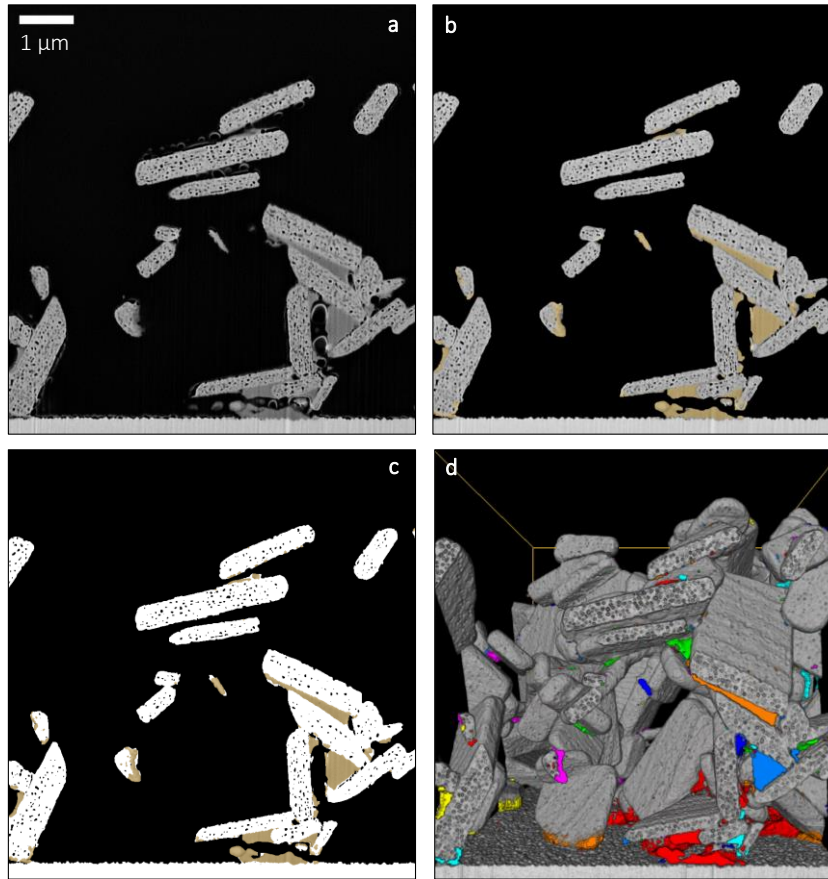


Figure 2.3 (a) Close-up of a cross-section image after the registration process. Air bubbles in the epoxy formed on the LTON surface or in the small channels between the particles. (b) The same cross-section image after eliminating the air bubbles. Also, the TiO_2 necking phase was identified and colored in yellow. (c) The final stage after the segmentation process. The three phases are separated in white = LTON, yellow = TiO_2 and black = void. (d) Identification and 3D rendering of all separated TiO_2 necking bonds in a subsection of the measured domain. Connected TiO_2 phases were given the same color.

Fiji. The size of the local region around a pixel for which the histogram was equalized was set to 127 pixels (block size). 256 bins were used to equalize the histogram and the max slope, which limits the contrast stretch, was set to 3 (1=no stretch, big number=no limit). For the machine learning, a classifier was obtained based on a small training data set and then applied to all the images. The quality of the segmentation could only be assessed visually and is shown in Figure 2.3c. The segmentation into the three phases (LTON particles, TiO_2 bonds, void phase) was

satisfactory. Figure 2.3d shows the 3D rendering of the TiO_2 necking where the individual TiO_2 phases were labeled, and connected TiO_2 phases were given the same color. For the first time, we identified and visualized the TiO_2 necking in an exact 3D representation of the LTON particle network. This data allows to assess and quantify the ability of the TiO_2 necking to connect the LTON particles over a length scale of multiple particles. Once the TiO_2 phase was subtracted, the LTON was segmented with an 8-bit threshold value of 92. An upper threshold of 106, where all the nano-pores were connected, and a lower threshold of 78, where only volumes entirely filled by epoxy were considered to be pores, were used to define error bars on the results, i.e., the sensitivity of the obtained results on the threshold accuracy.

3D Rendering

The 3D rendering of the acquired and post-processed data sets are shown in Figure 2.4. The 3D arrays of grey values are subsequently used to characterize and quantify the morphology. The digital representations of the morphologies can also be used as input data for mesh generators to construct grids for finite volume calculations.

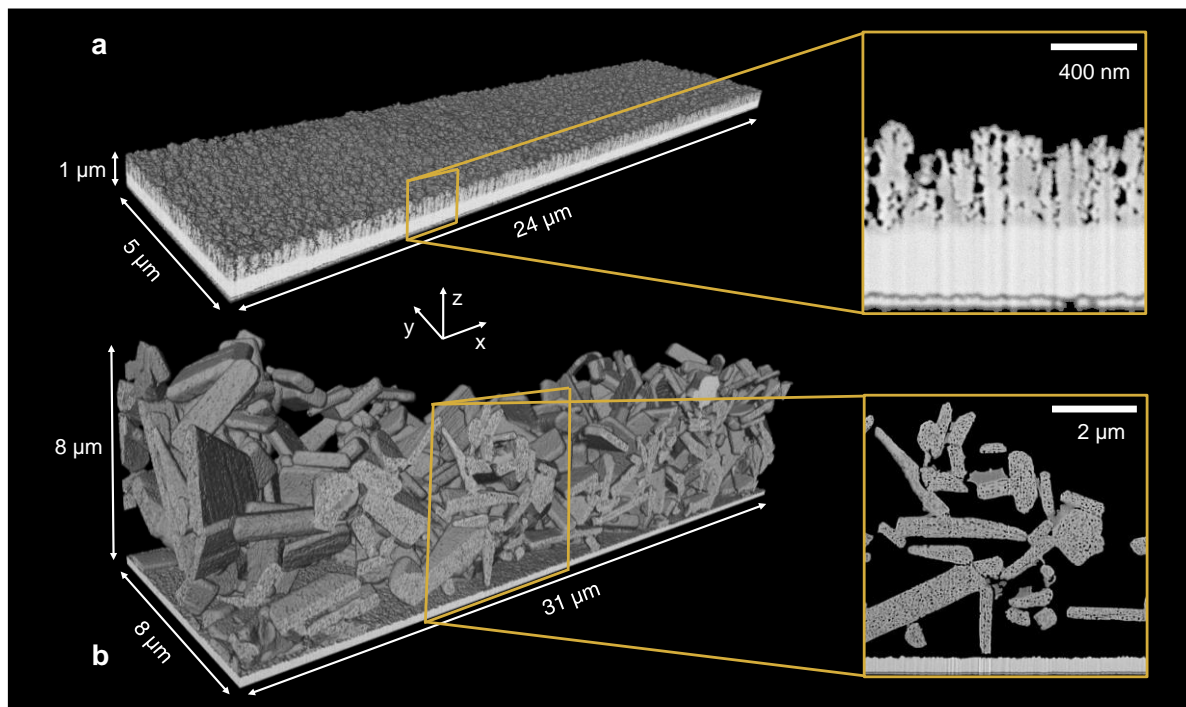


Figure 2.4 3D renderings of the analyzed photoelectrode morphologies with close-up views on the first cross-sections of the acquired volumes. (a) The α - Fe_2O_3 photoanode was measured with an isotropic voxel edge size of 4 nm. (b) The resolution of the LTON photoanode was an isotropic voxel edge size of 8 nm.

2.3 Methodology for the Morphological Characterization

2.3.1 Volume Fraction Profile

The volume fractions of the solid phases were calculated along the z-axis to determine a volume fraction profile throughout the thickness of the photoelectrode films. The volume fractions were computed using a voxel-based approach, and the volume of each pixel was assigned to a phase based on the segmentation process. The phase volume fraction of each pixel layer parallel to the substrate plane was determined by the ratio of phase pixels to the total number of pixels in that layer. The volume fraction profile was drawn perpendicular to the FTO glass surface, which was set as the origin ($x=0$).

2.3.2 Surface Area

The surface area was calculated by creating a triangular surface mesh and integrating over all triangle areas. The surface mesh was generated using the marching cube algorithm [21]. Eight neighboring voxels form the corners of a cube. The grey values of the voxels are linearly interpolated along the cube edges. The segmentation threshold value determines the interface point along the cube edges and defines the surface polygon that divides the cube into the solid and void phases. The algorithm marches through the dataset and sums up all the triangle areas. Surface triangles that touch the boundaries of the scanned volume were neglected, assuming symmetric boundary conditions.

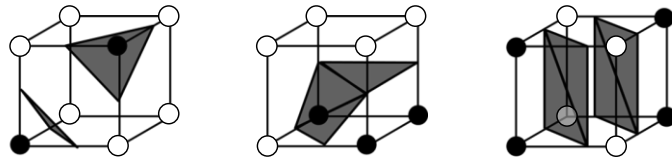


Figure 2.5 Scheme of triangular mesh generation using the marching cube algorithm. Three examples are shown for grey values 0 (black) and 255 (white). The algorithm was applied to data sets with continuous grey values between 0 and 255.

2.3.3 Size Distributions

The feature size at any point in the solid phase of the photoelectrode geometry was characterized by the biggest sphere that fits into the structure [22]. For this, mathematical morphology

operations were applied. After a threshold segmentation, the binary data set was sequentially processed by an opening algorithm with a structuring element increasing in size. The opening algorithm consists of a 3D morphological erosion, followed by a 3D morphological dilation, using a sphere with a diameter d [23], and thus, cancels all features smaller than the structuring element. The cumulative opening size distribution $1-F(d)=\varepsilon(d)/\varepsilon_0$ can be estimated by calculating the porosity, ε , after each step and relating it to the initial porosity, ε_0 . Its derivation leads to the size distribution, $f(d)=F'(d)$. The mean diameter is given as:

$$d_{\text{mean}} = \frac{\int_{d_{\text{min}}}^{d_{\text{max}}} d \cdot f(d) dd}{\int_{d_{\text{min}}}^{d_{\text{max}}} f(d) dd}, \quad (2.1)$$

where d_{min} and d_{max} are the considered lower and upper limits of the integration. The same methodology can be applied to the void phase, or to the TiO₂ necking phase, by inverting the segmented data set.

2.3.4 Particle Properties

An algorithm to fit ellipsoids into individual particles of an interconnected particle network was developed. The algorithm is only relevant for *sample (ii)* and was based on the principle of finding the maximal inscribing ellipsoid into a binary dataset for a given seed point. We used the matrix definition of an ellipsoid,

$$(X - X_0)^T H (X - X_0) \leq 1, \quad (2.2)$$

for its translational and rotational movement, and for evaluating if a point lies in the ellipsoid or on its border. H is the product of the eigenvalue and eigenvector matrices, X is the test point, and X_0 is the centroid [24]. Our method works on a stack of binary images and needs the coordinates of the seed points as input. For each seed point, the code fits the biggest possible ellipsoid into the solid phase. The calculations run on multiple cores in parallel for overlapping ellipsoids, or series for non-overlapping ellipsoids. Each ellipsoid is initialized with a small sphere (radius=4 voxels), and the radius is successively increased. A set number of points (default=1000)

on the surface of the sphere are evaluated after each step to determine whether they are located in the solid phase or the void phase. As soon as the sphere touches the void phase, an average vector between the contact points and the centroid is formed, and the sphere is moved away from the interface along the direction of the vector. The procedure is repeated until the sphere hits the solid-void interface on two opposite sides and thus is centered along the shortest axis of a particle. The radii are reduced back to 4 voxels, and the two semi-axes perpendicular to the shortest particle axis are simultaneously increased. Whenever the resulting ellipsoid hits the solid-void interface, the centroid gets pushed away, normal to the contact points. The medium axis of the particle is found once the ellipsoid has two contact points on opposite sides. The two in-plane semi-axes are rotated until one of the semi-axes merge with the medium particle axis. The radii are once more reduced to 4 voxels, and the last semi-axis is increased, and the centroid is moved away from the contact points until the final centroid location is found. In the last step, the ellipsoid semi-axes are inflated until the biggest possible ellipsoid volume is reached. The output of the code consists of an image stack with the computed ellipsoids, the values of the centroid coordinates, the volumes of the ellipsoids, the lengths of the semi-axes, and the eigenvectors of the ellipsoids, which describe the orientations of the semi-axes. The developed algorithm was inspired by the ellipsoid factor plug-in [24] in BoneJ [25] for estimating local bone thickness in trabecular bone structures. The code was written in Java as a Fiji plug-in.

2.3.5 Nano-Pore Characterization

For *sample (ii)*, the nano-pores within single LTON particles were characterized. The inner porosity, defined as the volume fraction of the pores within the particles, was computed using a voxel-based approach. Only the voxels that were located within the previously calculated ellipsoid volumes were extracted and segmented with a threshold value of 92. The inner porosity was calculated for each ellipsoid and then averaged. The connectivity of the nano-pore space was assessed by a 3D flood fill algorithm [26] starting from the inter-particle void space and subsequently flooding all the connected void phase voxels. The orientations of the pores relative to the orientation of the hosting ellipsoid were characterized. The pores within a given ellipsoid were separated by water shedding in order to break the pore network down into single volumes. The main elongations of these pores were computed by the tensors of inertia in Avizo, giving the orientations of the longest semi-axis of an ellipsoid fitted into each pore volume.

2.4 Results and Discussion

In this section, we first discuss the morphological quantification of the two examples of structured photoelectrode films based on the exact geometry obtained by FIB-SEM tomography. Subsequently, a multi-scale analysis of the features occurring in the LTON film is presented.

2.4.1 Mesoscopic Structural Characterization

Volume Fraction Profile

The volume fraction profile, assessing the material distribution through the thickness of the electrode films, is shown in Figure 2.6. The z -position in the film was normalized by the film thickness, t , to compare the LTON electrode (10 times thicker) to the hematite electrode. The film thickness of the hematite sample was $t=652$ nm. The LTON sample was 7.568 μm thick.

The volume fraction profile in the hematite film was divided into three regimes. First, there was an initial drop due to the ‘cauliflower’ stems developing from the bulk ($z/t=0-0.2$). Then, a second rather slow density decrease occurred from 85%-73% between $z/t=0.2$ and 0.5, where branches formed, followed by a sharp drop ($z/t > 0.5$) due to the uniform heights of the ‘cauliflowers’. The LTON film showed a much more loosely packed particle network of 30% solid, with a monotone decrease at the top ($z/t > 0.4$), as the particle density thinned out. This slow decrease in volume fraction was a result from the inhomogeneity of the film thickness.

In Figure 2.6, the solid volume fraction of the LTON particles, including the TiO_2 necking, is shown. The origin of the z -axis was set at the position where the solid volume fraction of the electrode deviated from 100%. However, as the FTO glass had a rough surface (profile height in the range of 20-120 nm), there was not an instant drop in the volume fraction. The low volume fraction just above the FTO glass ($z/t=0.015$) is explained by the fact that the plate-like particles are in contact with the glass with only a single corner. The volume fraction of the TiO_2 phase shows that the necking fills the roughness of the FTO surface and has the highest density (20%) just above the FTO substrate. Thus, the first layer of LTON particles was well-connected to the FTO substrate. TiO_2 density sharply dropped at a thickness larger than 400 nm and only connected the LTON particles over short distances. A calculated 6% of the total solid volume in the electrode was contributed by the necking.

The color shades around the hematite and LTON curves indicate the error bars assessed by an aggressive ($\alpha\text{-Fe}_2\text{O}_3$: 150, LTON: 106) and conservative ($\alpha\text{-Fe}_2\text{O}_3$: 100, LTON: 78) threshold-

based segmentation. The hematite electrode with a maximum error bar of (+ 6%, - 8%) was more affected by segmentation uncertainty due to small ‘cauliflower’ branches with diameters below 30 nm, showing a strong edge effect (bright and blurry secondary electron signal from small features) in the SEM image. The outlines of the LTON particles were sharp, i.e., steep grey value gradients, that minimized the sensitivity to the segmentation process. However, the uncertainty in the pore segmentation led to a maximum error bar of (+ 3%, -5%). The calculated mean volume fractions in the films were 60.1% and 19.8% for the semiconductor phase in the hematite and LTON sample, respectively.

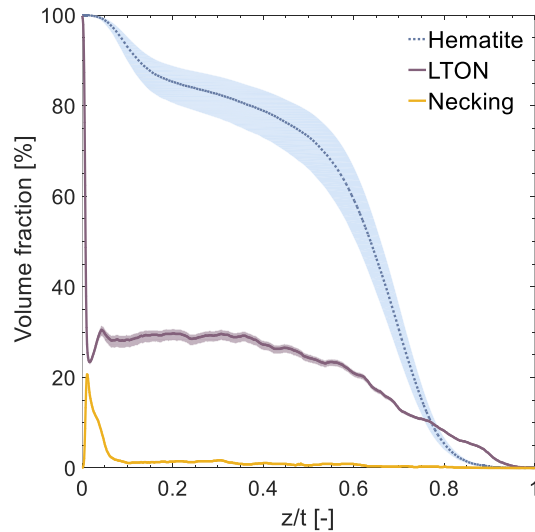


Figure 2.6 Volume fraction profiles through the normalized thickness of the photoelectrode films. The morphology of the $\alpha\text{-Fe}_2\text{O}_3$ electrode was much denser than the LTON film. The purple curves show the LTON volume fraction without TiO_2 necking. The yellow curve shows the volume fraction of only the necking phase (TiO_2). The FTO substrate was located at $z=0$. The film thickness of the hematite sample was $t=652$ nm. The LTON sample was 7.568 μm thick.

Surface Area

The surface area is an important performance-related property in photoelectrodes. The deposition methods of the analyzed films were adjusted to fabricate a morphology with a high surface area to improve light absorption and facilitate charge transfer to the solid-liquid interface. FIB-SEM tomography allows measuring the surface area of the exact structure, without any

assumptions. The accuracy of the measurement is only limited by the resolution of the SEM image and the accuracy of the ion beam milling. The collected morphology data was used to obtain the total surface area of the overall solid phase. In addition, we also used the method to assess the surface area of the LTON in contact with the electrolyte, LTON (I), the surface area without the contribution from the nano-pores, LTON (II), and the surface area of the LTON particles without pores and TiO_2 necking, LTON (III). The results are shown in Figure 2.7a.

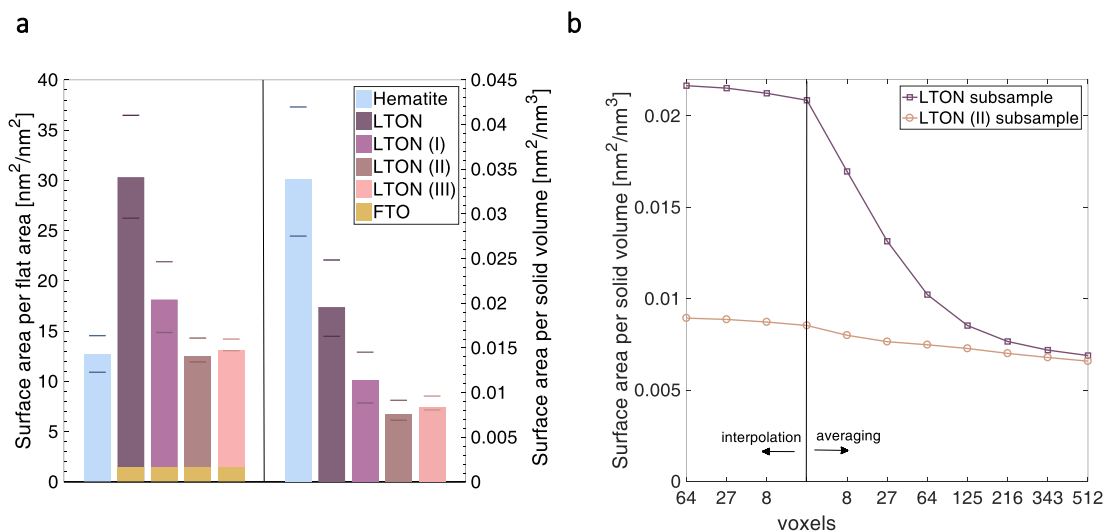


Figure 2.7 (a) Surface area per flat area (roughness factor) and per solid volume for $\alpha\text{-Fe}_2\text{O}_3$, and LTON. LTON (I): surface areas of nano-pores not connected to the bulk electrolyte were neglected, LTON (II): surface areas of LTON particles, neglecting the contributions of nano-pores, LTON (III): LTON particles without nano-pores and necking. The error bounds indicate a lower bound segmentation threshold ($\alpha\text{-Fe}_2\text{O}_3$: 100, LTON: 78) and an upper bound segmentation threshold ($\alpha\text{-Fe}_2\text{O}_3$: 150, LTON: 106), to quantify the effect of the uncertainty in the segmentation process. (b) Mesh density study of surface area calculations. For subsamples ($500 \times 500 \times 500$ voxels) of the LTON and LTON (II), the surface area per solid volume is shown for different mesh densities.

The hematite ‘cauliflower’ structure showed a film roughness factor (surface area per flat xy -plane area) of 12.7. The LTON electrode had a film roughness factor of 30.3, but more than half of this was accounted for by the nano-pore network within the particles. Without the surface area of the nano-pores, the film roughness factor decreased to 12.5. Our calculations also showed that the necking between the particles decreases the surface roughness only slightly, by a value of 1.3.

When we considered all the interfaces in contact with the electrolyte to be active, including the nano-pores connected to the inter-particle space, the film roughness was 18.2. For the LTON sample, some areas of the FTO substrate remained uncovered, which contributed a value of 1.4 to the roughness factor. In Figure 2.7a, error bounds are indicated for each computed case showing two extreme values for the threshold, with a lower bound segmentation threshold (α -Fe₂O₃: 100, LTON: 78) and an upper bound segmentation threshold (α -Fe₂O₃: 150, LTON: 106). The comparison of the error bounds also shows that most of the uncertainty for the computed surface area is rooted in the segmentation process of the nano-pores.

When evaluating the results as surface area per semiconductor volume (excluding the surface and volume contributions of the FTO), the highest value was found for the hematite sample, $3.382 \cdot 10^{-2} \text{ nm}^{-1}$ compared to LTON = $1.958 \cdot 10^{-2} \text{ nm}^{-1}$. The specific surface of the LTON in direct contact with the percolating electrolyte was $1.133 \cdot 10^{-2} \text{ nm}^{-1}$. The specific surface of the LTON without nano-pores was $7.51 \cdot 10^{-3} \text{ nm}^{-1}$. Converting the results to surface area per weight, this leads to $6.567 \text{ m}^2/\text{g}$ for α -Fe₂O₃ and $3.169 \text{ m}^2/\text{g}$ for LTON (using a bulk density for α -Fe₂O₃ of $5.15 \cdot 10^{-12} \text{ g}/\mu\text{m}^3$ for LTON of $6.18 \cdot 10^{-12} \text{ g}/\mu\text{m}^3$). Our calculated values agree qualitatively with reported measurement results. The measured value for the surface roughness factor for hematite (measurement method not specified) has been reported to be approximately 24 [7], and the specific surface area for LTON (BET method) has been reported to be $14.2 \text{ m}^2/\text{g}$ [8].

The FIB-SEM spatial resolution is the limiting factor for a more accurate calculation of the surface areas. Therefore, a mesh density study for the surface area calculations was done. For subsamples of the LTON and LTON(II) (sample size: 500 x 500 x 500 voxels), the surface area per solid volume is shown for different mesh densities in Figure 2.7b. The coarsening of the mesh was achieved by averaging neighboring voxels, whereas the refinement was done by bicubic interpolation. The FIB-SEM resolution is shown to be sufficient to determine an accurate surface area for the LTON(II) (without nano-pores), as the surface area decreases only by 6% for an averaging of 8 voxels. The bicubic interpolation mainly represents a smoothing process of the mesh, and the deviation in the surface area stays within 5% for a refinement of 64 (4 x 4 x 4) per voxel. In the case of the LTON with nano-pores, the calculations suggest that the FIB-SEM resolution was not high enough to prove surface mesh convergence. In the first averaging step, a decrease in the surface area by 19% was observed. The limiting FIB-SEM resolution explains the smaller calculated surface area compared to the experimental BET measurement. The smoothing process had only a small effect on the final result by an increase of 4% for a refinement of 64 per voxel.

Size Distribution of the Semiconductor-Phase, Pore-Space, and Necking

It is difficult to experimentally measure characteristic feature sizes and to quantify their distribution, especially for PEC electrodes with complex morphologies. The opening size distribution method, applied to the semiconducting phase of the segmented dataset, is capable of computationally quantifying the shortest diameter of every feature and thus indicates an average of the maximum path length for the minority carriers to reach the solid-electrolyte interface. For the hematite electrode, the mean feature diameter is 74 nm [$d_{\min}=0$ nm, $d_{\max}=144$ nm] (Figure 2.8a). In Figure 2.8b, the opening size distribution for the semiconducting phase of the LTON film is shown. The nano-pores in the individual particles were not considered in order to quantify the typical LTON particle size. The average characteristic feature size was 441 nm [$d_{\min}=0$ nm, $d_{\max}=800$ nm].

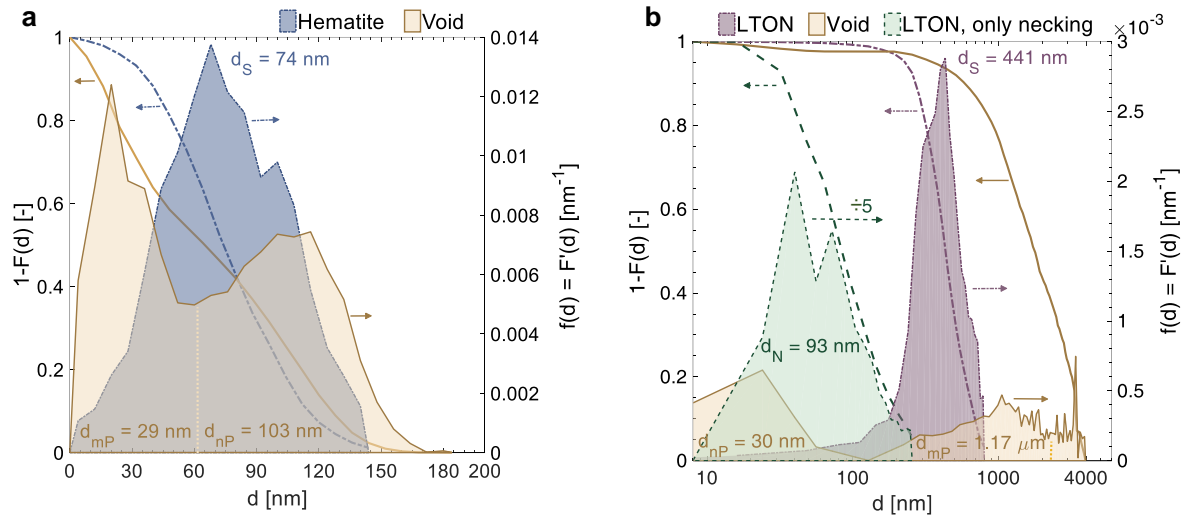


Figure 2.8 Cumulative opening size distribution (left y-axis) and probability opening size distribution (right y-axis) of the semiconductor films. (a) $\alpha\text{-Fe}_2\text{O}_3$ semiconducting phase (blue) and pore space (yellow). (b) LTON semiconducting phase with necking (violet), pore space (yellow), and TiO_2 necking phase without LTON phase (green). The TiO_2 probability opening size distribution has been scaled down by a factor of 5.

The pore space, filled with electrolyte in the operating PEC electrode (as long as the pore network is percolating and the capillary pressure is high enough for the electrolyte to penetrate the smallest

pores), had a mean diameter between hematite branches of 29 nm [$d_{\min}=0$ nm, $d_{\max}=60$ nm]. The mean diameter of the pore space, due to inhomogeneity of film thickness, i.e., between the thinnest and thickest film region, was 103 nm [$d_{\min}=60$ nm, $d_{\max}=185$ nm]. The pore space of the LTON film was divided into three different length scales: the nano-pores (nP), the micro-pores (mP) and the length scale of the inhomogeneity of the LTON film. The nano-pores within the LTON particles had a mean diameter of 30 nm [$d_{\min}=0$ nm, $d_{\max}=128$ nm]. The micro-pores, defined as the space between the individual LTON particles, had a mean diameter of 1.17 μm [$d_{\min}=128$ nm, $d_{\max}=2$ μm]. The mean characteristic diameter of the pore volume developing between the thickest and thinnest region of the film had a mean diameter of 3.03 μm [$d_{\min}=2$ μm , $d_{\max}=4$ μm].

The opening size distribution of the necking phase (TiO_2) in the LTON electrode revealed that the average diameter of the necking was 93 nm [$d_{\min}=0$ nm, $d_{\max}=256$ nm]. Together with the results from the volume fraction profile, these small sizes of the necking patches indicate that, apart from the first layer of LTON particles (well-connected to the FTO), the charge generated in particles higher up in the film must be transported through multiple TiO_2 necking patches, and particles before reaching the FTO substrate.

2.4.2 Feature Characterization on Multiple Scales

One strength of the FIB-SEM tomography is the data acquisition over a large volume (in the scale of tens of cubic micrometers) while ensuring high resolution (in the nanometer scale). The same 3D data set can be used to characterize various morphological features on different scales. Applied to the LTON photoelectrode, the dimensions, shapes, and orientations of the individual LTON particles (micrometer scale) and the nano-pores (pores within the hosting LTON particle in nanometer scale) were quantified.

For the particle analysis, individual particles had to be identified within the interconnected particle network. For the nano-pore analysis, the individual nano-pores needed to be assigned to the hosting particles. However, a proper segmentation of the particles posed difficulties due to the plate-like shapes of the particles, high aspect ratios, and locally dense stacking. For this purpose, we developed an algorithm to fit ellipsoids, grown from manually placed seed points, into the data set. Before applying this algorithm, the nano-pores were artificially eliminated with a low pass filter. In Figure 2.9, the computed ellipsoids in the LTON geometry are visualized.

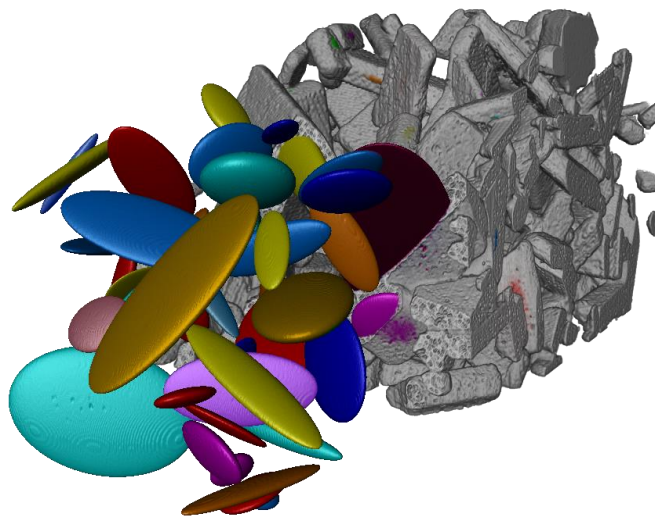


Figure 2.9 3D rendering of ellipsoids fitted into the particles of the LTON photoelectrode. Particles that crossed the boundary of the measured domain were not considered. The ellipsoids were used to characterize the LTON particles in the photoelectrode film.

LTON Electrode: Particle Characterization

Non-overlapping ellipsoids were fitted into all the particles that did not cross the boundary of the considered subvolume (width=23.6 μm , depth=7.9 μm , height=8 μm). 68 ellipsoids were fitted, each representing a LTON particle. Since the shape of the analyzed LTON particles was dictated by the crystal structure of the precursor oxide LaTi_2O_7 (LTO), the three ellipsoid axes could be associated with crystal axes of the LTO and the LTON unit cell. Lognormal distributions approximated the resulting distribution of ellipsoid diameters along the directions of the three semi-axes and are shown in Figure 2.10a. The shortest diameter of the ellipsoid, d_s , was confined between 100 nm and 500 nm, with a mean of 272 nm and standard deviation (SD) of 88 nm. This result confirms and quantifies the narrow range of d_s , which is explained by a known cleavage plane, normal to the shortest particle diameter, with weak bonds in the initial LTO particles [27]. The mean of 272 nm is slightly smaller than the mean diameter calculated by the opening size distribution. The difference is rooted in particles that are closely stacked together and thus are not distinguished as two entities by the opening size distribution method. The intermediate, d_i , and longest, d_l , ellipsoid diameters were distributed over a larger range, with maximum values up to 2 μm and 4 μm , respectively ($d_{i,\text{mean}}=932$ nm, $\text{SD}_i=427$ nm; $d_{l,\text{mean}}=1789$ nm, $\text{SD}_l=773$ nm). The distributions are an indicator of high aspect ratio particles. The aspect ratios are quantified in

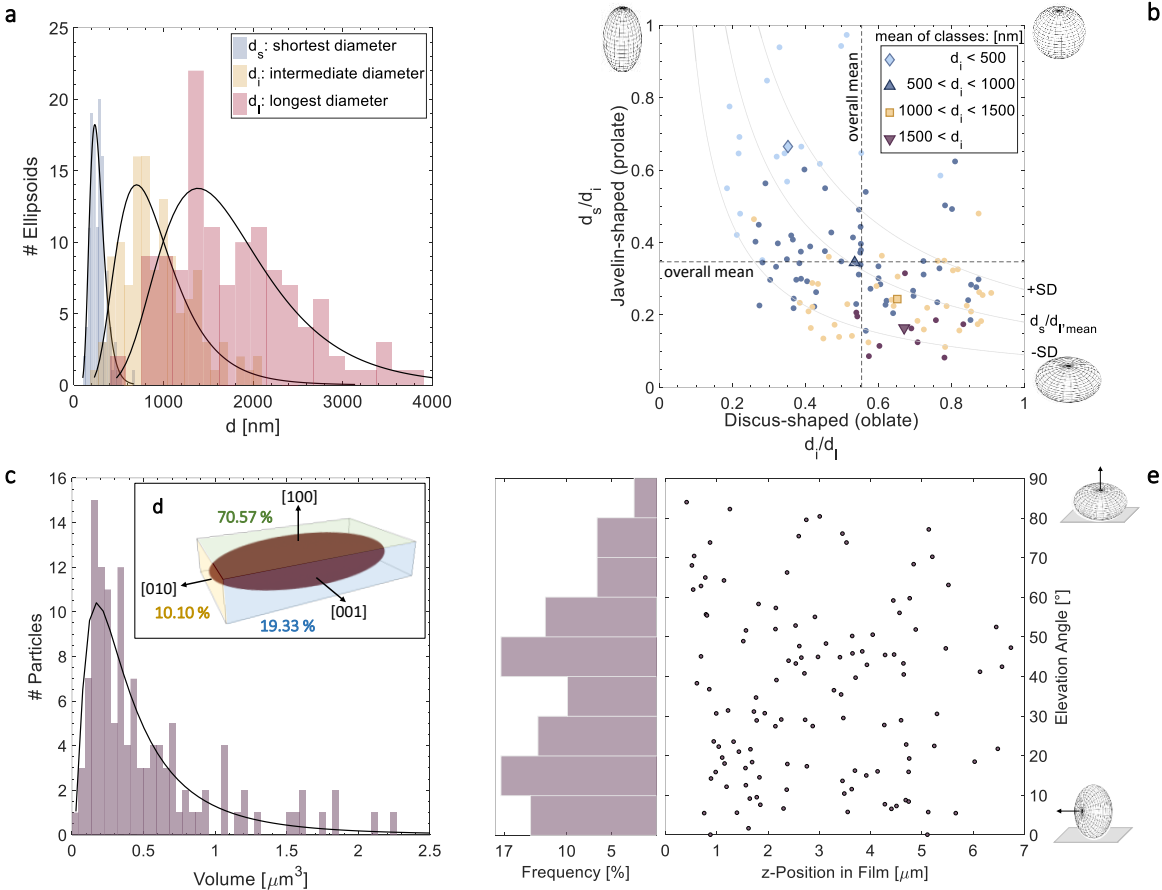


Figure 2.10 LTON particle characterization based on ellipsoids. (a) Size distribution of the three ellipsoid diameters with lognormal distributions: $d_{s,\text{mean}}=272$ nm, $d_{s,\text{SD}}=88$ nm; $d_{i,\text{mean}}=932$ nm, $d_{i,\text{SD}}=427$ nm; $d_{l,\text{mean}}=1789$ nm, $d_{l,\text{SD}}=773$ nm. (b) Shape analysis of the computed ellipsoids. The ellipsoids are divided into 4 classes based on the length of the intermediate diameter. The mean value shifts from prolate to oblate shapes for classes with larger d_i . Overall, the ratio d_s/d_i stays constant. Isolines for d_s/d_i are shown for the mean \pm SD. (c) Particle volume distribution (volumes of the smallest box in which the ellipsoid fits). Lognormal distribution: mean = $0.521 \mu\text{m}^3$, SD = $0.544 \mu\text{m}^3$, median = $0.338 \mu\text{m}^3$. (d) Box surrounding an ellipsoid. Surface fractions of the correlated crystallographic planes integrated over all considered particles. (e) Particle orientation determined by the direction of the smallest diameter. Elevation angle = 90° : particle lies flat on the FTO glass, and elevation angle = 0° : particle stands upright relative to the FTO glass. The scatter plot demonstrates no trend of particle orientation as a function of z -position.

Figure 2.10b. Overall, a high aspect ratio for d_s/d_i was found, with a mean of 0.35, and a moderate aspect ratio was found for d_i/d_l with a mean of 0.55. The results were grouped according to the length of d_l into 4 classes of 500 nm intervals. The mean values, calculated for each class, showed a significant trend from prolate shapes to oblate shapes as d_l increased. The ratio d_s/d_l was fixed within a narrow range (lognormal distribution: mean=0.18, SD=0.09), indicating that the thicker monocrystalline particles can sustain a longer extension along the d_l semi-axis. These results agree with the qualitative findings of a Transmission Electron Microscopy (TEM) study on the particle shape for LTON [27] and highlight the additional advantage of strongly improved statistics. This quantitative information on particle shape delivers novel input for the understanding and control of single crystal particle growth modes in LTON.

Based on the ellipsoid fitting, the particle volume distribution was estimated by assuming cubically shaped particles (Figure 2.10c). In this case, the volume of the particles can be approximated by the volume of the box surrounding the ellipsoid. The lognormal distribution function had a mean of $0.521 \mu\text{m}^3$, a standard deviation of $0.544 \mu\text{m}^3$, and a median of $0.338 \mu\text{m}^3$.

Quantifying the bounding boxes allows the estimation of the areas of specific surface plane types. Pokrant et al. [27] correlated specific crystallographic planes with LTON particle faces and found that the biggest surface corresponds to the (100) plane, the medium surface to the (001) plane and the smallest surface to the (010) plane (Figure 2.11a). The referred study was done using selected-area diffraction (SAD). Due to the high aspect ratio, the LTON particles could be placed in-plane (intermediate and longest axis parallel to substrate) for the SAD measurements. Under broad, parallel electron illumination, the lattice reflection of the crystalline particles showed as sharp diffraction spots. Matching the results with simulated diffraction patterns in [100] direction allowed to correlate the particle faces with the crystallographic planes. Following this model, we quantified the ratio of these surface types by evaluating the surface areas of the boxes surrounding the identified ellipsoids. Assuming non-touching particles, the (100) plane accounted for up to 70.57% of the overall outer particle surface, the (001) 19.33%, and the (010) 10.10% (Figure 2.10d). As the particles mostly touch from corner to plane, and not plane to plane, the given ratios are also valid for the real LTON photoelectrode. If one knows the activity of the surface plane types, for example by ab-initio calculations, then the results here are key to estimate the performance potential of LTON particles and electrodes.

Using the eigenvectors of the ellipsoid radii, the orientation of the particles with respect to the FTO substrate was determined (Figure 2.10e). Due to their plate-like nature, the orientation of the particles was quantified using the smallest diameter axis (standing normal on the largest

particle surface). The smallest diameter vector is perpendicular to the electrode plane for a particle lying flat on the FTO glass, and an elevation angle of 90° was assigned. The elevation angle was set to 0° for a particle standing on an edge (i.e., the smallest diameter vector is parallel to the FTO substrate). No trend of particle orientation as a function of the z -position in the film was found. Only a small percentage of particles laid flat or almost flat in the film. For the most part, the normal vectors of the particles were elevated by 10° or 45° . This is a desirable result, as the incoming light is absorbed along the long axes of the particles, the minority carriers have a short way to the electrolyte, and the majority carriers have to pass through fewer TiO_2 necking patches.

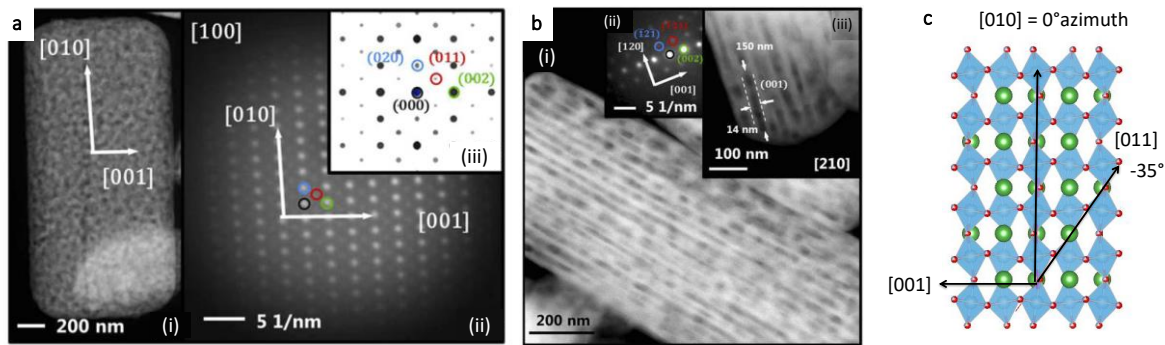


Figure 2.11 Results reprinted with permission from reference [27]. (a) (i) Scanning transmission electron microscopy (STEM) image of LTON particle, (ii) patterns measured by selected-area diffraction (SAD). (iii) simulated diffraction patterns in [100] direction. (b) (i) STEM image of particle viewed in [210] direction, (ii) SAD pattern, (iii) dimensions of a pore. (c) Projection of a typically-shaped monocrystalline LTON particle in [100] direction consisting of three unit cells in [001], two unit cells in [010] and two unit cells in [001] direction. Green are the La positions, blue are the O positions and orange are the N positions; the red are the Ti atoms. O and N share unit cell positions. The pore elongation direction [011] is shown.

LTON Electrode: Nano-pore Characterization

The pore network within the particles of *sample (ii)* forms during the powder ammonolysis step from LTO to LTON in order to make up for the reduction of the unit cell volume by 14% [27]. The inner porosity (volume fraction within the ellipsoid volume, i.e., neglecting particle boundary effects) was calculated for 68 individual particles, and an average value of 10% was obtained with a standard deviation of 0.02. This value agrees well with a calculated inner porosity of 9%, based on a complementing TEM tomography of a single LTON particle (TEM resolution of $7 \times 7 \times 7$

nm³). Our calculations predict that 34.1% of the total nano-pore volume within the particles is connected with the inter-particle void space, and thus, is filled with electrolyte during operation.

Pokrant et al. [27] found in their STEM analysis that the nano-pores were often elongated in one direction by several tenths of a nanometer versus several nanometers (Figure 2.11b). They correlated the main pore elongation to a crystallographic direction and proposed the direction [120]. We quantified the nano-pore orientations relative to the orientation of the hosting particle for a much larger number of pores with the exact 3D morphology data set. All nano-pores within four different LTON particles were analyzed. Only pores situated within the volume of the ellipsoid fitting the particle were considered (Figure 2.12a). An azimuth and an elevation angle of 0° corresponded to an elongated pore directed along the *x*-axis, the direction of the longest particle diameter *d*. The calculated pore orientations were translated into crystallographic directions based on an orthorhombic LTON unit-cell with unit-cell parameters: *a*=5.57137 Å ([100]), *b*=7.8790 Å ([010]), and *c*=5.60279 Å ([001]) [28]. Figure 2.12b shows the 2D histogram of the relative nano-pore orientations based on all pores in 4 particles with a volume greater than 30 voxels. The volume threshold filtered out small pores for which the algorithm was not able to determine the orientation. The frequency of the elevation angles was normally distributed around 0°. Considering only the elevation angles between 0° and 5°, an overall maximum in the azimuth angle distribution was found at -30° and the corresponding local maximum at 150° was shifted by +180°. A high number of pores was elongated in the [010] direction, which corresponds to the longest semi-axis of the particle. However, the 2D histogram revealed that the pore orientations along the [011] direction belong to the most frequent elongation direction. With this result, we quantitatively confirmed the qualitative TEM-based hypothesis [27] that the nano-pore elongation direction follows a major crystal axis. However, our calculations suggest an elongation direction along the [011] direction. We also proved that we are able to analyze complex 3D porous networks utilizing FIB-SEM tomography with a higher resolution than 10 nm.

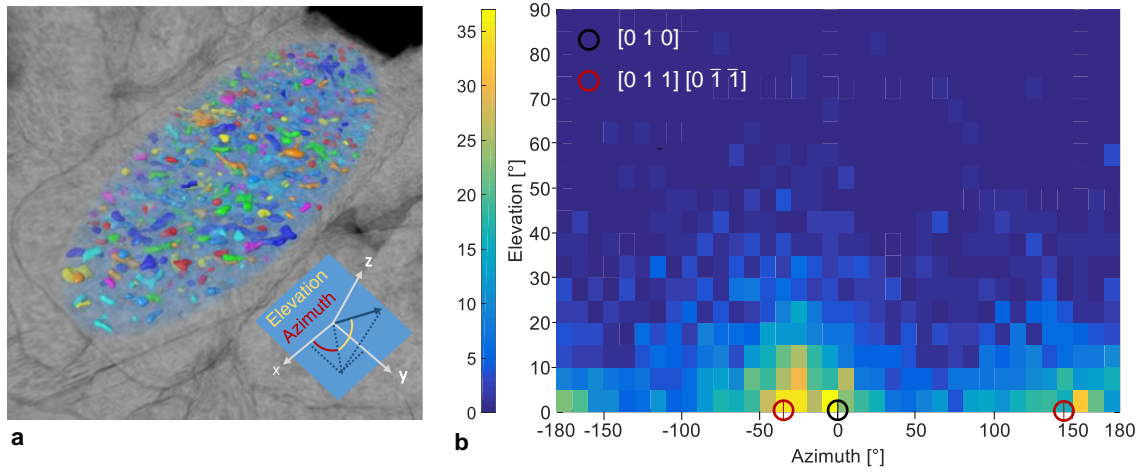


Figure 2.12 (a) Rendering of an ellipsoid (blue) fitted into a LTON particle. Nano-pores within the ellipsoid were identified and labeled. The semi-axes correspond to crystallography directions of $x=[010]$, $y=[001]$, and $z=[100]$. An azimuth and an elevation angle of 0° corresponds to the direction of the x-axis. The pores in the network were separated using water-shedding and visualized with individual colors. (b) 2D histogram of the nano-pore orientations in 4 different LTON particles relative to the orientation of the hosting particle. Three crystallography directions are indicated. The nano-pores are most frequently elongated in the $[011]$ direction.

2.5 Conclusions

We provide the first quantitative analysis of the structure of two morphologically-complex photoelectrodes: a particle-based lanthanum titanium oxynitride electrode with a film thickness of a few micrometers, and a ‘cauliflower-like’ structured hematite electrode with a film thickness of a few hundred nanometers. We used a combined experimental-numerical approach in which we obtained the exact structural information by destructive, ex-situ FIB-SEM tomography and digitalized the structure utilizing advanced post-processing and segmentation algorithms. We then used various computational algorithms to quantify the morphological properties on multiple scales: *i)* the solid phase material distribution along the electrode thickness, specific surface, mean feature dimensions, and film homogeneity on the meso-scale; *ii)* particle shapes, surfaces, volumes and orientations on the micro-scale; and *iii)* nano-pore volumes and orientations on the nano-scale.

Detailed semiconductor material distribution profiles along the electrode thickness were obtained, which can provide relevant information for light absorption calculations. Surface characterizations on the exact geometry allowed decoupling of contributions from the micro-scale features and the nano-scale pores, suggesting that the connected nano-pore surfaces represent 31% of the overall surface. Advanced segmentation of the tomography data, based on machine learning algorithms which can distinguish different grey value patterns, led to the identification of the TiO₂ necking phase in the LTON electrode and revealed that necking spans short distances between particles only. These results prove that majority carriers must be transported through multiple particles and necking patches in order to reach the FTO back-contact. An algorithm was developed which performs ellipsoid fitting into the particle-based LTON structure. This algorithm allows for the identification and characterization of individual particles in the highly interconnected particle network. Quantitative characterization of single LTON particles was then obtained by calculating frequency distributions of particle diameters and volumes, as well as particle shapes and orientations. The surface area of the particles was calculated and contributions from the characteristic particle facets, which are linked to crystallographic planes, were estimated. The high resolution of the FIB-SEM tomography gave quantitative insight into the nano-pore volumes within the LTON particles and allowed determination of the crystallographic directions, to which the pores were preferentially elongated.

This study provides the first in-depth geometrical quantification of morphologically-complex photoelectrodes. The method we developed provides the tools for direct pore-level simulations

Quantitative Structural Analysis of Morphologically Complex Electrodes

in morphologically-complex photoelectrodes and contributes to guiding the morphology and fabrication of optimized photoelectrodes with enhanced performance.

2.6 References

- [1] S. Suter, M. Cantoni, Y. K. Gaudy, S. Pokrant, and S. Haussener, "Linking morphology and multi-physical transport in structured photoelectrodes," *Sustain. Energy Fuels*, pp. 2661–2673, 2018.
- [2] P. Zhang, L. Gao, X. Song, and J. Sun, "Micro- and Nanostructures of Photoelectrodes for Solar-Driven Water Splitting," *Adv. Mater.*, vol. 27, no. 3, pp. 1521–4095, 2014.
- [3] S. Chen, S. S. Thind, and A. Chen, "Nanostructured materials for water splitting - State of the art and future needs: A mini-review," *Electrochem. commun.*, vol. 63, pp. 10–17, 2016.
- [4] M. G. Lee, J. S. Park, and H. W. Jang, "Solution-processed metal oxide thin film nanostructures for water splitting photoelectrodes: A review," *J. Korean Ceram. Soc.*, vol. 55, no. 3, pp. 185–202, 2018.
- [5] H. R. Kim, G. Kim, S. Il In, and Y. Park, "Optimization of porous BiVO₄ photoanode from electrodeposited Bi electrode: Structural factors affecting photoelectrochemical performance," *Electrochim. Acta*, vol. 189, pp. 252–258, 2016.
- [6] A. Kay, I. Cesar, and M. Grätzel, "New benchmark for water photooxidation by nanostructured alpha-Fe₂O₃ films," *J. Am. Chem. Soc.*, vol. 128, no. 49, pp. 15714–21, 2006.
- [7] S. C. Warren *et al.*, "Identifying champion nanostructures for solar water-splitting," *Nat. Mater.*, vol. 12, no. 9, pp. 842–9, 2013.
- [8] S. Landsmann, A. E. Maegli, M. Trottmann, C. Battaglia, A. Weidenkaff, and S. Pokrant, "Design Guidelines for High-Performance Particle-Based Photoanodes for Water Splitting: Lanthanum Titanium Oxynitride as a Model," *ChemSusChem*, vol. 8, no. 20, pp. 3451–3458, Oct. 2015.
- [9] S. Haussener, W. Lipinski, J. Petrasch, P. Wyss, and a. Steinfeld, "Tomographic Characterization of a Semitransparent-Particle Packed Bed and Determination of its Thermal Radiative Properties," *J. Heat Transfer*, vol. 131, no. 7, p. 072701, 2009.
- [10] S. Suter, A. Steinfeld, and S. Haussener, "Pore-level engineering of macroporous media for increased performance of solar-driven thermochemical fuel processing," *Int. J. Heat Mass Transf.*, vol. 78, pp. 688–698, 2014.
- [11] V. De Andrade *et al.*, "Nanoscale 3D imaging at the Advanced Photon Source," *SPIE Newsroom*, pp. 2–4, 2016.
- [12] L. Zielke *et al.*, "Three-phase multiscale modeling of a LiCoO₂ cathode: Combining the advantages of FIB-SEM imaging and X-ray tomography," *Adv. Energy Mater.*, vol. 5, no. 5, pp. 1–8, 2015.

- [13] S. Gaboreau, J. C. Robinet, and D. Prêt, “Optimization of pore-network characterization of a compacted clay material by TEM and FIB/SEM imaging,” *Microporous Mesoporous Mater.*, vol. 224, pp. 116–128, 2016.
- [14] W. Li, W. Ding, G. Ji, L. Wang, J. Zhang, and F. Sun, “Three-dimensional visualization of arsenic stimulated mouse liver sinusoidal by FIB-SEM approach,” *Protein Cell*, vol. 7, no. 3, pp. 227–232, 2016.
- [15] S. Dilger, S. Landsmann, M. Trottmann, and S. Pokrant, “Carbon containing conductive networks in composite particle-based photoanodes for solar water splitting,” *J. Mater. Chem. A*, vol. 4, no. 43, pp. 17087–17095, 2016.
- [16] M. Cantoni and L. Holzer, “Advances in 3D focused ion beam tomography,” *MRS Bull.*, vol. 39, no. 04, pp. 354–360, 2014.
- [17] J. Schindelin *et al.*, “Fiji: an open-source platform for biological-image analysis,” *Nat. Methods*, vol. 9, no. 7, pp. 676–682, 2012.
- [18] Q. Tseng *et al.*, “A new micropatterning method of soft substrates reveals that different tumorigenic signals can promote or reduce cell contraction levels,” *Lab Chip*, vol. 11, no. 13, p. 2231, 2011.
- [19] I. Arganda-Carreras, V. Kaynig, C. Rueden, A. Schindelin, Johannes Cardona, and H. S. Seung, “Trainable_Segmentation: Release v3.1.2,” 2016. [Online]. Available: <https://doi.org/10.5281/zenodo.59290>.
- [20] K. Zuiderveld, *Contrast limited adaptive histogram equalization*. Academic Press Professional, Inc., 1994.
- [21] W. E. Lorensen and H. E. Cline, “Marching cubes: A high resolution 3D surface construction algorithm,” *ACM SIGGRAPH Comput. Graph.*, vol. 21, no. 4, pp. 163–169, 1987.
- [22] H. J. Vogel, “Morphological determination of pore connectivity as a function of pore size using serial sections,” *Eur. J. Soil Sci.*, vol. 48, no. 3, pp. 365–377, 1997.
- [23] P. Soille, *Morphological image analysis: principles and applications*. Springer Science & Business Media, 2013.
- [24] M. Doube, “The ellipsoid factor for quantification of rods, plates, and intermediate forms in 3D geometries,” *Front. Endocrinol. (Lausanne)*, vol. 6, no. FEB, pp. 1–5, 2015.
- [25] M. Doube *et al.*, “BoneJ: Free and extensible bone image analysis in ImageJ,” *Bone*, vol. 47, no. 6, pp. 1076–1079, 2010.
- [26] M. Longair, “Find Connected Regions.” [Online]. Available: <https://www.longair.net/edinburgh/imagej/find-connected-regions/>.

- [27] S. Pokrant, S. Dilger, and S. Landsmann, “Morphology and mesopores in photoelectrochemically active LaTiO₂N single crystals,” *J. Mater. Res.*, vol. 31, no. 11, pp. 1574–1579, 2016.
- [28] M. Yashima, M. Saito, H. Nakano, T. Takata, K. Ogisu, and K. Domen, “Imma perovskite-type oxynitride LaTiO₂N: structure and electron density,” *Chem. Commun.*, vol. 46, no. 26, p. 4704, 2010.

Linking Morphology and Multi-Physical Transport in LTON Photoanodes

The content of this chapter is adapted with permission from The Royal Society of Chemistry from an article by Silvan Suter, Marco Cantoni, Yannick Gaudy, Simone Pokrant and Sophia Haussener published 2018 in Sustainable Energy and Fuels [1].

3.1 Introduction

No single material has been found to efficiently and stably split water via photoelectrochemical (PEC) approaches while simultaneously ensuring scalability at low costs [2]. Stable and abundant semiconductors exist, but their water-splitting efficiencies are far below their theoretical maximum [3]. Nano and micro-structuring of materials have been pursued in order to circumvent some of the critical limitations of bulk material properties [4]. Hole diffusion lengths in photoanodes with orders of magnitude smaller values than the material specific absorption length of light are common [5]. Optimal morphology can lead to enhanced solar absorption, increased surface area, and shorter minority carrier migration paths. In well-controlled multi-step processes, which create structured multi-dimensional arrays like nanotubes [6], nanowires [7], or 3D structures like micron pillars [8], the decoupling of light absorption and charge transport can be achieved. In these morphologies, the light absorption along the vertical axis is enhanced, while orthogonally, minority charge carriers have a relatively short path to the semiconductor-electrolyte interface [9]. The morphological characterization of these structures is relatively straightforward due to the regularity of the patterns, and optimization of feature dimensions and

array layouts have been reported [10], [11]. Due to the decoupling of the light absorption and the charge transport, the morphology can be optimized for each physical phenomenon separately. However, the fabrication of these well-defined structures can be expensive or not possible, depending on the used materials and processing routes. Less expensive or less controllable fabrication steps can result in extremely complicated photoelectrodes with irregular and complex morphologies. Examples are the ‘cauliflower’ shaped hematite nanopillars with a complex surface area [12] and a multi-layered LaTiO_2N particle network on FTO [13]. Both photoanodes were introduced in the previous chapter.

In general, the geometries of complex photoelectrode morphologies have so far not been quantified on a nanoscale using tomography data, and the understanding of the influence of the morphology on the water-splitting performance is limited. In the case of LTON photoanodes, a study has shown a decrease of photocurrent for an increase in the thickness of the particle stack [14]. It was suggested that mass transport limitations start to dominate before the maximum light absorption was reached. When aiming to improve the efficiency of a photoelectrode, the light absorption, photogenerated carrier collection, ion transport, and catalysis must be optimized simultaneously [3]. However, the structuring of the electrode can be beneficial to some of these transport phenomena, and disadvantageous to others. The effects are coupled, and a combination of experimental and numerical work is needed to understand the coupling and to optimize the structure for increased efficiency [15]. In other fields, studies on mesoporous materials have relied on exact geometries acquired by X-ray tomography or FIB-SEM tomography. In the solid oxide fuel cell research, FIB-SEM data have been mostly used to quantify the structure of the gas diffusion layer [16], [17], and connectivity analyses have provided values for the tortuosity [18]. Also in the field of lithium-ion batteries, tomography data sets have provided the information for topology studies [19] and the base for detailed electrochemical simulations to study the effect of the microstructure on the battery performance [20], and its degradation [21].

Here we propose direct pore-level simulations on the exact geometries of complex photoanodes to characterize multi-physical transport in the mesoporous film structure and identify transport limitations. Based on the 3D FIB-SEM tomography data acquired and presented in the previous chapter, finite volume calculations were performed. In the present chapter, the methodology is demonstrated on structured LTON photoanodes used for photoelectrochemical water-splitting. The outcome of this study facilitates the identification of structural performance limitations and the development of morphology guidelines for performance enhancement.

3.2 Morphology and Representative Volumes

The digitalized geometry of the LaTiO₂N (LTON) photoanode analyzed in *Chapter 2* was used for the calculations of the multi-physical transport. The overall domain measured by the FIB-SEM had the dimensions of 8 x 8 x 31 μm^3 . Doing finite volume calculations on detailed, complex geometries requires a lot of memory, and therefore, it is critical to keep the computational domain size as small as possible. Based on morphological properties, an initial study was conducted to find a representative volume (RV). We defined the RV as the smallest subvolume of the dataset for which the structural properties, surface and volume fraction, statistically represent the properties of the overall film. The solid volume fraction and the normalized surface area were computed on successively increasing subvolumes in order to determine the RV for the studied photoelectrodes. The volumes had a constant height (the full film thickness) and a fixed aspect ratio of the side lengths, corresponding to the aspect ratio of the full dataset. An initial volume with a depth of 160 nm and a width of 640 nm was defined in the center of the datasets. The volumes were considered representative when the average of the last 10 calculated values of the solid volume fraction and the specific surface area, respectively, stayed within an error band of $\pm 3\%$.

The film roughness factor and the solid fraction are shown for increasing volume sizes in Figure 3.1a. The aspect ratio of the volume width to the depth is kept constant at 4:1. For the LTON electrode, a volume of 64.176 μm^3 (RV: width=5.73 μm , depth=1.4 μm) was required to keep the film roughness and the solid volume fraction within an error band of $\pm 3\%$. As a comparison, the same study was done for the $\alpha\text{-Fe}_2\text{O}_3$ film of *Chapter 2*. For the hematite film, the size of the individual ‘cauliflowers’ was an order of magnitude smaller than the width and depth of the measured data set. The morphology properties stayed within the given error band for a volume greater than 11.904 μm^3 (RV: width=8 μm , depth=2 μm). The LTON RV was much bigger than the RV required for the hematite film due to the bigger feature sizes of the LTON particles. Also, the LTON film showed some inhomogeneity in the film thickness for the measured data set. In order to address the variability of the film thickness in the LTON sample, a subsample with the volume eight times the volume of an RV was chosen. For the subsequent light absorption and transport calculations, the volume fraction distribution along the z -axis, the overall volume fraction, as well as the surface area per flat area are crucial. Three subsamples (1000 x 1000 x 1000 voxels) were created and compared to the overall LTON data set in Figure 3.1b. Subsample 1 has a mean absolute percentage deviation from the overall sample of 8% for the volume fraction distribution. The relative error of the overall volume fraction is 4%, and the center of density is 19% lower. The surface area per flat surface is 10% higher. Subsample 2 has a lower film

thickness, with a mean absolute percentage deviation of 35% for the volume fraction distribution. The relative error of the overall volume fraction is 1.7%, and the center of density is 1.8% higher. The surface area per flat surface is 5% lower. Subsample 3 has a mean absolute percentage deviation of 19% for the volume fraction distribution. The relative error of the overall volume fraction is 3%, and the center of density is 5% higher. The surface area per flat surface is 2% higher. Subsample 1 represented the overall sample well and was used as the domain geometry for the subsequent calculations.

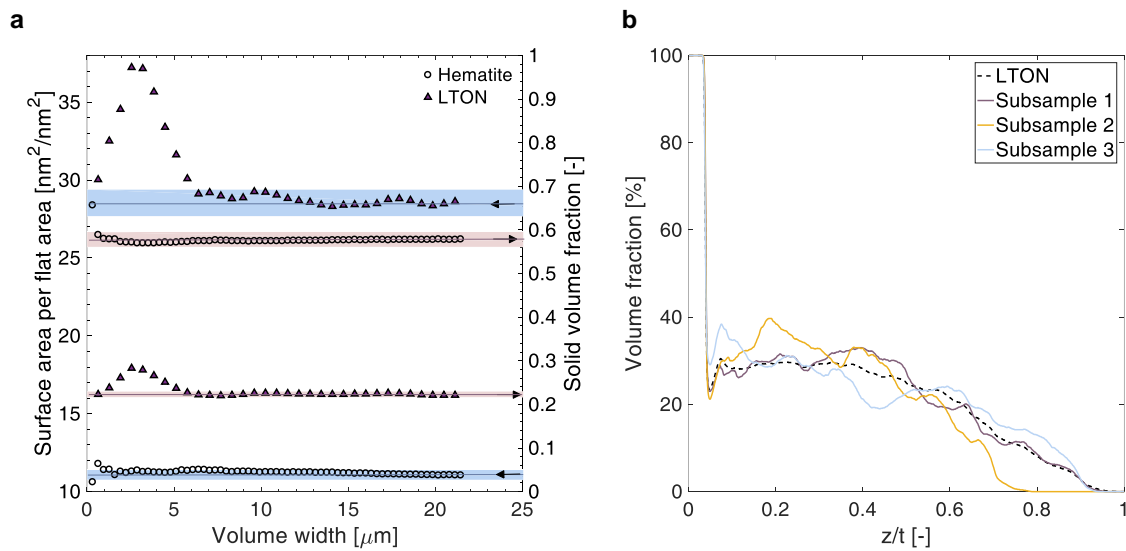


Figure 3.1 (a) For the LTON electrode, a subvolume is representative with a volume larger than $64.176 \mu\text{m}^3$ (RV: width= $5.73 \mu\text{m}$, depth= $1.4 \mu\text{m}$). The aspect ratio of the volume width to the volume depth is 4:1, and the error threshold is $\pm 3\%$. For comparison, the RV study is shown for the $\alpha\text{-Fe}_2\text{O}_3$ film. (b) The volume fractions of three equally sized subsamples ($1000 \times 1000 \times 1000$ voxels) are compared to the volume fraction of the overall film. Subsample 1 represents the overall sample well with a mean absolute percentage deviation of 8% for the volume fraction distribution.

3.3 Governing Equations and Methodology

We considered a representative subvolume of the LTON dataset to model the light absorption for front or back illumination and study the correlating mass transport within the electrolyte of a water-splitting device. The multi-physics were decoupled and modeled in series. First, the electron-hole pair generation rate was calculated using Beer-Lambert's law, considering the solid volume fraction of the semiconductor. The local current densities were then computed under the assumption of 100% internal quantum efficiency. In the last step, the local current densities were used as a boundary condition to solve for the mass transport and species concentrations in the electrolyte. An estimation for bulk species concentrations was finally calculated from the results of the exact morphology by using empirical correlations for known flow cell setups. Figure 3.2 shows a scheme of how the multi-physics are connected in the model domain.

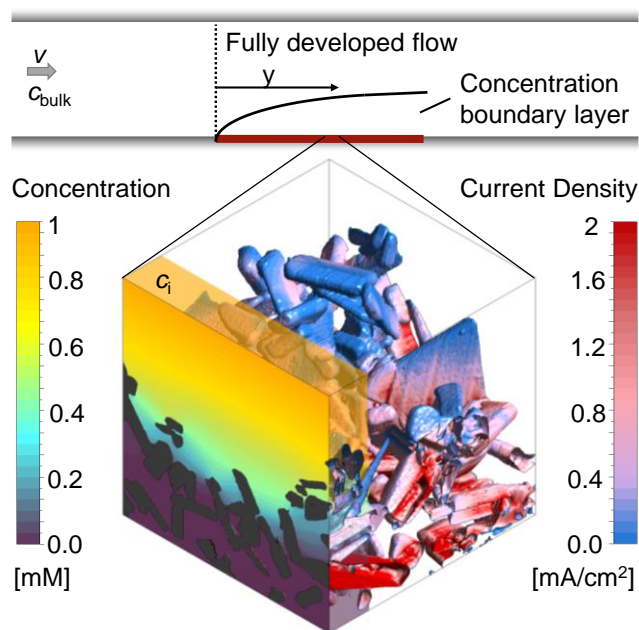


Figure 3.2 Scheme showing the local current densities on the semiconductor-electrolyte interface for simulated back illumination. The species concentrations of OH^- ions are shown in the pore space between the LTON particles. The electrolyte is stagnant in the pore space and by a Sherwood correlation, the contributions of the hydrodynamic boundary layer in a flow cell setup is taken into account to correlate the intermediate concentration c_i to the bulk concentration c_{bulk} .

3.3.1 Electron-Hole Pair Generation Rate

The light absorption was modeled following Beer-Lambert's law with an experimentally determined absorption coefficient. The spectral reflectance, ρ , and the transmittance, τ , of the LTON film were acquired with a UV-3600 Shimadzu UV-VIS-NIR spectrophotometer using an integrating sphere. The LTON sample was illuminated from the side of the FTO glass, and therefore, ρ had to be corrected by the absorbance of the FTO glass: $\rho_c = \rho + a_{\text{FTO}}$. The transmittance and the reflectance of the FTO glass were measured separately, and the absorbance was calculated by $a_{\text{FTO}} = 1 - \rho_{\text{FTO}} - \tau_{\text{FTO}}$. The effective absorption coefficient of LTON was determined using a partially transmitting film with a thickness greater than the wavelength, considering multiple internal reflections [22]:

$$\alpha^*(\lambda) = -\frac{1}{t^*} \ln \left(\frac{\sqrt{(-\rho_c^2 + 2\rho_c + \tau^2 - 1)^2 + 4\tau^2} - \rho_c^2 + 2\rho_c + \tau^2 - 1}{2\tau} \right) \quad (3.1)$$

with the effective thickness given by $t^* = \int_0^t V(z) dz$ where $V(z)$ is the averaged volume fraction profile along the z-direction [23]. The extinction coefficient as a function of the z-position is then given by

$$k(z) = k^* \cdot V(z) = \frac{\alpha^* \lambda \cdot V(z)}{4\pi}. \quad (3.2)$$

The determined absorption coefficient is shown in Figure 3.3.

For the calculation of the generation rate, a subsample of the segmented FIB-SEM data set was discretized in all three directions. For the position $x=i$, $y=j$ and $z=k$, the generation rate per solid volume, $G_{i,j,k}$ was calculated as:

$$g_{i,j,k}(\lambda) = \alpha^*(\lambda) \cdot V_k \cdot P_k(\lambda) \cdot \frac{\lambda}{hc} \quad (3.3)$$

$$P_{k+1}(\lambda) = P_k(\lambda) - g_{i,j,k}(\lambda) \cdot dz \cdot \frac{hc}{\lambda} \quad (3.4)$$

$$G_{i,j,k} = \frac{1}{V_k} \cdot \sum_{\lambda=300nm}^{\lambda_{\text{Bandgap}}} g_{i,j,k}(\lambda) \quad (3.5)$$

where $P_{k=1}(\lambda)$ is the wavelength dependent AM 1.5G solar spectrum. All losses due to absorption in the electrolyte or the FTO layer and glass were not considered. This method does not take into account scattering within the porous structure; however, for highly absorbing materials, the light is absorbed within 1 or 2 particles, minimizing the effect of scattering on the generation rate profile.

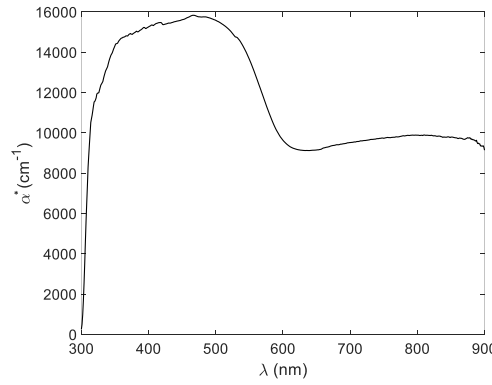


Figure 3.3 Calculated absorption coefficient for LTON, based on measurements and corrected by the solid volume fraction profile.

3.3.2 Local Current Density

The local current density on the semiconductor-electrolyte interface was calculated by solving the Poisson equation in the semiconductor:

$$\nabla \cdot (D \cdot \nabla c) + S_c = 0 \quad (3.6)$$

where c is the charge concentration, D is the diffusion coefficient, and S_c is the source term. The semiconductor phase of the FIB-SEM dataset was meshed using a tetrahedral mesh generator [24], and the Poisson equation was solved with a commercial finite volume solver [25]. The

computed generation rates per solid, $G_{i,j,k}$, were inserted as source terms and the boundary condition at the semiconductor-electrolyte interface was set to $\phi_{\text{interface}}=0$. The resulting charge flux over the interface was taken as the local current density. This method does not take into account any semiconductor physics, but simply distributes the charges to the closest semiconductor-electrolyte interface by choosing a sufficiently small diffusion coefficient. The underlying assumption is 100% internal quantum efficiency. The results were identical for diffusion coefficient values smaller or equal to 10^{-12} cm²/s.

A real internal quantum efficiency for minority charge carriers and limitations of majority charge carriers due to inter-particle connectivity problems were not considered. The purpose of the study is to determine potential mass transport limitations assuming the best case scenario.

3.3.3 Mass Transport

Mass transport of reactants within the void phase of the complex morphology was modeled as diffusion in a stagnant fluid. For the assumptions of zero fluid velocities and infinitely diluted species, the diffusive transport equation was solved until steady state was reached:

$$\frac{\partial c}{\partial t} = \nabla \cdot (D \cdot \nabla c) \quad (3.7)$$

The void phase of the FIB-SEM data set was meshed using a tetrahedral mesh generator [24], and the diffusive transport equation was solved with a commercial finite volume solver [25]. A schematic of the simulation setup is shown in Figure 3.4. An intermediate concentration ϕ was set as a top boundary condition. The side walls had symmetry boundary conditions, and the bottom, which was covered by FTO had a no-flux boundary condition. The calculated local current density was applied as a reactant sink boundary condition onto the electrolyte-semiconductor interface. The boundary flux was given as a step function. For $\phi_{\text{Boundary}} > 0$, the reactant sink rate was equal to the charge flux calculated by the generation rate for a boundary concentration. For $\phi_{\text{Boundary}} = 0$, the sink rate became zero. It was assumed that the photo-induced potential drop occurs only in the space-charge layer of the semiconductor and in the Helmholtz layer [26]. Thus, ions are not driven by an electric field, but only travel by diffusion. This assumption is correct for ionic concentrations in the electrolyte with a small Debye length. For our calculations, the ionic strength in most parts of the domain is high enough to keep the Debye length below 1nm;

however, for the domain regions with near depletion, the Debye length increases and contributions from the electric field through migration were neglected. The mass transport through the macroscopic hydrodynamic boundary layer in a laminar-flow parallel plate cell was taken into account by the experimentally determined Leveque- correlation [27]:

$$Sh = \frac{k_y \cdot d_e}{D} = 0.978 \left(Re \cdot Sc \cdot \frac{d_e}{y} \right)^{\frac{1}{3}} \left(\frac{2}{\gamma + 1} \right)^{\frac{1}{3}} \quad (3.8)$$

The local mass transfer coefficient is k_y at distance y downstream from the front edge of the photoelectrode, and where d_e is the equivalent diameter of the flow cell equal to $2BS/(B+S)$. The Reynolds number is defined as $Re = \rho v d_e / \mu$, where the Schmidt number is defined as $\mu / \rho D$, γ is the aspect ratio S/B , where B is the width and S is the height of the flow cell. The average mass transfer coefficient for the photoelectrode with length L is according to Qi et al. [27] evaluated at $y=8/27L$. The fluid dynamic properties of the electrolyte were taken from water, and the following dimensions were used: $B=1$ cm, $S=0.15$ cm, $L=1$ cm. The intermediate concentration c_i was linked to the bulk concentration c_{bulk} using the mass transfer equation $N = k_y \cdot A_p (c_i - c_{\text{bulk}})$, where N is the total species flux and A_p is the projected flat area of the photoelectrode subsample.

The tortuosity was calculated with the mean path lengths of the reactants divided by the film thickness. 2500 pathlengths were extracted from the derivative of the reactant concentration field. The start points of the pathlengths were uniformly distributed on the plane of the intermediate concentration c_i .

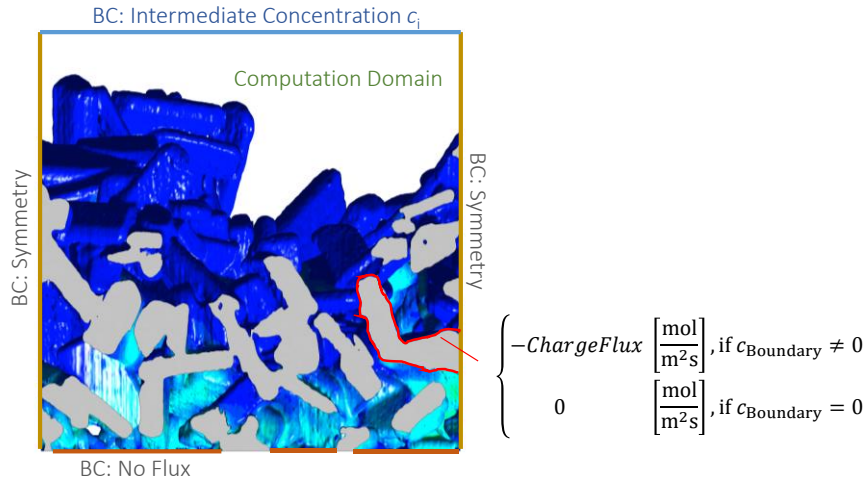


Figure 3.4 An intermediate concentration c_i was set as a top boundary condition. The side walls had symmetry boundary conditions and the bottom, which was covered by FTO had a no-flux boundary condition. The calculated local current density was applied as a reactant sink boundary condition onto the electrolyte-semiconductor interface. The boundary flux was given as a step function. For $c_{\text{Boundary}} > 0$, the reactant sink rate was equal to the charge flux calculated by the generation rate for a boundary concentration. For $c_{\text{Boundary}} = 0$, the sink rate became zero.

3.4 Results and Discussion

3.4.1 Light Absorption and Local Current Density

An isotropic subsample with a volume of $512 \mu\text{m}^3$ was used for the following calculations. The subsample was eight times larger than the representative volume and represented well the key morphological characteristics (volume fraction profile and surface area) of the measured LTON film (Figure 3.1). To model the light absorption, 25 x 25 volume fraction profiles along the z -axis were calculated from the subsample. For each column, the generation rate per solid volume was calculated applying Beer-Lambert's law with a discretization step of 40 nm in the z -direction.

For the wavelength-dependent absorption coefficient (Figure 3.3), and a bandgap of 2.1 eV, 77% of the incident light of the AM1.5G spectrum was absorbed within the LTON film. This result is in agreement with the experimentally determined absorptance of 72.3% [23]. Figure 3.5a shows the generation rates for front and back illumination. The generation rate for front illumination was symmetrically distributed, with a peak just beyond half of the film thickness. In contrast, the generation rate profile for illumination from the backed showed a maximum in the first micrometer and then declined. This difference is directly linked to the morphology, as the first particle layers for the front illumination are much more loosely packed compared to the layers above the FTO glass. Assuming 100% internal quantum efficiency, the generated charges were distributed onto the closest semiconductor-electrolyte interface. The current density distributions are shown in Figure 3.5b. The most frequent current density was $0.12 \text{ mA}/\text{cm}^2$ for front illumination, and $0.17 \text{ mA}/\text{cm}^2$ for back illumination. As expected, the back illumination led to higher maximum local current densities (4.31 mA cm^{-2} for front illumination and 4.99 mA cm^{-2} for back illumination). The calculated current densities represent a best case scenario, where all minority charges reach the electrolyte and the majority charges travel unhindered to the FTO back contact. Experimentally, it has been shown that there is a connectivity problem and that many majority carriers do not make it through multiple particles to the back contact [14]. The structure analysis of *Chapter 2* revealed that the TiO_2 necking is located between the LTON particles throughout the film, but the recombination rate at the interface might be too high. Nevertheless, the assumption of unhindered majority carrier transport is still valid and of interest, as the same study [14] circumvented the connectivity issue by introducing multiwall carbon nanotubes to connect the LTON particles with the back contact.

The measured absorption coefficient showed a weak wavelength dependency between 300 nm and 590 nm (bandgap). Therefore, the generation rate profile was calculated for a constant wavelength-averaged absorption coefficient of $1.4 \cdot 10^4 \text{ cm}^{-1}$. The mean deviation from the exact

profile was 1.1% and 1.6%, for front and back illumination, respectively. Based on this finding, the generation rate profiles and the local current densities were calculated for constant absorption coefficients ranging from $5 \cdot 10^3$ to $1 \cdot 10^5 \text{ cm}^{-1}$ and a constant bandgap of 2.1 eV. The results showed that the influence of the morphology on the generation rate profile increases with higher absorption coefficients. For an absorption coefficient of only $5 \cdot 10^4 \text{ cm}^{-1}$, the shape of the generation rate profile is already dictated by the volume fraction profile. A maximum absorptance of 97.3%, equivalent to a maximum current of 9.5 mA/cm^2 (per flat photoelectrode area), can be reached with a high absorption coefficient of $1 \cdot 10^5 \text{ cm}^{-1}$; the remaining part is always lost due to small areas not covered by any particle. For all absorption coefficients, the maximum current density for front illumination was 9-13% lower than for back illumination. Also, for low absorption coefficients ($< 8 \cdot 10^3 \text{ cm}^{-1}$), evenly distributed current densities with low values ($< 4 \text{ mA/cm}^2$) were found, which is desirable in order to avoid degradation. High absorption coefficients ($> 5 \cdot 10^4 \text{ cm}^{-1}$) resulted in big fractions of the surface area having high current densities, up to 11 mA/cm^2 .

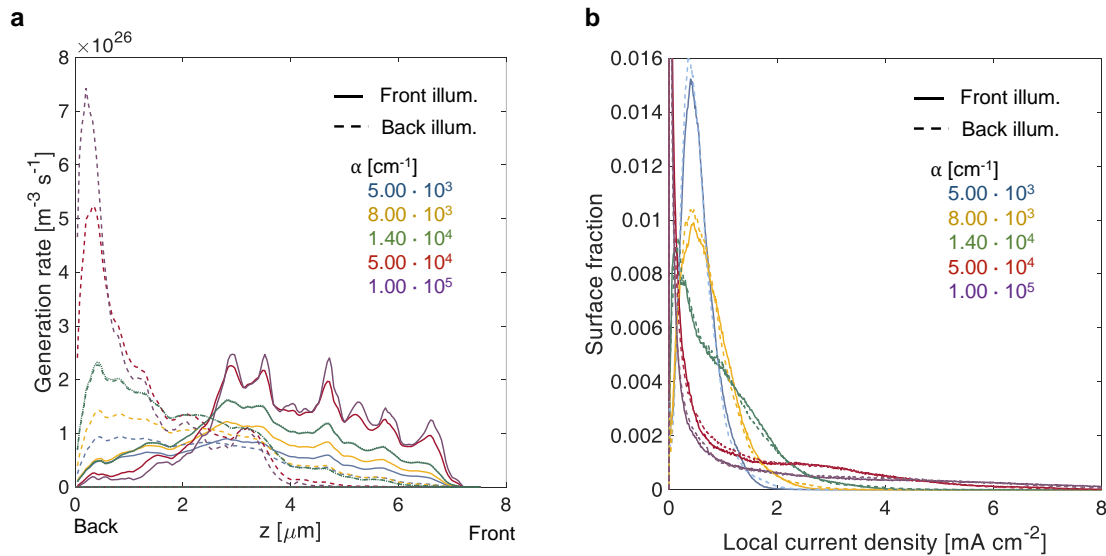


Figure 3.5 (a) Calculated generation rates for front and back illuminations integrated over all the discretized columns in x- and y-direction. The generation rates for the measured, wavelength-dependent absorption coefficient is shown in a green dotted line for front and back illumination. The mean deviation from the exact profile to a constant, wavelength-averaged absorption coefficient of $1.4 \cdot 10^4 \text{ cm}^{-1}$ is 1.1% and 1.6% for front and back illumination, respectively. The profiles for an additional 4 constant absorption coefficients are shown. (b) Local current density distribution for front and back illumination with constant, wavelength-dependent absorption coefficients.

3.4.2 Mass Transport and Local Species Concentrations

The diffusion of reactants into the pore space of the LTON photoelectrode was studied. The same subsample as previously discussed was considered and shown in Figure 3.2. The incident-light-to-charge-transfer-rate-conversion (ILCC) was calculated as a function of the intermediate reactant concentration, located above the LTON film at the interface to the macroscopic hydrodynamic boundary layer. The charge transfer rate integrated over the semiconductor-electrolyte interface is determined by the number of photons absorbed in the semiconductor and the number of reactants diffusing to the interface. The results are shown in Figure 3.6 as absorbed-light-to-charge-transfer-rate-conversion (ALCC) by multiplying with the absorptance. For $ALCC = 1$, the mass transport did not limit photoelectrode performance for a given c_i , but once the transport limitation was reached, the ALCC decreased sharply with decreasing c_i . For back illumination, the decrease occurred at higher c_i , and the initial slope was steeper because the electrolyte close to the back (where the current density is the highest) was depleted first. Similar curves with different starting points for the transport limits were calculated for various diffusion coefficients D , ranging from 10^{-4} to 10^{-6} cm²/s, including the diffusion coefficients of OH⁻ ($D=5.28 \cdot 10^{-5}$ cm²/s) and dissolved CO₂ ($D=2.02 \cdot 10^{-5}$ cm²/s) in water. The results can be approximated by the following correlation:

$$ALCC = a \cdot c_i \cdot e^{(-b \cdot c_i)} \leq 1 \quad (3.9)$$

where c_i [mol m⁻³] is the intermediate concentration. a and b are parameters that depend on the properties of the semiconductor, the electrolyte, the irradiance, and the morphology:

$$a = \Phi_{>Eg} \cdot A \cdot n \cdot D \cdot (a_1/\alpha^2 + a_2) \quad [\text{m}^3 \text{ mol}^{-1}] \quad (3.10)$$

$$b = \Phi_{>Eg} \cdot A \cdot n \cdot D \cdot (b_1/\alpha^2 + b_2) \quad [\text{m}^3 \text{ mol}^{-1}] \quad (3.11)$$

Both a and b are linearly dependent on the integral of the incoming photon flux (with energies above the bandgap), $\Phi_{>Eg}$ [m⁻² s⁻¹], the absorptance, A [-], the number of charges transferred at the semiconductor-electrolyte interface per reactant, n [-], and the diffusion coefficient of the reactant in the fluid phase, D [m²/s]. Finally, there is an inverse quadratic dependency of a and b on the absorption coefficient α [m⁻¹]. The first two parameters define the maximum possible

current per irradiated flat area, and the multiplication with n defines the maximum possible reactant flux through a plane perpendicular to the irradiation direction. Any increase in this overall flux shifts the curve of the ALCC to higher a_i , and a decrease shifts it to lower a_i . In Figure 3.6, the linear dependency between the diffusion coefficient and the parameters a and b has been demonstrated by fitting $a=a_0 \cdot D$ and $b=b_0 \cdot D$ in Equation (3.9) to all the simulated data points (same absorption coefficient), with a root mean square RMS=0.014 for front illumination and a RMS=0.016 for back illumination.

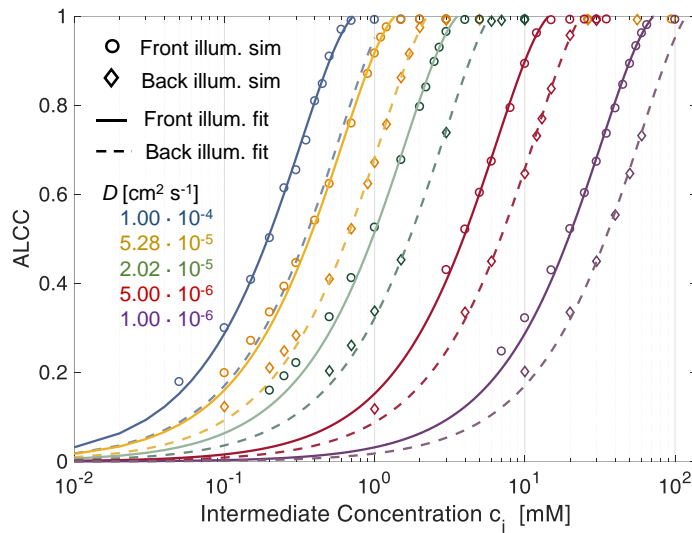


Figure 3.6 Simulated values for the absorbed-light-to-charge-transfer-conversion (ALCC) as a function of the intermediate concentration and the diffusion coefficient for front and back illumination. Two sets of parameters for front and back illumination could fit Equation (3.9) to the simulated values.

As shown in Figure 3.7, the ALCC highly depends on the generation rate profile, or more specifically, the absorption coefficient and the volume fraction profile. For front and back illumination, the results showed a shift to higher a_i for larger absorption coefficients. For the front illumination, this was mainly due to the increased generation rate. For the back illumination, the shift to higher a_i is much more pronounced, as a larger absorption coefficient also shifts the generated charges to lower positions in the film, thus making it more difficult for the reactants to reach. In both cases, the ALCC curves merged asymptotically with high absorption coefficients.

As previously discussed, in this range of high absorption coefficients, the generation rate profile is purely dependent on morphology. This behavior can be described by an inverse quadratic dependency with the fitting parameters a_1, a_2, b_1, b_2 . The parameters a_1 and b_1 are weights to control the decrease of a and b with increasing absorption coefficients. The parameters a_2 and b_2 characterize the effect of morphology on the ALCC. Equations (3.9) to (3.11) were fitted to the data points in Figure 3.7, respecting the previous fit for a_0 and b_0 . For front illumination, the parameters $a_1=2.254 \cdot 10^{-1}$, $a_2=4.714 \cdot 10^{-13}$, $b_1=8.217 \cdot 10^{-2}$, and $b_2=1.709 \cdot 10^{-13}$ were calculated with $\text{RMS}=0.032$. For back illumination, the parameters $a_1=2.538 \cdot 10^{-1}$, $a_2=2.003 \cdot 10^{-13}$, $b_1=9.536 \cdot 10^{-2}$, and $b_2=6.871 \cdot 10^{-14}$ were calculated with $\text{RMS}=0.041$. The parameters a_2 and b_2 are more than two times smaller for back illumination than for front illumination, which confirms them as morphology-descriptive parameters. Smaller parameters a_2 and b_2 lead to a shift of the ALCC to higher a . The morphology has a much stronger effect on the ALCC for the back illumination case, as the generation rates are much deeper in the film, and mass transport limitations occur at higher concentrations.

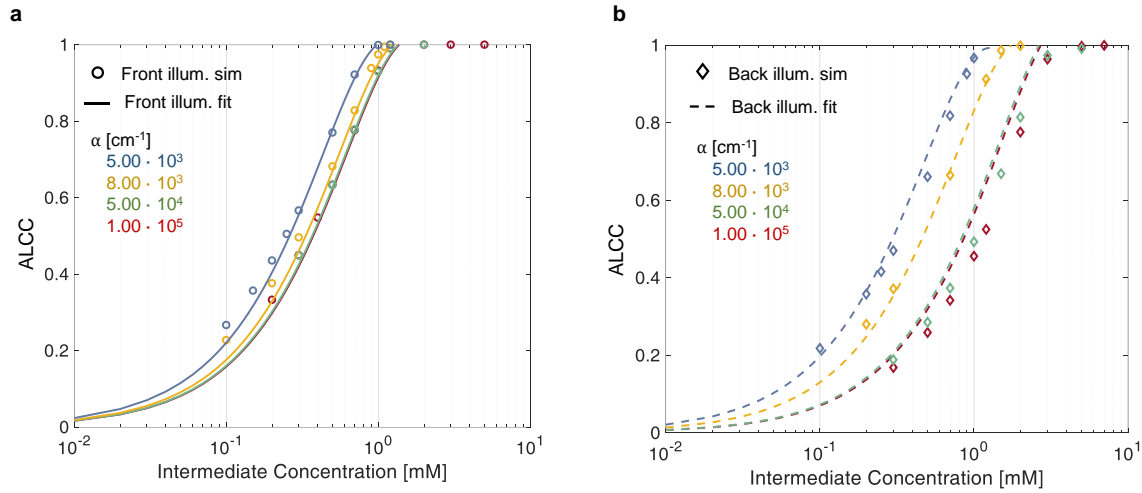


Figure 3.7 Simulation values and fit of ALCC vs. intermediate concentration for different, wavelength-averaged absorption coefficients: (a) front illumination and (b) back illumination. For increasing absorption coefficients, the curves merge asymptotically, as the generation rate profile, and therefore the ALCC, is only dependent on the morphology.

The correlation found between a and ALCC can be combined with a macroscopic Sherwood correlation, describing the hydrodynamic boundary layer, to link the ALCC to a bulk concentration, a_{bulk} . The LTON photoelectrode was considered to be in a PEC flow cell [28] to

Linking Morphology and Multi-Physical Transport in LTON Photoanodes

quantify the effect of a realistic hydrodynamic boundary layer. The transport of OH⁻ ions into the pore space of the LTON electrode for the oxygen evolution reaction in a water-splitting device was studied. For the specific case of a flow cell, the Sherwood correlation was used. However, Equation (3.9) can be linked to any other appropriate correlation in another reactor setup. The ALCC as a function of the bulk pH of an aqueous NaOH solution is shown in Figure 3.8a for 3 different flow regimes: almost stagnant ($Re=4$); medium velocity ($Re=143$); and maximum velocity in laminar flow ($Re=2300$). The bulk pH for which the mass transport through the macroscopic concentration boundary layer begins to be limiting is indicated with a dotted line. For $Re=4$, the macroscopic mass transport limit was predicted to begin below a bulk pH of 12.6. The mesoscopic LTON structure had a minimal effect in this flow regime, and the illumination direction did not play a role. For $Re=143$ and $Re=2300$, the mass transport limitation was due to LTON morphology, and the difference between front and back illumination was more pronounced for higher Re . For the given case, mass limitations occurred only for relatively low bulk pH values (bulk pH < 12.6, $Re=4$), and in a flow cell setup, those mass transport limitations were shown to be effectively reduced by increasing the velocity (bulk pH < 11.82, $Re=2300$). However, with our multi-scale correlation, we not only predict the bulk pH, below of which the mass transport is limiting, but we also describe the ALCC as a function of the bulk pH.

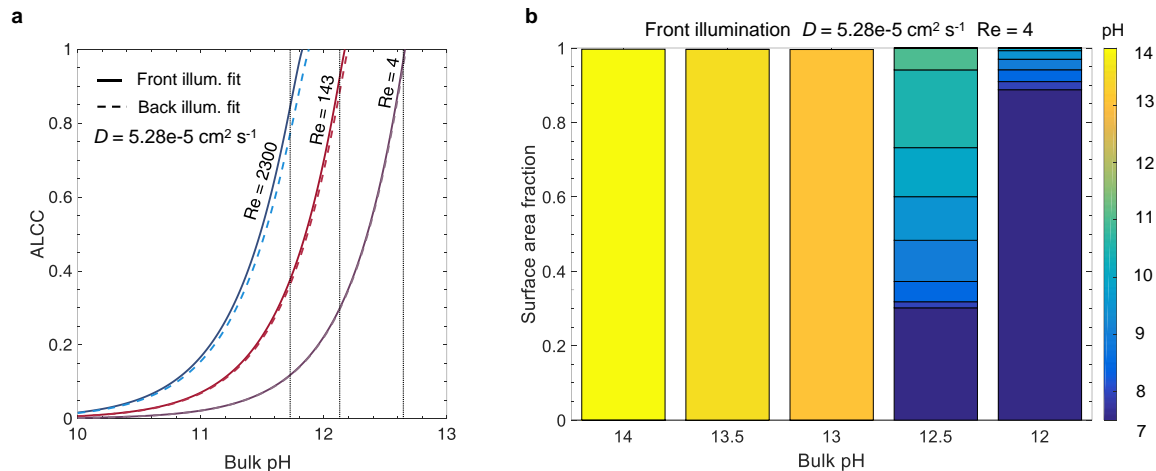


Figure 3.8 (a) The ALCC correlated to the bulk pH for different flow regimes of a flow cell water splitting device with NaOH as an electrolyte. The bulk pH, for which the mass transport through the macroscopic concentration boundary layer begins to be limiting, is indicated with a vertical dotted line. (b) The surface fraction of local surface concentrations for a given bulk pH and a flow regime of $Re=4$.

In addition, the local surface concentrations, c_s , along the semiconductor-electrolyte interface were quantified for different diffusion coefficients at specific ALCC values. Figure 3.9 shows the results for $D=5.28 \cdot 10^{-5} \text{ cm}^2/\text{s}$, $D=2.02 \cdot 10^{-5} \text{ cm}^2/\text{s}$, and $D=5.00 \cdot 10^{-6} \text{ cm}^2/\text{s}$ at ALCC=1, 0.8, 0.6, 0.4, and 0.2. The concentration distribution is analyzed by using histogram bins in the logarithmic scale. The surface fractions for surfaces with zero concentration are, by definition, identical for all three diffusion coefficients at a given ALCC. For decreasing ALCC values, the surface fraction of surfaces in depleted electrolyte regions increases. For both illumination directions, the depletion of the electrolyte began in regions above the FTO, which are the furthest from the bulk concentration. In the case of front illumination, a sharp increase of surfaces with zero concentration was observed from ALCC=1 to 0.6. The charges are generated high up in the film, and almost 60% of the surfaces were depleted for a 40% decrease of the overall mass flux. The rate of surface depletion diminished afterward for lower ALCC values. For back illumination, the surface fraction of depleted surfaces was always much lower compared to front illumination for the same ALCC. For back illumination, the peak of the generation rate was confined to the bottom of the LTON film, and the ALCC was influenced by the first surface areas that were depleted. Also, the surface fraction of depleted surfaces increased linearly with decreasing ALCC. In Figure 3.9, the order of magnitude of the intermediate concentration for each ALCC and diffusion coefficient is indicated above each histogram bar. For ALCC=1, the calculated surface concentrations were, at most, one order of magnitude smaller than the intermediate concentrations, resulting in small concentration gradients throughout the pore space of the structure. It quickly changed for ALCC=0.8, where a wide distribution of surface concentrations was observed. The magnitude of the diffusion coefficient determined the surface fraction at each concentration. Larger diffusion coefficients resulted in a broader concentration distribution along the film thickness, and low surface concentrations (10^{-3} - 10^{-1} mol/m^3) had a higher surface fraction. The concentration gradient was much higher for low diffusion coefficients, and most of the surface concentrations were closer to the intermediate concentration for a given ALCC. This was observed for front and back illumination.

In general, the computed results provide unique insights into the influence of morphology on local surface concentration distributions. The data can be used to study the degradation of structured semiconductor electrodes due to locally quantified pH values in which the semiconductor is not stable. The specific case of the LTON photoelectrode in aqueous NaOH electrolyte was analyzed, and the surface fractions of local pH values vs. bulk pH values are shown in Figure 3.8b. The ALCC was below 1 for bulk pH values smaller than 12.6 and $Re=4$. For higher bulk pH values, the local pH on the electrolyte-semiconductor interface was not affected

by the morphology. However, for smaller bulk pH values, e.g., 12.5, local pH values (down to pH 7) were found. For LTON, which is stable only at high pH values (above 13), we never reached a condition where the morphology would locally reduce the pH and degrade the semiconductor. The introduced approach could also be applied to an electrode for CO₂ reduction, where local pH gradients are also desired to promote the activity of a catalyst towards the production of a specific product.

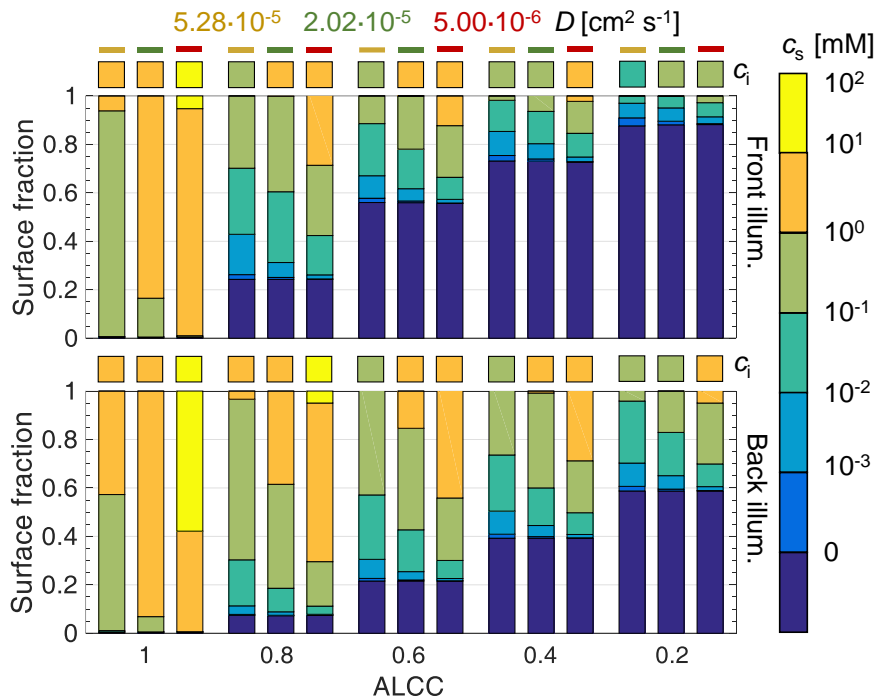


Figure 3.9 The surface concentration distributions, c_s , at the semiconductor-electrolyte interface at different ALCC values for 3 diffusion coefficients for front and back illumination. The histogram bars are binned with a logarithmic scale and the square above the bar indicates the intermediate concentration c_i corresponding to the ALCC.

3.4.3 Tortuosity

The tortuosity was calculated for the same conditions as the surface concentration calculations and is shown in Figure 3.10a. The tortuosity was defined as the mean path length of the reactants

traveling from the intermediate concentration plane to the semiconductor surface divided by the LTON film thickness. The path lengths were normally distributed, and the error bars indicate the standard deviations. The tortuosity was generally larger for back illumination, as the key parameter is the generation rate profile calculated from the light absorption. For both illumination directions, the tortuosity decreased for smaller ALCC values due to the creation and growth of the depletion regions. For a given ALCC value, the influence of the diffusion coefficient was negligible. Despite the complex structure of the LTON film, the mean values of the path lengths did not exceed the film thickness, even in the case of no mass transport limitations.

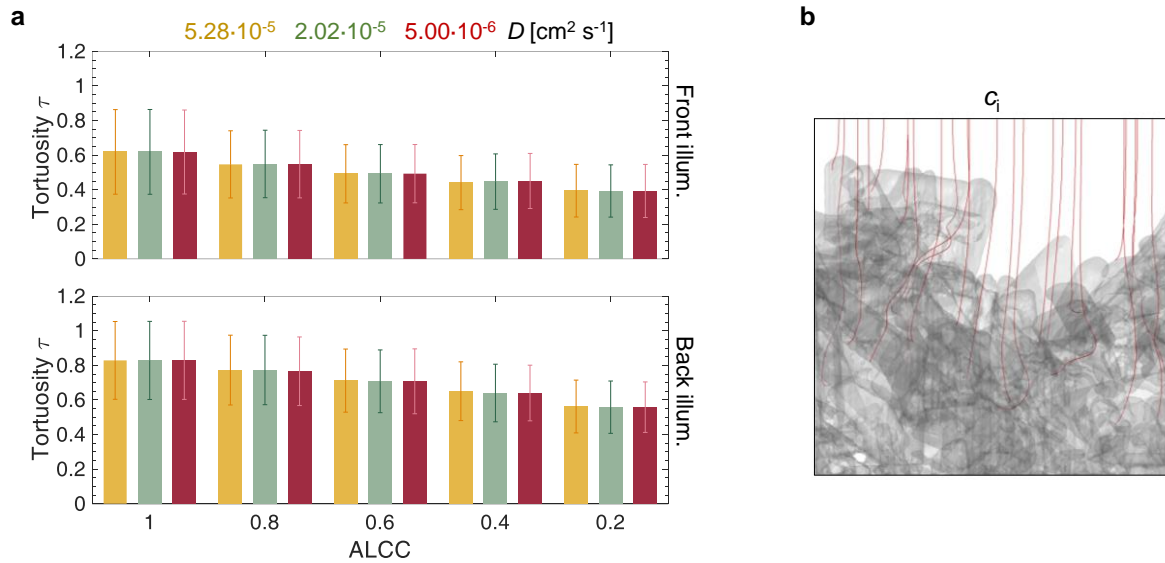


Figure 3.10 (a) The tortuosity, τ , at different ALCC values for 3 diffusion coefficients for front and back illumination. The tortuosity corresponds to the mean path length of the reactants divided by the film thickness. The error bars indicate the standard deviations of the normal distributed tortuosity. (b) Diffusion paths of the reactants in a side view of a 3D rendered LTON photoanode.

3.5 Conclusions

Multi-physical transport characterizations were performed on the LTON photoelectrode using direct pore-level simulations. The exact 3D morphological geometry was used to investigate light absorption in the semiconductor and mass transport through the liquid space of the LTON particle network. Current densities for front and back illumination were calculated and imposed as a boundary condition at the semiconductor-electrolyte interface. A light absorptance of 72.3% was calculated for an experimentally determined absorption coefficient. The area coverage of the FTO glass with LTON particles was found to be sufficient, as a maximum absorptance of 97.3% was reached when applying a two orders of magnitude larger absorption coefficient. Therefore, new experimental approaches are needed to stack the LTON particles more densely, or the film thickness has to be increased. Front side illumination resulted in more diluted and homogeneous light absorption and local current densities. On the other side, back illumination has the benefit of generating most of the electron-hole pairs very close to the FTO back contact, avoiding long transport paths through multiple particles for the electrons, and potentially reducing the recombination rate. However, the gain in efficiency can be reduced by limits in the ion transport through the mesoporous electrode. Therefore, mass transport calculations were done on multiple scales, simulating the purely diffusive transport of reactants through the stagnant pore space and correcting the result with a Sherwood correlation to take into account the concentration gradients in the macroscopic hydrodynamic boundary layer. The mass transport induced performance drop of the photoelectrode was described as a function of the semiconductor and electrolyte properties, and the incident radiation. Two sets of parameters were needed, one set for front and another for back illumination, to define a correlation that links the mass transport limitation to the morphology. The conditions, at which the performance of the electrode decreased, were quantified and correlated to a bulk electrolyte concentration, and flow conditions of a flow PEC setup. For slow flow rates, the mass transfer rate through the concentration boundary layer is smaller than the mass transfer rate through the mesoporous structure. For higher flow rates, diffusion limits between the LTON particles become dominant, and regions close to the FTO glass will be depleted of reactants. As expected, mass transport limitations occur at higher bulk concentrations for back illumination compared to front illumination. Local concentration distributions of OH^- ions on the semiconductor-electrolyte interface were quantified for various ALCC values and diffusion coefficients. These results give a unique insight into the local pH values within the mesoporous electrode. In the regime of limited mass transport, a substantial fraction of the semiconductor-electrolyte surface area is exposed to much more acidic pH values compared to the bulk electrolyte pH. For the same conditions, the tortuosity of the reactants

within the LTON film was calculated. For this specific case, the tortuosity was defined as the mean path length of the reactants divided by the LTON film thickness, allowing the tortuosity to be smaller than one. Despite the complexity of the morphology, the diffusion paths were short and even for back illumination, the tortuosity for most paths stayed below one.

We demonstrated a new approach for the characterization of multi-physical transport in morphologically complex photoelectrode. A better understanding of the light absorption and the ion transport limitations in these structures were obtained. The methods developed in this chapter can be applied to other morphologies and semiconductors to define design guidelines for performance-enhanced morphologies. A valuable extension to the presented approach would be the digital manipulation of the morphology with subsequent pore-level simulations. In combination with an optimization algorithm, the morphology with the best water-splitting performance could be computed.

3.6 References

- [1] S. Suter, M. Cantoni, Y. K. Gaudy, S. Pokrant, and S. Haussener, “Linking morphology and multi-physical transport in structured photoelectrodes,” *Sustain. Energy Fuels*, pp. 2661–2673, 2018.
- [2] J. Li and N. Wu, “Semiconductor-based photocatalysts and photoelectrochemical cells for solar fuel generation: a review,” *Catal. Sci. Technol.*, Sep. 2014.
- [3] D. Li, J. Shi, and C. Li, “Transition-Metal-Based Electrocatalysts as Cocatalysts for Photoelectrochemical Water Splitting: A Mini Review,” *Small*, vol. 14, no. 23, pp. 1–22, 2018.
- [4] H. R. Kim, G. Kim, S. Il In, and Y. Park, “Optimization of porous BiVO₄ photoanode from electrodeposited Bi electrode: Structural factors affecting photoelectrochemical performance,” *Electrochim. Acta*, vol. 189, pp. 252–258, 2016.
- [5] J. H. Kennedy, “Photooxidation of Water at α -Fe₂O₃ Electrodes,” *J. Electrochem. Soc.*, vol. 125, no. 5, p. 709, 1978.
- [6] O. K. Varghese, M. Paulose, and C. A. Grimes, “Long vertically aligned titania nanotubes on transparent conducting oxide for highly efficient solar cells,” *Nat. Nanotechnol.*, vol. 4, no. 9, pp. 592–7, 2009.
- [7] M. T. Mayer, C. Du, and D. Wang, “Hematite/Si nanowire dual-absorber system for photoelectrochemical water splitting at low applied potentials,” *J. Am. Chem. Soc.*, vol. 134, no. 30, pp. 12406–9, 2012.
- [8] Y. Qiu *et al.*, “Efficient photoelectrochemical water splitting with ultrathin films of hematite on three-dimensional nanophotonic structures,” *Nano Lett.*, vol. 14, no. 4, pp. 2123–9, Apr. 2014.
- [9] J. Joy, J. Mathew, and S. C. George, “Nanomaterials for photoelectrochemical water splitting – review,” *Int. J. Hydrogen Energy*, vol. 43, no. 10, pp. 4804–4817, 2018.
- [10] J. Li *et al.*, “Si nanopillar array optimization on Si thin films for solar energy harvesting,” *Appl. Phys. Lett.*, vol. 95, no. 3, p. 033102, Jul. 2009.
- [11] Z. Zhang and P. Wang, “Optimization of photoelectrochemical water splitting performance on hierarchical TiO₂ nanotube arrays,” *Energy Environ. Sci.*, vol. 5, no. 4, p. 6506, 2012.
- [12] A. Kay, I. Cesar, and M. Grätzel, “New benchmark for water photooxidation by nanostructured α -Fe₂O₃ films,” *J. Am. Chem. Soc.*, vol. 128, no. 49, pp. 15714–21, 2006.
- [13] S. Landsmann, A. E. Maegli, M. Trottmann, C. Battaglia, A. Weidenkaff, and S. Pokrant,

- “Design Guidelines for High-Performance Particle-Based Photoanodes for Water Splitting: Lanthanum Titanium Oxynitride as a Model,” *ChemSusChem*, vol. 8, no. 20, pp. 3451–3458, Oct. 2015.
- [14] S. Dilger, S. Landsmann, M. Trottmann, and S. Pokrant, “Carbon containing conductive networks in composite particle-based photoanodes for solar water splitting,” *J. Mater. Chem. A*, vol. 4, no. 43, pp. 17087–17095, 2016.
- [15] J. McKone and N. Lewis, “Photoelectrochemical water splitting: materials, processes and architectures,” H.-J. Lewerenz and L. Peter, Eds. Royal Society of Chemistry, 2013, pp. 52–82.
- [16] J. R. Wilson *et al.*, “Three-dimensional reconstruction of a solid-oxide fuel-cell anode,” *Nat. Mater.*, vol. 5, no. 7, pp. 541–544, 2006.
- [17] H. Ostadi, P. Rama, Y. Liu, R. Chen, X. X. Zhang, and K. Jiang, “3D reconstruction of a gas diffusion layer and a microporous layer,” *J. Memb. Sci.*, vol. 351, no. 1–2, pp. 69–74, 2010.
- [18] G. Brus, K. Miyawaki, H. Iwai, M. Saito, and H. Yoshida, “Tortuosity of an SOFC anode estimated from saturation currents and a mass transport model in comparison with a real micro-structure,” *Solid State Ionics*, vol. 265, pp. 13–21, 2014.
- [19] M. F. Lagadec, R. Zahn, S. Müller, and V. Wood, “Topological and network analysis of lithium ion battery components: The importance of pore space connectivity for cell operation,” *Energy Environ. Sci.*, vol. 11, no. 11, pp. 3194–3200, 2018.
- [20] S. Müller, J. Eller, M. Ebner, C. Burns, J. Dahn, and V. Wood, “Quantifying Inhomogeneity of Lithium Ion Battery Electrodes and Its Influence on Electrochemical Performance,” *J. Electrochem. Soc.*, vol. 165, no. 2, pp. A339–A344, 2018.
- [21] A. H. Wiedemann, G. M. Goldin, S. A. Barnett, H. Zhu, and R. J. Kee, “Effects of three-dimensional cathode microstructure on the performance of lithium-ion battery cathodes,” *Electrochim. Acta*, vol. 88, pp. 580–588, 2013.
- [22] J. R. Howell, *Thermal radiation heat transfer*, Sixth edit. Boca Raton: CRC Press, 2016.
- [23] Y. K. Gaudy, S. Dilger, S. Landsmann, U. Aschauer, S. Pokrant, and S. Haussener, “Determination and optimization of material parameters of particle-based LaTiO₂N photoelectrodes,” *J. Mater. Chem. A*, vol. 6, no. 36, pp. 17337–17352, 2018.
- [24] H. Friess, S. Haussener, A. Steinfeld, and J. Petrasch, “Tetrahedral mesh generation based on space indicator functions,” *Int. J. Numer. Methods Eng.*, vol. 93, no. 10, pp. 1040–1056, 2013.
- [25] “ANSYS® Academic Research CFX, Release 17.1.” .

- [26] Y. K. Gaudy and S. Haussener, “Utilizing modeling, experiments, and statistics for the analysis of water-splitting photoelectrodes,” *J. Mater. Chem. A*, vol. 4, no. 8, pp. 3100–3114, 2016.
- [27] J. Qi and R. F. Savinell, “Mass transfer in a laminar-flow parallel plate electrolytic cell with simultaneous development of velocity and concentration boundary layers,” *J. Appl. Electrochem.*, vol. 20, no. 6, pp. 885–892, 1990.
- [28] J. T. Davis and D. V Esposito, “Limiting photocurrent analysis of a wide channel photoelectrochemical flow reactor,” *J. Phys. D: Appl. Phys.*, vol. 50, no. 8, p. 084002, Mar. 2017.

Optimizing Reaction Selectivity by the Mesostructuring of Silver Catalysts

4.1 Introduction

The electrochemical reduction of CO₂ offers a path to store electricity from renewable sources in energy-dense chemical bonds [1]–[4]. During this process, carbon will be recycled by transforming available CO₂ into valuable chemicals and fuels and mitigate further greenhouse gas emissions [5]–[7]. Transition metals (e.g., Cu, Au, Ag) have been demonstrated to catalyze the multi-electron, electrochemical reduction of CO₂ for the production of carbon monoxide (CO), formic acid or formate (HCOOH or HCOO⁻), hydrocarbons and alcohols [6], [8]. However, low energy efficiencies and high costs have so far been the obstacles for novel CO₂-to-fuel conversion technologies [3]. In addition, the selectivity of the catalysts towards the products is often poor, which adds to the complexity of the system [9]. In most practical applications, the CO₂ is reduced in an aqueous environment, where the hydrogen evolution reaction rate often outcompetes the desired product evolution rate [4]. Unless the goal is to produce synthesis gas (a mixture of hydrogen and CO) [10], the key requirement for an efficient CO₂-to-fuel catalyst is to favor the activation of CO₂ to produce CO and keep the hydrogen evolution rate low. Even if CO is further reduced on a copper surface, the initial selectivity towards CO will determine the overall upper limit for the CO₂-to-fuel conversion [11]–[13]. Gold and silver electrodes, in particular, have shown to reduce CO₂ only to CO, but the selectivity for this reaction is low compared to the hydrogen evolution reaction [14]–[16]. The selectivity depends on the intrinsic property of the catalyst surface active site and the local concentration of the reaction partners, which are the

concentration of reactants and species involved in the rate-limiting steps of the reaction pathway [17]. The intrinsic properties are material specific, but research has demonstrated the impact of particle shape and size, and low-coordinated facets on the activity of the catalysts, allowing to tune the selectivity by nanostructuring [18]. The species concentration, on the other hand, can be influenced by the morphology on the mesoscale. An ordered mesostructure of gold inverse opals has proven to diminish the hydrogen evolution reaction by 10-fold compared to a planar electrode [19]. By electrodepositing gold in the void of a close-packed colloidal polystyrene thin films, the surface structure remained unchanged for porous electrodes of various thickness. Therefore, suppression of the hydrogen evolution reaction was attributed to the mass transport rather than the surface structure. Similar mesostructures made out of silver showed not only suppression of the hydrogen evolution reaction, but also promoted the CO evolution reaction, increasing the CO selectivity even further [17]. With the two competing surface reactions and multiple buffer reactions in the electrolyte, a mesostructure introduces complex diffusional gradients that could increase the overall selectivity rather than just be limiting, as it would be the case for a single product evolution reaction [19], [20]. The species concentration and the pH value in the mesostructure can be substantially different from the bulk electrolyte. Due to the production of hydroxide ions (OH⁻), the local pH near the catalyst surface is increased, which is thought to change the adsorption behavior of reaction intermediates that could pose a mass transport limit for the hydrogen evolution reaction [21]–[23]. Also, the local pH affects the equilibria of the acid-base reaction in the buffer solution, shifting towards carbonates and bicarbonates and reducing the local concentration of CO₂ [20], [24]. For a better understanding of the processes that lead to an enhance CO selectivity in mesostructures, it is important to know the species concentration distributions in porous catalysts. Experimentally, only the bulk concentrations and pH can easily be measured, but not the local values at the electrolyte-catalyst interface. Computational mass transport models can provide additional information on what is happening on the pore level. So far, many of the numerical studies have focused on the device level, modeling the mass transport on a macro scale between the cathode and anode [10], [25], [26]. Numerical models that focus on the pH and species distribution near the catalyst surface have been implemented in 1D for planar electrodes and show that higher buffer strength has a negative effect on the CO selectivity [20], [27]. Even though the bulk pH is higher than in a low buffer strength electrolyte, the local surface pH is reduced by the buffer reaction. In comparison with experimental data, a more sophisticated 1D model on a planar gold surface was used to determine the role of the bicarbonate in the rate-limiting step of CO₂ reduction catalysis [14]. Furthermore, Raciti et al [28]. recently applied a mass transport model to a nanostructured copper electrode. Their study highlighted the species

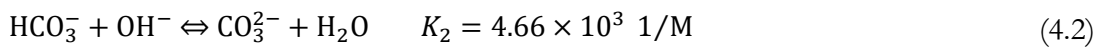
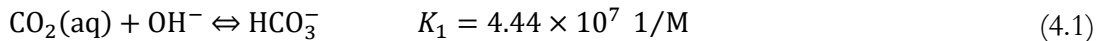
concentration and local pH values between the copper nanowires by using effective transport properties in a 1D approach.

Here we report a transport model on a detailed 3D mesostructure, taking into account the diffusion of species in the pore space, the buffer reactions in the electrolyte and surface reaction rates dependent on the local concentration of the reaction partners. The model was validated with experimental data from Yoon et al. [17]. The results of the study provide new insights into the local species concentration distributions and the local current distribution of the CO and H₂ evolution reactions. The model was then used to establish new design guidelines for ordered, mesostructured inverse opals catalysts to increase the CO faradaic efficiency in electrochemical CO₂ reduction.

4.2 Model Description and Governing Equations

We consider a mesoporous silver electrode for the electrochemical reduction of CO₂ in potassium bicarbonate (KHCO₃) electrolyte. Our model domain replicates an ordered Ag inverse opals (Ag-IO) electrode structure fabricated by Yoon et al [17]. They used colloidal polystyrene thin films as a template for the silver deposition. The polystyrene spheres were stacked in a hexagonal close-packed arrangement, leading to a face centered cubic (FCC) lattice of the pore network. The details of the fabrication process (sphere deposition, sintering, and silver electrodeposition) and experimental electrode characterization can be found in their publication [17]. The thickness of the Ag-IO films can be precisely controlled, and the uniform porosity, surface structure, and tortuosity make them suitable for the experimental validation of our model. The model domain of the porous Ag-IO network with pores of about 200 nm in diameter is shown in Figure 4.1. 12 channels interconnect each pore, with channel diameters, extracted from SEM images, of around 70 nm. The desired morphology was achieved by overlapping the spheres of a hexagonal close-packed bed. The starting radius of the spheres was $r_{\text{sphere}} = r_{\text{pore}} - dr$, and the sphere radii were subsequently increased by $dr = 7$ nm. The domain symmetries are along the hexagonal prism walls. The key morphology parameters of the Ag-IO films are the film thickness, t , the pore diameter d_{pore} , and the surface roughness factor, RF, defined as the electrochemical active surface area (ECSA) normalized to the geometric area of the electrode. In the model, ECSA is the surface area of the Ag-electrolyte interface and the geometric area is the hexagonal cross-section of the symmetry unit cell. The film thickness is a function of the number of pores and the pore radius and is shown at end of this section. An electrolyte bulk concentration of 0.1 M KHCO₃ is considered with a boundary layer thickness of 1 μm. This boundary layer thickness has been reported to correspond to a stirring rate of approximately 700-800 rpm [14]. In the concentration boundary layer, the convection and velocity gradients are assumed to be insignificant.

The buffer reactions in the CO₂ and bicarbonate system in alkaline solution are:



with reaction rate constants shown in Table 4.1. The bulk electrolyte is saturated with CO₂, and the bulk species concentrations are given in Table 4.2. The diffusion coefficients of the various species in water are listed in Table 4.3.

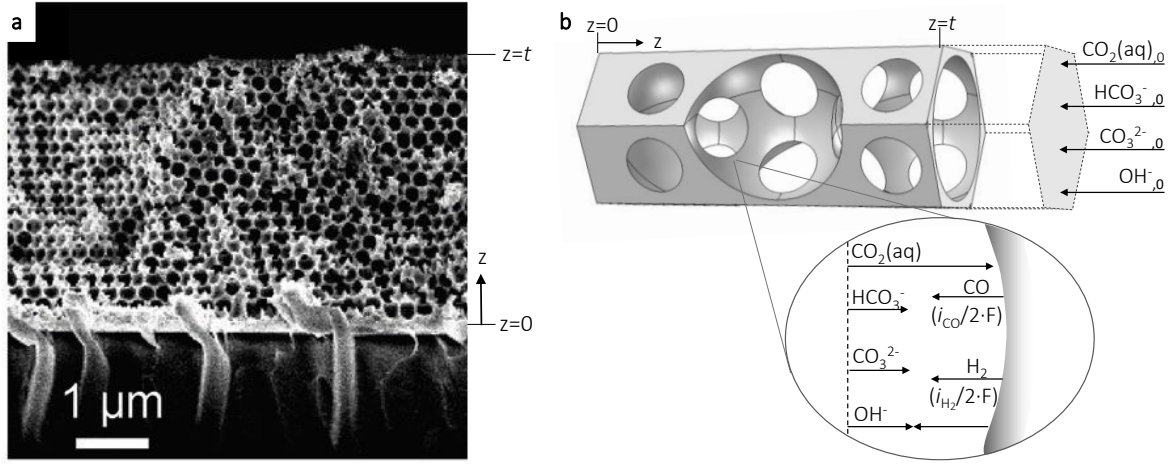


Figure 4.1 (a) SEM cross-section of Ag-IO reprinted with permission from reference [17]. (b) Illustration of the mass transport model for electrochemical reduction of CO₂ on Ag-IO.

Table 4.1 Rate constants for reactions (4.1) and (4.2) at 25°C [20], [32].

Reaction	Forward rate constant	Reverse rate constant
1	$k_{1f} = 5.93 \times 10^3 \text{ M}^{-1}\text{s}^{-1}$	$k_{1r} = 1.34 \times 10^{-4} \text{ s}^{-1}$
2	$k_{2f} = 1 \times 10^8 \text{ M}^{-1}\text{s}^{-1}$	$k_{2r} = 2.15 \times 10^4 \text{ s}^{-1}$

Table 4.2 Species bulk concentrations in 0.1 M KHCO₃ at 25°C [14].

CO ₂ (aq)	HCO ₃ ⁻	CO ₃ ²⁻	OH ⁻
0.033 M	0.1 M	$2.9 \times 10^{-5} \text{ M}$	$6.6 \times 10^{-8} \text{ M}$

Table 4.3 Diffusion coefficients of species in water at 25°C. The values have been corrected with the Stokes-Einstein equation [4].

$D_{\text{CO}_2} [\text{m}^2\text{s}^{-1}]$	$D_{\text{HCO}_3^-} [\text{m}^2\text{s}^{-1}]$	$D_{\text{CO}_3^{2-}} [\text{m}^2\text{s}^{-1}]$	$D_{\text{OH}^-} [\text{m}^2\text{s}^{-1}]$
1.48×10^{-9}	9.25×10^{-10}	7.12×10^{-10}	5.27×10^{-9}

Optimizing Reaction Selectivity by the Mesostructuring of Silver Catalysts

The following partial differential equations in steady state conditions describe the mass balances of the species in the boundary layer and the pore space:

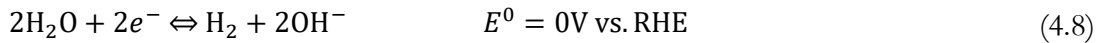
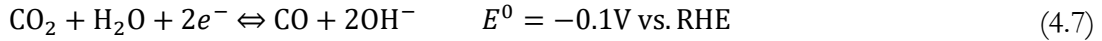
$$0 = D_{\text{CO}_2} \nabla^2 [\text{CO}_2(\text{aq})] - [\text{CO}_2(\text{aq})][\text{OH}^-]k_{1f} + [\text{HCO}_3^-]k_{1r} \quad (4.3)$$

$$0 = D_{\text{HCO}_3^-} \nabla^2 [\text{HCO}_3^-] + [\text{CO}_2(\text{aq})][\text{OH}^-]k_{1f} - [\text{HCO}_3^-]k_{1r} - [\text{HCO}_3^-][\text{OH}^-]k_{2f} + [\text{CO}_3^{2-}]k_{2r} \quad (4.4)$$

$$0 = D_{\text{CO}_3^{2-}} \nabla^2 [\text{CO}_3^{2-}] + [\text{HCO}_3^-][\text{OH}^-]k_{2f} - [\text{CO}_3^{2-}]k_{2r} \quad (4.5)$$

$$0 = D_{\text{OH}^-} \nabla^2 [\text{OH}^-] - [\text{CO}_2(\text{aq})][\text{OH}^-]k_{1f} + [\text{HCO}_3^-]k_{1r} - [\text{HCO}_3^-][\text{OH}^-]k_{2f} + [\text{CO}_3^{2-}]k_{2r} \quad (4.6)$$

At the silver electrode surface the two competing reduction reactions are:



Above, the equilibrium potentials are given versus the reversible hydrogen electrode (RHE). The molar flux of the produced species was calculated from the current densities using Faraday's law. The surface reactions were modeled by the concentration dependent Butler-Volmer correlations:

$$i_{\text{CO}} = i_{0,\text{CO}} \left(\frac{c_{\text{CO}_3^{2-}}}{c_{\text{CO}_3^{2-},0}} \right)^m \left(\frac{c_{\text{OH}^-}}{c_{\text{OH}^-,0}} \exp\left(\frac{(2 - \beta_{\text{CO}})F\eta}{RT}\right) - \frac{c_{\text{CO}_2}}{c_{\text{CO}_2,0}} \exp\left(\frac{-\beta_{\text{CO}}F\eta}{RT}\right) \right) \quad (4.9)$$

$$i_{\text{H}_2} = i_{0,\text{H}_2} \left(\frac{c_{\text{OH}^-,0}}{c_{\text{OH}^-}} \right)^n \left(\frac{c_{\text{OH}^-}}{c_{\text{OH}^-,0}} \exp\left(\frac{(2 - \beta_{\text{H}_2})F\eta}{RT}\right) - \exp\left(\frac{-\beta_{\text{H}_2}F\eta}{RT}\right) \right) \quad (4.10)$$

with exchange current densities, i_0 , charge transfer coefficients, β , fitted to experimental data. The anodic back reactions were included in the model, but their contributions are small at the overpotentials relevant for CO_2 reduction compared to the cathodic reactions. The mass transport limitations, especially for $\text{CO}_2(\text{aq})$, were taken into account with the concentration dependent terms in front of the exponential functions. The water reduction reaction rate has been shown to be intrinsically pH dependent on Ag and Au electrodes [17], [19]. The suppression of

the H₂ evolution at higher pH values was modeled with an inverse dependency of the exchange current density on the OH⁻ concentration. The promotion of CO evolution for mesoporous Ag electrodes has been hypothesized to be related to increased activity of CO₃²⁻ [17], [29]. Our calculation showed (see discussion in section 4.3.2) that besides the increase in OH⁻ concentration, the activity of CO₃²⁻ is the only activity with a substantial change from the bulk concentration in a mesoporous structure. The parameters *m* and *n* were fitted to experimental data. The experimental voltage sweeps of Yoon et al. [17] show a limiting current densities for both of the reduction reactions. For the H₂ evolution, the current density reaches a plateau at -0.75V vs. RHE for a flat Ag electrode. The CO evolution for a mesoporous Ag electrode with a roughness factor of more than 100 shows a linear increase for higher potentials, indicating a limit in mass transport. Both cases were assumed to be caused by adsorption of inhibiting species on the Ag surface and were modeled with an absolute maximum current density:

$$i = \frac{i_w}{1 + \left\| \frac{i_w}{i_{lim}} \right\|} \quad (4.11)$$

where *i_w* is the current density without considering the specific mass transport limitations through adsorption, and *i_{lim}* is the limiting current density that correlates to the maximum reaction rate observed in the experiment.

The set of differential (4.3)-(4.6) and algebraic equations (4.7)-(4.11) was solved on a 3D tetrahedral mesh using a finite element solver in COMSOL 5.3.

Film Thickness vs. Roughness Factor

The film thickness is analytically linked to the number of pores and the sphere radius of the template spheres. Assuming a sintering process, where the sphere overlap is proportional to the sphere radius, the film thickness is determined by the following equations:

$$r_{\text{sphere}} = r_{\text{pore}} - dr \quad (4.12)$$

$$dr = 0.07 \cdot r_{\text{pore}} \quad (4.13)$$

$$t = r_{\text{sphere}} + (n_{\text{pores}} - 1) \cdot (2 \cdot \sqrt{6}/3 \cdot r_{\text{sphere}}) \quad (4.14)$$

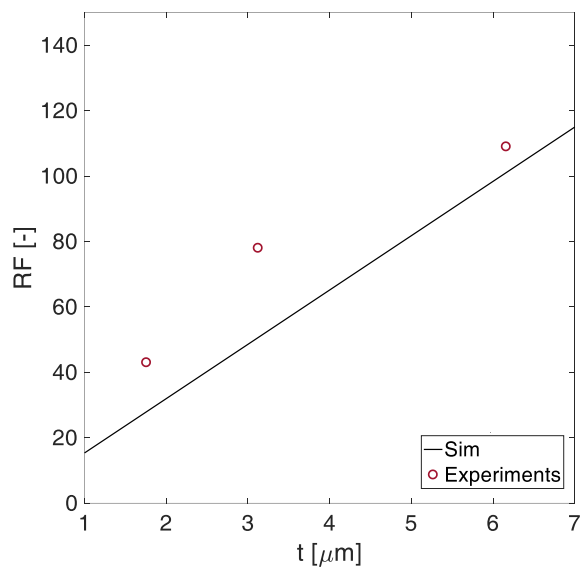


Figure 4.2 Roughness factor as a function of the Ag-IO film thickness. The experimental data were taken from Yoon et al.[17]. The roughness factor of the model is a linear function. The model values are in general smaller than the experimentally determined values. Most probably, there is a micro roughness on the pore level that is not considered in the model.

4.3 Results and Discussion

4.3.1 Empirical Parameters and Model Validation

The exchange current densities, i_0 , and the charge transfer coefficients, β , for the CO₂ and water reduction reactions at the Ag surface were determined by fitting a 1D model to the experimental data of a planar silver electrode in 0.1 M KHCO₃ [17]. The best fitting parameters were found by minimizing the sum of square errors (SSE) between the model and the experimental data for a roughness factor (RF) equal to 4. RF=4 corresponds to a planar electrode and the results are listed in Table 4.4 and shown in Figure 4.3. The model was fitted to the average of 3 planar electrodes. The reduction rate dependencies on the OH⁻ and CO₃⁻ activities were initially kept first order. 3 Ag-IO with RF=43, 78, 109 were digitally replicated to validate the mesoporous model by comparing the simulation results to the experimental values from Yoon et al. [17]. The roughness factor versus film thickness is shown in Figure 4.2 for the experimental and model structures. With a pore diameter of 200 nm and channel diameters of 70 nm, the model geometries exhibit smaller RF for the same film thickness. Besides measurement errors, the differences could be caused by a micro roughness at the pore scale of the Ag-IO. As the surface area has a dominant effect on the OH⁻ production and CO₂ consumption, the exchange current densities $i_{0,CO}$ and i_{0,H_2} were multiplied by a correction factor to compensate for the smaller surface area. For both reduction reactions, a limiting current density was observed in the experimental data. The water reduction reaches a plateau for a planar electrode at around -0.75 V vs. RHE, whereas the CO₂ reduction exhibits a linear instead of an exponential increase for RF>43 between -0.7 and -0.75 V vs. RHE. The observed mass limiting phenomena could most likely be the adsorption of reaction inhibiting species at the electrolyte-electrode interface limiting higher current densities. For both reactions, a limiting current density was extracted from the experimental data and the values added to the model are shown in Table 4.4. The dashed lines in Figure 4.3 show the simulation results for $m=n=1$. The general trend of H₂ evolution suppression and CO evolution promotion for higher RF can be observed. However, the model is less sensitive to the mesoporous structure; hence, for an Ag-IO with RF=109 at a potential of -0.7 V vs. RHE, the partial CO current density is 1.6 times smaller and, the partial H₂ current density is 2.5 times larger than the experimental values. This is also reflected in the faradaic efficiency for the CO production shown in Figure 4.4, where at the same potential the selectivity towards CO production is 1.7 times smaller than measured experimentally. However, the model can predict the experimentally observed shift to lower potentials for the peak in CO faradaic efficiency, when the roughness of the Ag-IO is increased.

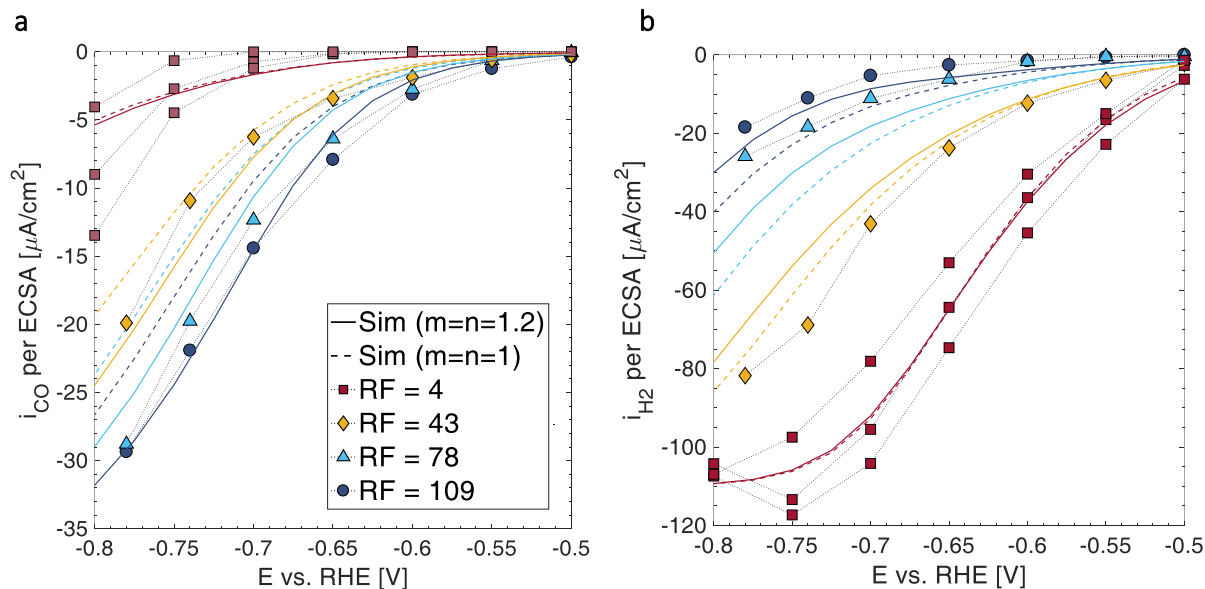


Figure 4.3 Partial current density for the CO_2 and water reduction reaction, normalized by the electrochemical active surface area (ECSA). The experimental data from Yoon et al.[17] is shown with markers. The computed results are shown with a dashed ($m=n=1$) and a solid line ($m=n=1.2$). The lines and markers are color coded based on their roughness factor RF.

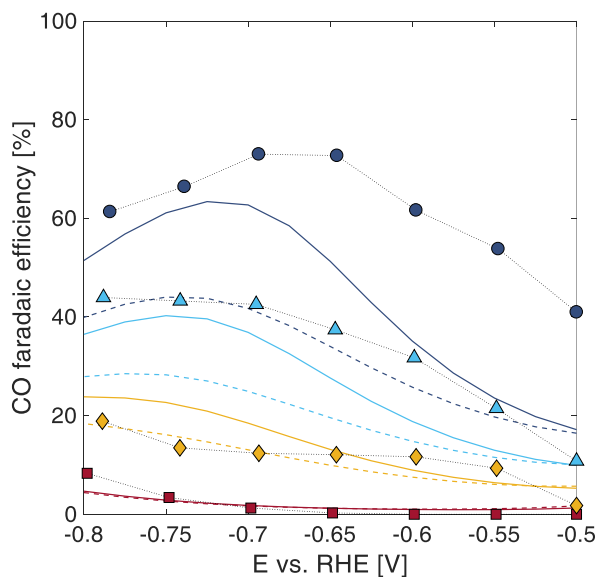


Figure 4.4 CO faradaic efficiency on Ag films, with differing RF, as a function of applied potential. The legend and color code is the same as in Figure 4.3.

Table 4.4 Empirical parameters fitted to the experimental data of a planar Ag electrode.

parameter set	$i_{0,\text{CO}}$ [A m ⁻²]	i_{0,H_2} [A m ⁻²]	$i_{\text{lim,CO}}$ [A m ⁻²]	$i_{\text{lim,H}_2}$ [A m ⁻²]
1	1.0012×10^{-5}	7.0102×10^{-10}	0.4	1.1
2	8.4083×10^{-6}	9.2084×10^{-10}	0.4	1.1
parameter set	β_{CO} [-]	β_{H_2} [-]	m [-]	n [-]
1	0.29	0.95	1	1
2	0.29	0.95	1.2	1.2

In order to increase the sensitivity of the model towards the mesoporous structure, the reduction rate dependencies on the OH⁻ and CO₃⁻ activities were allowed to be greater than 1 and fractional. By keeping the same fitting algorithm, the exchange current densities and charge transfer coefficients were determined on the planar 1D simulation for given values of m and n . The mesoporous model was then validated and the SSE between the model and the experimental data were assessed. The best fitting values for m and n were found by minimizing the SSE. The parameters are listed in Table 4.4, and the partial current densities are shown with a solid line in Figure 4.3. For an Ag-IO with RF=109 at a potential of -0.7 V vs. RHE, the model partial CO current density matches the experimental value, and the partial H₂ current density is 1.6 times larger than measured. The model, with $m=1.2$ and $n=1.2$, predicts a maximum faradaic efficiency in CO production of 63% at -0.725 V vs. RHE, 10 percent points less than measured with a shift in potential of -0.025 V.

A sensitivity study was done by independently varying the pore and channel diameter by $\pm 10\%$ (Figure 4.5). Both parameters mainly alter the suppression of the water reduction reaction. Reducing the pore diameter decreases the CO selectivity, whereas a reduction in the channel diameter enhances the CO selectivity. In this study, the number of pores were kept constant, but the film thickness changes, leading to a smaller overall surface area for a reduced pore diameter, and a larger surface area for a structure with smaller channel diameters. For both cases, the deviation in the maximum CO faradaic efficiencies was smaller than 7 percent points.

The parameter set 2 (Table 4.4) was used in the mesoporous model for the subsequent sections.

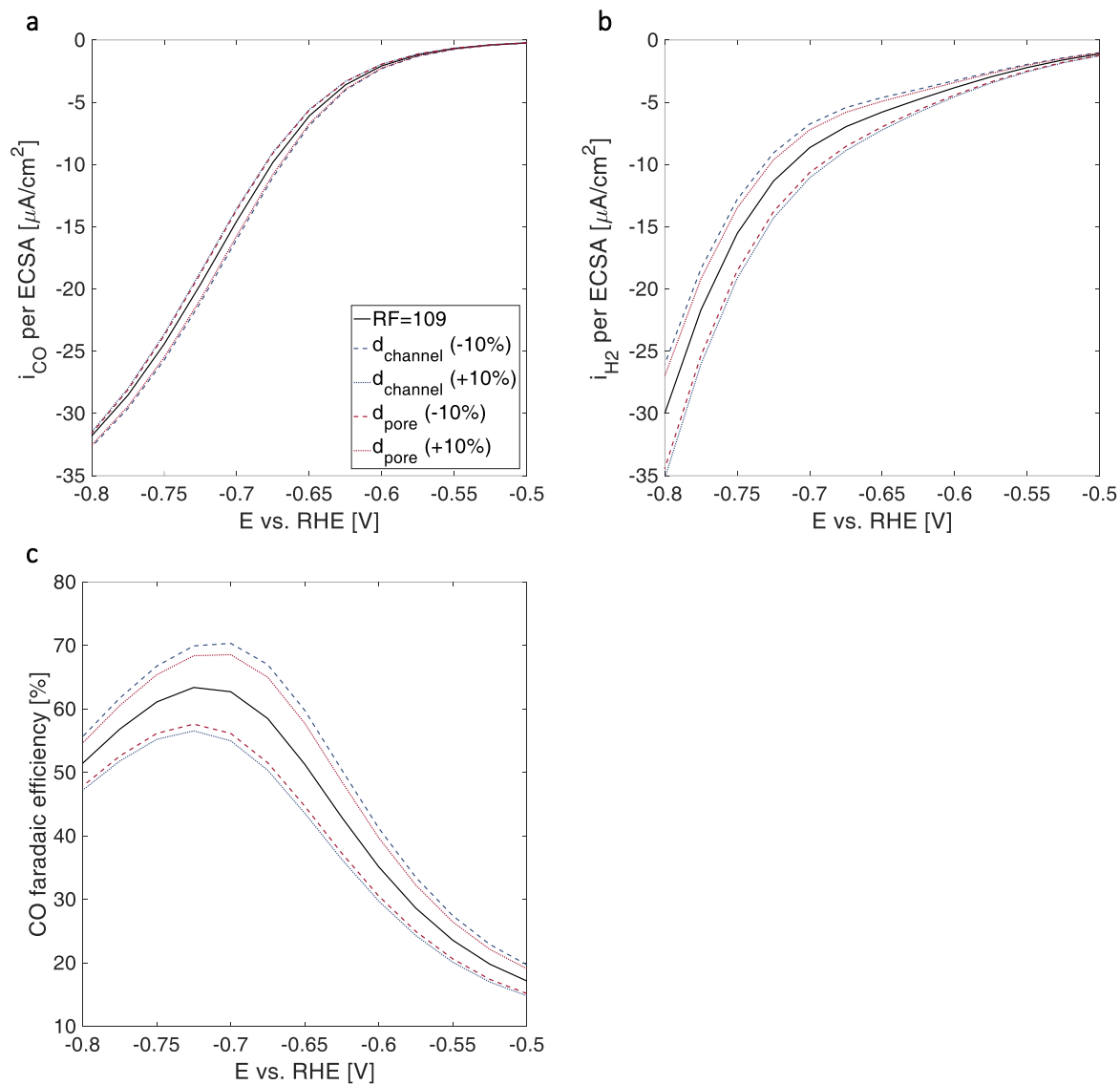


Figure 4.5 A sensitivity study for the model with a RF=109. The partial current densities and the CO faradaic efficiency are shown for $\pm 10\%$ in pore and channel diameter. The water reduction is more sensitive to the changes in morphology than the CO₂ reduction. Reducing the pore diameter decreases the CO faradaic selectivity, whereas a reduction in the channel diameter enhances the selectivity.

4.3.2 Local Current Densities and Species Concentrations

The validated 3D model of the replicated mesoporous Ag-IO offers unique insights into the local current density distributions of the CO₂ and water reduction reactions and the local concentrations of the species CO₂, OH⁻, HCO₃⁻, and CO₃²⁻ in the pore space. Overall, the partial CO current per ECSA is promoted for Ag-IO with higher roughness factors, and the partial H₂ current is suppressed. However, the local current densities are not homogeneously distributed along the z-axis as shown in Figure 4.6a for a potential of -0.8 V vs. RHE.

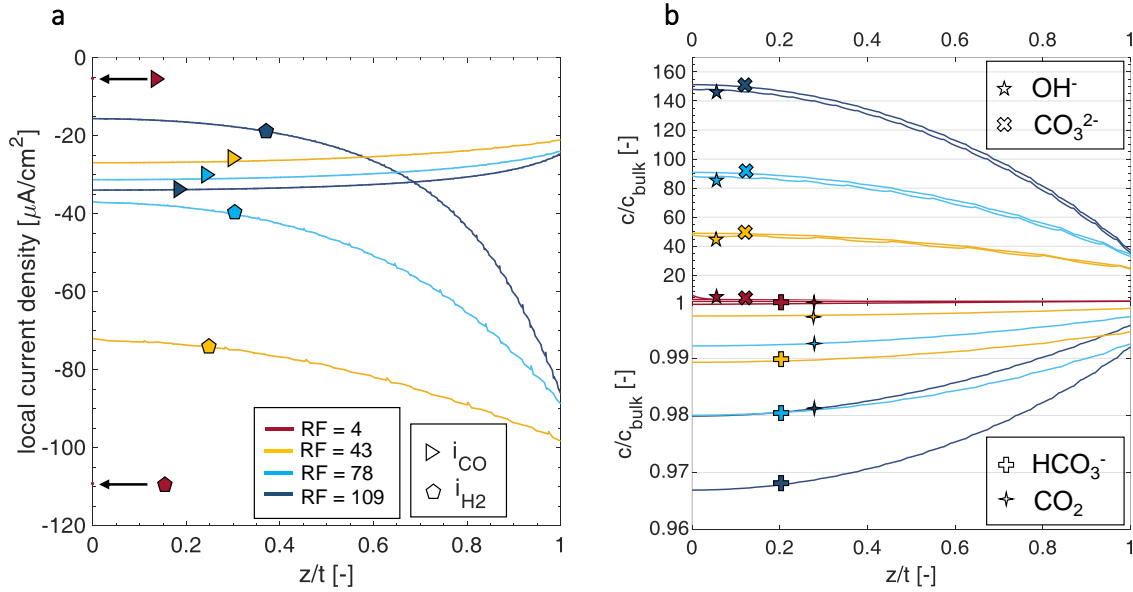


Figure 4.6 (a) Local current density profiles of CO and H₂ evolution along the z -axis of Ag-IO electrodes with RF=4, 43, 78, 109 and thickness $t=0$ (planar), 1.7, 3.1, 6.2 μm . (b) Concentration profiles along the z -axis of OH⁻, CO₃²⁻, HCO₃⁻ and CO₂ versus their bulk concentration. Both Figures are at a potential of -0.8 V vs. RHE.

The biggest suppression of H₂ evolution occurs in the lowest 20% of the pore network, whereas in the more shallow pores, near $z=t$, the H₂ partial current density increases sharply to values close to the planar case. The promotion for the CO evolution is also more pronounced near the bottom of the electrode, with a small decrease in CO partial current density towards the top of the film. These observations are consistent with the calculated species concentrations shown in

Figure 4.6b. The rate of OH^- production in the deepest pores is substantially higher than the diffusion flux towards the bulk electrolyte. This leads to a build-up of OH^- and, through the buffer reaction of the electrolyte, also increases the CO_3^{2-} concentration. For pores closer to the top of the film, the mass transport towards the bulk electrolyte is faster, leading to lower OH^- and CO_3^{2-} concentrations. The calculations show that the top 40% of the Ag-IO films substantially reduce the selectivity towards the CO evolution and that higher CO faradaic efficiencies could be achieved by decreasing the mass transfer in this part of the film.

Figure 4.7 proves that there are no concentration gradients perpendicular to the z -axis for CO_2 , HCO_3^- , and CO_3^{2-} and only a small gradient for OH^- . Also, the OH^- concentration is the only concentration profile that is not monotonically increasing or decreasing along the z -axis in the pore space. On the top section of each pore, the OH^- concentration increases slightly due to the longer diffusion path through one of the 3 channels that are not on the top of the pore space. This explains the wavy OH^- concentration profile in Figure 4.6b.

For the considered operation conditions, the consumption of CO_2 is low and with a maximum decrease of 2% from the saturation concentration (RF=109) far away from mass transport limitations. Also the depletion of HCO_3^- is small and has been shown not to take part in any rate-limiting step [14].

4.3.3 Pore Size vs. Film Thickness

The film thickness, t , and the pore size, d_{pore} , determine the morphology of inverse opal mesoporous structures. When using a self-assembling sphere packing for the template, the pore network is defined by an FCC lattice in a hexagonal close-packed arrangement [30]. A micro roughness factor of 1 was assumed on the pore level and the dependency of RF vs. t was linear (Figure 4.2). The sphere overlap, dr , from the sintering process, was assumed to be proportional to the pore radius. The relation $dr=0.07 \cdot r_{\text{pore}}$ was extracted from SEM images of the Ag-IO [17]. Therefore, the surface area, the roughness factor and, the tortuosity are geometrically linked to t and d_{pore} .

Increasing the film thickness increases the diffusion path lengths of the species and more OH^- and CO_3^{2-} can accumulate in the pore network. As previously seen, this leads to a higher partial CO current densities and a higher CO faradaic selectivity. Figure 4.8a shows the partial CO current density for Ag-IO of thickness 3 and 15 μm , and Figure 4.8b shows the CO faradaic selectivity for Ag-IO of thickness 3, 6 and 15 μm . In contrary, increasing the pore size for a

constant film thickness decreases both current density and selectivity. Having bigger pores in the same film thickness translates to a smaller surface area, and therefore, a lower rate of OH⁻ production which favors the water reduction reaction. For the considered pore diameters of 100-400 nm, the change in tortuosity is negligible as shown in Figure 4.9. With the thickness of the film much bigger than the pore diameter, mass transport lateral to the film thickness is insignificant.

Figure 4.8c and Figure 4.8d quantify the effect of the film thickness and the pore diameter on the maximal achievable CO faradaic efficiency and the required electrode potential. The linear dependency of RF vs. t and the non-linear dependency of RF vs. d_{pore} is shown. For a pore diameter of 200 nm, a film thickness of more than 10 μm is needed to push the CO faradaic efficiency above 90%. The same faradaic efficiency can be achieved with a pore diameter of 100 nm at a reduced film thickness of 7 μm . With the porosity independent of the pore size at a value of 0.87, 30% of Ag could be saved by halving the pore size. From this point of view, reducing the pore size is the superior path to boost the selectivity towards CO₂ reduction. However, in reality, the optimum for such an electrode will also be dependent on the homogeneity of the mesoporous film. Whether thin films with small pore diameters or thicker films with big pore diameters can be fabricated with a higher homogeneity and reproducibility needs to be experimentally investigated.

What we can note here, is that the thin film mentioned above consists of 93 pores, whereas the thicker film only has 67 pores. In summary, for IO films, it is not enough to characterize the film by its roughness factor, but the film thickness and pore diameter are the key parameters to optimize the geometry.

In general, the peak of the maximum CO faradaic efficiency is observed at lower potentials vs. RHE when increasing the film thickness or reducing the pore diameter. The potential is linked to the value of the maximum CO faradaic efficiency, and not directly dependent on the film thickness and pore diameter. Both film mentioned above ($t=10\mu\text{m}$, $d_{\text{pore}}=200$ nm and $t=7\mu\text{m}$, $d_{\text{pore}}=100$ nm) have a maximum CO faradaic efficiency of 90% at the same potential of -0.675 V vs. RHE. Using a mesoporous Ag-IO not only enhances substantially the CO faradaic efficiency, but also decreases the required potentials vs. RHE.

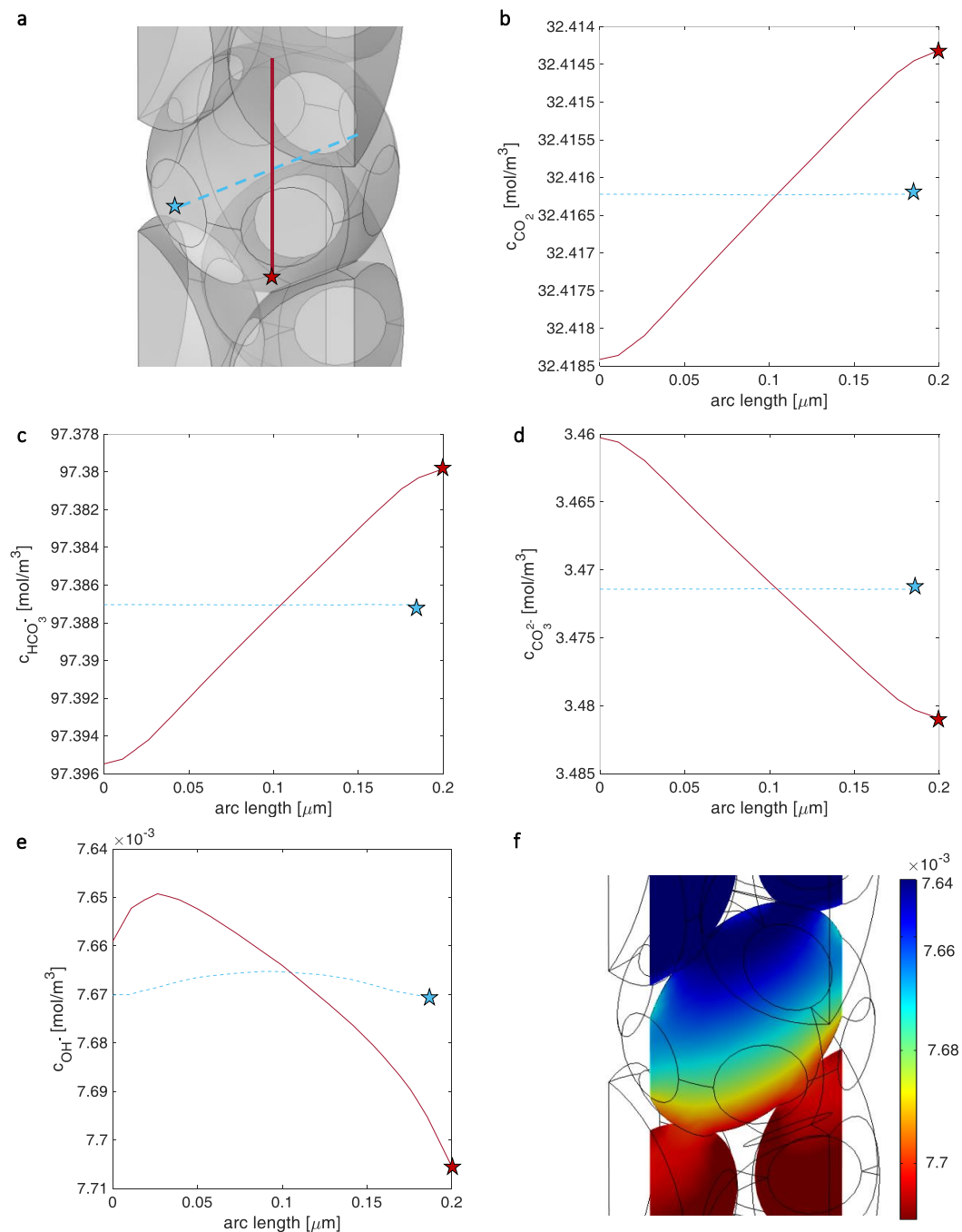


Figure 4.7 (a) Illustration of the horizontal and vertical cut line through the space of a pore at $\xi=1 \mu\text{m}$ for an Ag-IO with RF=109 at -0.8 V vs. RHE. (b)-(e) Concentration profiles of CO_2 ,

HCO_3^- , CO_3^{2-} and OH^- along the cut lines, with the star indicating the end position. (f) Contour plot of the OH^- concentration on the x-y cut plane.

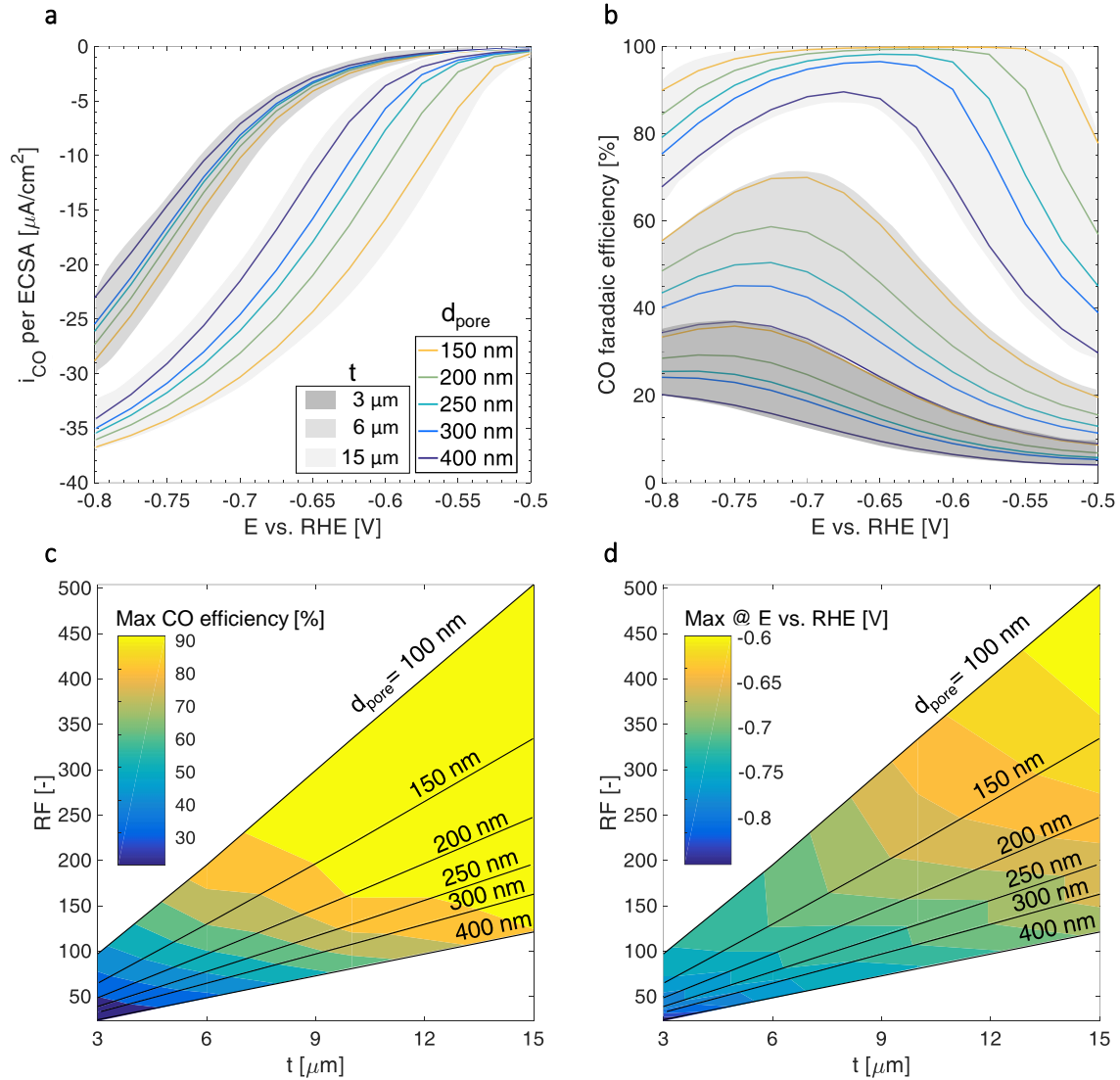


Figure 4.8 (a) Partial CO current density for Ag-IO with pore diameters of 150-400 nm and film thickness of 3 and 15 μm . (b) CO faradaic efficiency for electrodes with the same pore diameters and film thickness of 3, 6 and 15 μm . (c) The values of the maximum CO faradaic efficiency in the contour plot as a function of the film thickness t and the roughness factor RF. Also, the linear relation between RF and t is shown for the different pore diameters. (d) The potentials vs. RHE for the maximum CO faradaic efficiency as a function of the film thickness t and the roughness factor RF.

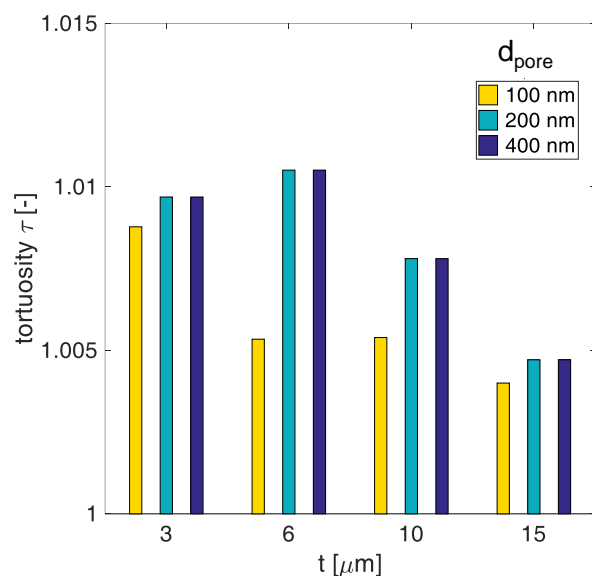


Figure 4.9 The tortuosity is defined as the diffusion path length through the entire Ag-IO film divided by the thickness t . Results for a film thickness of 3, 6, 10, and 15 μm are shown for films with pore diameters of 100, 200 and 400 nm.

4.3.4 Additional Diffusion Layer

As shown in section 4.3.2, a substantial part of the selectivity towards the CO_2 reduction is diminished by the top half of the pores in the Ag-IO, where local concentrations of OH^- and CO_3^{2-} are not high enough to suppress the H_2 or promote the CO production, respectively. With thicker films or smaller pore diameters, the contributions of the top part of the mesoporous film relative to the overall fuel production of the film will be smaller, but the aforementioned phenomena will remain. In order to address this issue, an additional diffusion layer was introduced on top of the Ag-IO. From an experimental point of view, the most straightforward approach would be a passive layer using the same polystyrene sphere template than the Ag film. After the electrochemical deposition of Ag, another metal layer, with no activity towards CO_2 and water reduction, could be deposited in the same manner. For the calculations, pore diameters of 200 nm were considered and a micro roughness factor of 1 was assumed on the pore level. Zero current densities at the interface of the electrolyte and the passive layer was assumed. Figure 4.10a shows the gain factor in the maximum CO faradaic efficiency for Ag films with a thickness of 3, 6, 10 and 15 μm , and a layer thickness of the passive metal of 0.5, 1, 1.5, 2 or 3 μm . Evidently,

the thick Ag films with the additional diffusion layer, and with an already high CO faradaic efficiency, has less of a gain compared to the dramatic improvement for the thinner Ag films. For a 3 μm thick Ag-IO, the CO faradaic efficiency can be increased from 29% to over 58% by adding 3 μm of a passive layer. Whereas, with a 6 μm thick Ag film, the improvement is less drastic, yet the efficiency can be pushed above 91%. Figure 4.10b shows the effect of the thickness of the passive top layer on the current density distributions for a 3 μm thick Ag-IO at -0.7 V vs. RHE. The 3 μm thick diffusion layer reduces the increase to 75%, whereas the H_2 partial current density for the bare Ag film without the passive layer increases by 236% from the bottom of the electrode to the top. The introduction of an additional diffusion layer successfully suppresses the water reduction in the shallower pores of the Ag film. In addition, the CO faradaic efficiency is further improved throughout the whole electrode due to the increased diffusion path lengths.

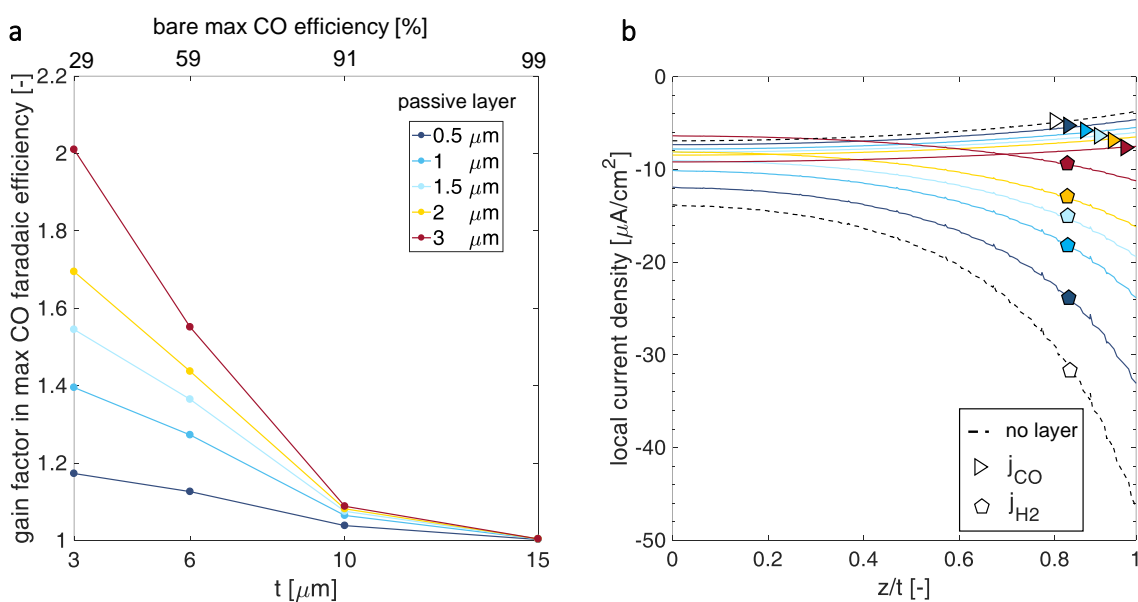


Figure 4.10 (a) The gain factor in the maximum CO faradaic efficiency by adding a passive layer with the same mesoporous structure on top of the Ag-IO. The added layer has a thickness between 0.5 and 3 μm . The maximum CO faradaic efficiency of the bare electrode (without a passive layer) is shown on the top x-axis. (b) The CO and H_2 evolution current density distribution along the z -axis for a 3 μm thick Ag-IO at -0.7 V vs. RHE with no added layer (dashed line) and passive layers (colored lines).

The concept of an additional diffusion layer on top of the Ag-IO can be extended by considering lower porosities, higher tortuosity or thicker films of the passive material. A porous domain, with thickness t_{diff} , was added on top of the Ag structure in our model. Within that porous domain, the diffusion coefficients were reduced by a factor p , resulting in the effective diffusion coefficient, D_{eff} :

$$D_{\text{eff}} = p \cdot D \quad (\text{e.g. } p = \varepsilon/\tau < 1) \quad (4.15)$$

The reduction of the effective diffusion coefficient, if not experimentally measured, could be extracted from the ratio of the porosity and tortuosity [31]. Inside the porous material of thickness t_{diff} , the buffer reactions were still considered. The mass transport through the porous layer is reduced by either decreasing p or increasing the thickness t_{diff} . Figure 4.11 quantifies the gain factor in the maximum CO faradaic efficiency as a function of the ratio of those two parameters. As a comparison, the passive metal layers (Figure 4.10a) with a thickness of 0.5 μm or 3 μm , correspond to a ratio p/t_{diff} of 1.74 or 0.29, respectively. Ratios larger than 1.2 are not shown in the contour plot, as their gain factors are small and not of particular interest. Figure 4.11 can be used as a design guideline to choose an appropriate diffusion layer on top of a mesoporous Ag-IO to boost the CO faradaic efficiency above 90% for a given film thickness. For an optimum CO_2 reduction electrode, the film thickness should be as large as experimentally possible to benefit from the large surface area, combined with the right diffusion layer to suppress the water splitting reaction in the upper part of the catalytic film.

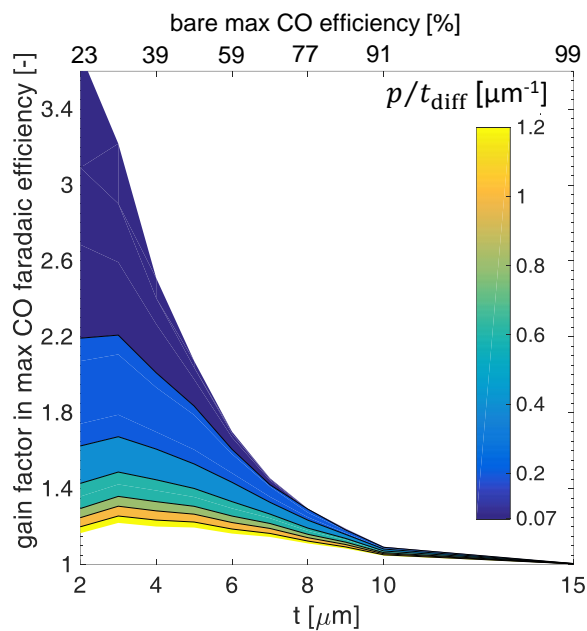


Figure 4.11 The gain factor in the maximum CO faradaic efficiency by an additional porous diffusion layer on top of the Ag-IO. p (<1) is the factor by which the diffusion coefficients are reduced in the porous media and t_{diff} is the thickness of the diffusion layer.

4.4 Conclusions

We introduced a finite element model on an accurate 3D geometrical representation of an ordered mesostructured Ag electrode. The model takes into account the mass transport and the electrolyte buffer reactions in the pore space and predicts the catalytic reaction rates at the electrolyte-Ag interface based on concentration dependent Butler-Volmer correlations. We have demonstrated that the dramatic suppression of the undesirable H₂ evolution reaction rate and the promotion of the CO evolution reaction rate as a function of the roughness factor can successfully be modeled by an inverse OH⁻ concentration dependency of the H₂ evolution exchange current density and a proportional dependency of the CO evolution exchange current density on the CO₃²⁻ concentration. The best agreement with experimental data was found for fractional reaction orders of 1.2 for both evolution rates. The model gives detailed insights on the local concentration distributions of CO₂(aq), OH⁻, HCO₃⁻, and CO₃²⁻ in the pore space. For a 0.1M KHCO₃ electrolyte, saturated with CO₂, the considered operation conditions for a maximum CO faradaic selectivity are far away from a mass transport limit of CO₂(aq). However, a substantial build-up of OH⁻ and CO₃²⁻ is observed in the lower part of the film, as the mass transport rate cannot keep up with the OH⁻ evolution rate. In contrast, the shallower pores exhibit low OH⁻ and CO₃²⁻ concentrations that is translated in locally high H₂ and low CO current densities. Therefore, a significant part of the CO faradaic efficiency of a mesostructured Ag electrode is lost in the top half of the catalytic film, due to a high mass transport rate. The morphology of the electrode, which the species need to diffuse through, can be described solely by the pore diameter. The pores are always stacked in a hexagonal close-packed arrangement in an FCC lattice, which is given by the colloidal polystyrene spheres template. The maximal achievable CO selectivity is dictated by the pore diameter and the film thickness. Both parameters directly influence the surface area, which is the key property to boost the CO faradaic efficiency. The goal is to have as much active Ag surface in regions where the OH⁻ and CO₃²⁻ concentrations are high. For a mesostructured Ag electrode with a pore diameter of 200 nm, a thickness of at least 10 μm is required to reach a CO selectivity above 90%. The film thickness can be substantially reduced when using a template with smaller spheres, as the surface area per film thickness is increased. A reduced film thickness could lead to more homogeneous deposition of Ag during the fabrication process of the electrode.

Based on the detailed insights from the model, we proposed a strategy to further increase the CO faradaic efficiency of a mesostructured Ag electrode with a given thickness. To address the low H₂ evolution rate suppression in shallow pores and to reduce the amount of expensive catalytic material, an additional diffusion layer can be introduced on top of the Ag electrode. Using the

Optimizing Reaction Selectivity by the Mesostructuring of Silver Catalysts

morphology from the same template, but depositing a non-catalytic material on top, can successfully increase the CO selectivity from 60% to more than 90%. We generalized the approach by characterizing the diffusion layer as a porous media with a certain thickness and reduced effective diffusion coefficients. The effect of the layer thickness and the reduction factor of the diffusion coefficient on the CO selectivity can be predicted by our model.

The results of our mass transport model are direct design guidelines for the fabrication of ordered, mesostructured Ag electrodes for the selective, and efficient CO₂ reduction reaction. In the considered parameter range, the electrode should be as thick as experimentally possible to ensure a high total CO evolution current, while a reduced pore size and an additional diffusion layer can dramatically boost the CO selectivity.

Further research is needed to quantify the empirical parameters on the Butler-Volmer correlations in order to apply the model using other catalytic materials, e.g. Cu. In this case, multi-layered mesostructured electrodes could be optimized, where e.g. the CO evolution on the Ag surface could be further converted to hydrocarbons on a Cu surface.

4.5 References

- [1] W. Tang *et al.*, “The importance of surface morphology in controlling the selectivity of polycrystalline copper for CO₂ electroreduction,” *Phys. Chem. Chem. Phys.*, vol. 14, no. 1, pp. 76–81, 2012.
- [2] K. P. Kuhl, T. Hatsukade, E. R. Cave, D. N. Abram, J. Kibsgaard, and T. F. Jaramillo, “Electrocatalytic conversion of carbon dioxide to methane and methanol on transition metal surfaces,” *J. Am. Chem. Soc.*, vol. 136, no. 40, pp. 14107–14113, 2014.
- [3] J.-P. Jones, G. K. S. Prakash, and G. A. Olah, “Electrochemical CO₂ Reduction: Recent Advances and Current Trends,” *Isr. J. Chem.*, vol. 54, no. 10, pp. 1451–1466, Oct. 2014.
- [4] Y. Hori, “Electrochemical CO₂ Reduction on Metal Electrodes BT - Modern Aspects of Electrochemistry,” C. G. Vayenas, R. E. White, and M. E. Gamboa-Aldeco, Eds. New York: Springer, 2008, pp. 89–189.
- [5] G. A. Olah, G. K. S. Prakash, and A. Goepfert, “Anthropogenic chemical carbon cycle for a sustainable future,” *J. Am. Chem. Soc.*, vol. 133, no. 33, pp. 12881–12898, 2011.
- [6] D. T. Whipple and P. J. A. Kenis, “Prospects of CO₂ utilization via direct heterogeneous electrochemical reduction,” *J. Phys. Chem. Lett.*, vol. 1, no. 24, pp. 3451–3458, 2010.
- [7] M. R. Singh, E. L. Clark, and A. T. Bell, “Thermodynamic and achievable efficiencies for solar-driven electrochemical reduction of carbon dioxide to transportation fuels,” *Proc. Natl. Acad. Sci.*, vol. 112, no. 45, pp. E6111–E6118, 2015.
- [8] J. Durst *et al.*, “Electrochemical CO₂ Reduction – A Critical View on Fundamentals, Materials and Applications,” *Chim. Int. J. Chem.*, vol. 69, no. 12, pp. 769–776, 2015.
- [9] M. Gattrell, N. Gupta, and A. Co, “A review of the aqueous electrochemical reduction of CO₂ to hydrocarbons at copper,” *J. Electroanal. Chem.*, vol. 594, no. 1, pp. 1–19, 2006.
- [10] R. R. Gutierrez and S. Haussener, “Modeling of Concurrent CO₂ and Water Splitting by Practical Photoelectrochemical Devices,” *J. Electrochem. Soc.*, vol. 163, no. 10, pp. H1008–H1018, 2016.
- [11] A. A. Peterson and J. K. Nørskov, “Activity descriptors for CO₂ electroreduction to methane on transition-metal catalysts,” *J. Phys. Chem. Lett.*, vol. 3, no. 2, pp. 251–258, 2012.
- [12] K. P. Kuhl, E. R. Cave, D. N. Abram, and T. F. Jaramillo, “New insights into the electrochemical reduction of carbon dioxide on metallic copper surfaces,” *Energy Environ. Sci.*, vol. 5, no. 5, pp. 7050–7059, 2012.
- [13] C. W. Li and M. W. Kanan, “CO₂ reduction at low overpotential on Cu electrodes resulting from the reduction of thick Cu₂O films,” *J. Am. Chem. Soc.*, vol. 134, no. 17, pp. 7231–7234, 2012.

- [14] A. Wuttig, Y. Yoon, J. Ryu, and Y. Surendranath, "Bicarbonate Is Not a General Acid in Au-Catalyzed CO₂ Electroreduction," *J. Am. Chem. Soc.*, vol. 139, no. 47, pp. 17109–17113, 2017.
- [15] Y. Hori, H. Ito, K. Okano, K. Nagasu, and S. Sato, "Silver-coated ion exchange membrane electrode applied to electrochemical reduction of carbon dioxide," *Electrochim. Acta*, vol. 48, no. 18, pp. 2651–2657, 2003.
- [16] Q. Lu *et al.*, "A selective and efficient electrocatalyst for carbon dioxide reduction," *Nat. Commun.*, vol. 5, pp. 1–6, 2014.
- [17] Y. Yoon, A. S. Hall, and Y. Surendranath, "Tuning of Silver Catalyst Mesostructure Promotes Selective Carbon Dioxide Conversion into Fuels," *Angew. Chemie - Int. Ed.*, vol. 55, no. 49, pp. 15282–15286, 2016.
- [18] H. Mistry, A. S. Varela, S. Kühn, P. Strasser, and B. R. Cuenya, "Nanostructured electrocatalysts with tunable activity and selectivity," *Nat. Rev. Mater.*, vol. 1, 2016.
- [19] A. S. Hall, Y. Yoon, A. Wuttig, and Y. Surendranath, "Mesostructure-Induced Selectivity in CO₂ Reduction Catalysis," *J. Am. Chem. Soc.*, vol. 137, no. 47, pp. 14834–14837, 2015.
- [20] N. Gupta, M. Gattrell, and B. MacDougall, "Calculation for the cathode surface concentrations in the electrochemical reduction of CO₂ in KHCO₃ solutions," *J. Appl. Electrochem.*, vol. 36, no. 2, pp. 161–172, 2006.
- [21] Y. Hori, A. Murata, and R. Takahashi, "Formation of hydrocarbons in the electrochemical reduction of carbon dioxide at a copper electrode in aqueous solution," *J. Chem. Soc., Faraday Trans. 1*, vol. 85, no. 8, pp. 2309–2326, 1989.
- [22] H. Ooka, M. C. Figueiredo, and M. T. M. Koper, "Competition between Hydrogen Evolution and Carbon Dioxide Reduction on Copper Electrodes in Mildly Acidic Media," *Langmuir*, vol. 33, no. 37, pp. 9307–9313, 2017.
- [23] K. J. P. Schouten, E. Pérez Gallent, and M. T. M. Koper, "The influence of pH on the reduction of CO and CO₂ to hydrocarbons on copper electrodes," *J. Electroanal. Chem.*, vol. 716, pp. 53–57, 2014.
- [24] M. R. Singh, Y. Kwon, Y. Lum, J. W. Ager, and A. T. Bell, "Hydrolysis of Electrolyte Cations Enhances the Electrochemical Reduction of CO₂ over Ag and Cu," *J. Am. Chem. Soc.*, vol. 138, no. 39, pp. 13006–13012, 2016.
- [25] M. R. Singh, E. L. Clark, and A. T. Bell, "Effects of electrolyte, catalyst, and membrane composition and operating conditions on the performance of solar-driven electrochemical reduction of carbon dioxide," *Phys. Chem. Chem. Phys.*, vol. 17, no. 29, pp. 18924–18936, 2015.
- [26] L. C. Weng, A. T. Bell, and A. Z. Weber, "Modeling gas-diffusion electrodes for CO₂

- reduction,” *Phys. Chem. Chem. Phys.*, vol. 20, no. 25, pp. 16973–16984, 2018.
- [27] H. Hashiba *et al.*, “Effects of electrolyte buffer capacity on surface reactant species and the reaction rate of CO₂ in Electrochemical CO₂ reduction,” *J. Phys. Chem. C*, vol. 122, no. 7, pp. 3719–3726, 2018.
- [28] D. Raciti, M. Mao, and C. Wang, “Mass transport modelling for the electroreduction of CO₂ on Cu nanowires,” *Nanotechnology*, vol. 29, no. 4, p. 044001, 2018.
- [29] S. Verma, X. Lu, S. Ma, R. I. Masel, and P. J. A. Kenis, “The effect of electrolyte composition on the electroreduction of CO₂ to CO on Ag based gas diffusion electrodes,” pp. 7075–7084, 2016.
- [30] D. Hung, Z. Liu, N. Shah, Y. Hao, and P. C. Searson, “Finite Size Effects in Ordered Macroporous Electrodes Fabricated by Electrodeposition into Colloidal Crystal Templates,” *J. Phys. Chem. C*, vol. 111, no. 8, pp. 3308–3313, Mar. 2007.
- [31] E. L. Cussler, “Diffusion: Fundamentals of Mass Transfer,” in *Diffusion: Fundamentals of Mass Transfer*, Cambridge: Cambridge University Press, 2011, pp. 237–273.
- [32] B. P. Sullivan, K. Krist, and H. E. Guard, *Electrochemical and electrocatalytic reactions of carbon dioxide*. Elsevier, 2012.

Implementing Light Trapping on Thin Film, Mesostructured Fe₂O₃ Photoanodes

5.1 Introduction

Photoelectrochemical water-splitting offers an opportune strategy to produce hydrogen sustainably for industrial applications and solar energy storage. Besides a solar-to-hydrogen (STH) efficiency of at least 10% and low material costs for large area panels, a practical device relies on the durability of its components [1]. The required standards regarding the chemical stability are especially high for the semiconductor films of the photoelectrodes that are in direct contact with the electrolyte. Hematite (α -Fe₂O₃) has for years been extensively studied as a photoanode due to its excellent stability in aqueous and alkaline solutions [2]. With light absorption in the visible range (energy bandgap: 2.1 eV), a maximal theoretical current density of 12.6 mA/cm² can be achieved under air mass 1.5 global (AM1.5G) [3]. α -Fe₂O₃ also has the benefit of being non-toxic and abundant, which makes the sourcing of the material and the fabrication of a device cheap [4]. However, low efficiencies in charge injection, charge separation, and light absorption have so far hindered the capacity of α -Fe₂O₃ photoanodes to 5% STH [5]. To address the low charge injection efficiencies associated with slow water oxidation kinetics, catalysts have been developed to increase the turnover number of the reaction significantly [6], [7]. The charge separation and light absorption efficiencies are coupled in the bulk material and pose the main obstacle for a better device performance. With the hole diffusion length two orders of magnitude smaller than the absorption length [8], a substantial part of the generated electron-hole pairs recombine before reaching the surface in a thick film. A strategy to overcome the discrepancy in length scales is the nanostructuring of the material by keeping the penetration length of the light high but reducing the transport paths of minority carriers. Successful decoupling of the charge separation and light

absorption has been demonstrated with α -Fe₂O₃ nanowires [9] and cauliflower-shaped pillars [10], but bulk recombination stayed dominant, and surface recombination increased due to the enlarged surface area. Another approach is the deposition of ultra-thin α -Fe₂O₃ films of a few nanometers to effectively reduce the bulk recombination. By applying ultrasonic spray pyrolysis [11], atomic layer deposition [12] or pulsed laser deposition [13], thin films produced with high internal quantum efficiency (IQE) were reported. These thin films have a low absorptance, unless they are deposited on a host-guest scaffold to increase the light penetration depth [12] or engineered light trapping mechanisms are applied. Dotan et al. [13] demonstrated resonant light trapping using a 26 nm thick Ti-doped α -Fe₂O₃ film on a planar glass substrate covered with a reflective silver layer, reaching photocurrents of 2.9 mA/cm² at 1.63 V vs. RHE. The photocurrent was further improved to 4 mA/cm² by placing two flat films in a 90° V-shape to benefit from the harvest of reflected photons. The applied strategy is compelling, as the deficits in charge separation and light absorption efficiencies were addressed without increasing the surface area more than necessary. The same approach with resonant and geometrical light trapping can be taken to the microscale. Computational studies have investigated the influence of the shape of transparent substrates covered by a thin α -Fe₂O₃ layer on the overall light trapping efficiency. Increased light absorption was demonstrated with transparent, stacked TiO₂ particles [14] and FTO pillars [15], and ITO cones, with an aluminum backing layer and heights taller than 1 μ m, reached nearly total solar absorption [16]. These results promise that a combination of resonant light trapping in thin films and an optimal microstructure of the substrate can substantially improve the performance of α -Fe₂O₃ photoanodes. However, none of the computed microstructures have been tested experimentally, potentially due to the challenges of fabricating such patterned substrates with a high enough precision and uniform coverage with a thin layer of α -Fe₂O₃. For photovoltaic applications, geometric light trapping with pyramidally textured silicon has been realized to minimize the reflective losses of solar cells [17]–[19]. Anisotropic etching of silicon in potassium hydroxide exposed intersecting (111) crystallographic planes that formed square-based pyramids. This light trapping scheme could also be applied to thin film photoelectrochemical electrodes by depositing a conductive layer and a semiconductor onto the patterned silicon wafer. However, transferring the morphology onto a cheaper substrate material would not only reduce the fabrication costs, but also open new routes for having patterned photoelectrochemical electrodes on a variety of substrates, including flexible materials. Furthermore, a film transfer of multilayered electrodes, deposited in reverse order, allows for the annealing of the α -Fe₂O₃ at high temperatures before depositing the heat-sensitive reflective silver layer, as demonstrated by Kay et al. [20]. With this approach, the reflectivity of the silver layer stays high and is not affected by thermal etching. For the more specific topology transfer,

Implementing Light Trapping on Thin Film, Mesostructured Fe₂O₃ Photoanodes

template-stripping processes have been used in photonics to transfer microstructures from a silicon wafer to a variety of materials [21], [22]. Gold is applied as a low adhesion layer between the silicon and the desired materials and substrate. Mechanical stripping of the substrate did not damage the silicon wafer, and the template could be reused multiple times.

Herein we report a new template-stripping process to fabricate thin film α -Fe₂O₃ photoanodes that incorporate both, resonant and geometric light trapping. First, numerical calculations of the electromagnetic wave propagation quantify the potential gain of thin α -Fe₂O₃ films deposited on transparent or reflective wedge microstructures compared to a planar design. We then propose two process flows (A): “strip then deposit” and B): “deposit then strip”) to fabricate those microstructured photoanodes on a flexible substrate. A patterned silicon wafer is used as a template, and the final photoanodes are characterized in a photoelectrochemical measurement setup.

5.2 Resonant and Geometric Light Trapping in Thin Films on Wedge Structures

5.2.1 Model Description and Governing Equations

Model

We consider an anode in a photoelectrochemical water splitting device with a thin film semiconductor and a transparent or reflective back contact. The 2D model consists of a water domain, a semiconductor layer, and a back contact layer in either a planar or a structured wedge configuration. Figure 5.1 shows the model domain for the latter configuration, where the electromagnetic wave propagates through the absorbing water, semiconductor and back contact layers with reflections at the water-semiconductor and semiconductor-back contact interfaces. In case of a reflective back contact, resonant wave modes, dependent on the wavelength and the semiconductor film thickness, are expected. The wedge introduces geometric light trapping where reflected photons are hitting the semiconductor layer for a second or third time. Parameters that define the geometry are the angle of the wedge, γ , the domain section width, $2d_{sc}$, and the aspect ratio of the wedge base vs. the domain section width, $R_w=L_p/d_{sc}$. The electromagnetic wave simulating solar irradiation at AM.1.5G is defined as an input at the top boundary, indicated by $P(\lambda)$, with an incident angle described by α_i . Both in-plane and out-of-plane polarization of the light is modeled, which is further referred to as transverse electric (TE) or transverse magnetic (TM) waves, respectively. A perfectly matched layer (PML), with the material properties of water, eliminates any reflected wave crossing over the input boundary. Floquet periodicity is applied to the lateral boundaries.

To quantify the enhancement in light absorption through resonant and geometric light trapping, the following parameters were varied: the film thickness, d_{film} , the wedge angle, γ , and the aspect ratio, R_w . The section width was kept constant at $2d_{sc}=6 \mu\text{m}$. Hematite, $\alpha\text{-Fe}_2\text{O}_3$, was chosen as the absorbing semiconductor material and four different back contact materials were investigated: (i) a perfect transparent layer ($R=0$), modeled as a thick layer with the same material properties as the semiconductor, but with scattering boundaries, (ii) a perfect reflective layer ($R=1$), modeled as a perfect electric current collector, (iii) a Ag, and (iv) a Pt back contact. Both the absorbed photon fluxes in the semiconductor, as well as realistic current densities at the semiconductor-water interface were calculated. We further assessed the sensitivity of the light absorption on the angle of the incoming light. An air-glass and a glass-water interface was considered and the incident angle, α_i , and the incoming power, $P(\lambda)$, were adapted using the Fresnel law. Finally, the dependency of the photocurrent on the scale of the wedge structure was studied by varying the section width, d_{sc} .

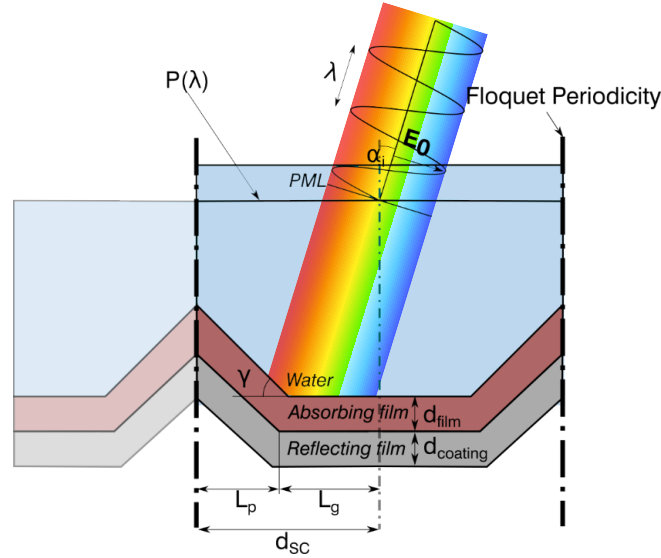


Figure 5.1 2D simulation domains for a photoanode with a wedge structure. Solar irradiation (AM1.5G) enters the water domain at an angle α_i , propagates through the absorbing water, semiconductor, and backing film, with reflections at the interfaces. Resonant light trapping in the thin semiconductor film, as well as geometric light trapping due to the wedge structure are expected. The Floquet periodicity is applied at the lateral boundaries, and the input boundary is backed by a perfect matching layer to eliminate reflected waves crossing the input boundary.

All the domains were meshed using triangular shaped second order elements except the PML, where a mapped mesh with quadrilateral elements were used. The maximum element size was a fifth of the shortest wavelength in the media. A refinement was introduced in the hematite layer to have at least five elements over the thickness. A mesh study confirmed the independence from the element size for the used grid.

The Maxwell equations were solved using the software *Comsol 5.3* with the RF module. The postprocessing was done in *Matlab R2017b*.

From the Maxwell Equation to Light Absorption

In all the simulation domains, the Maxwell curl equation is solved for the electric field \mathbf{E}

$$\nabla \times (\nabla \times \mathbf{E}(x, y, \lambda)) - \left(\frac{2\pi c}{\lambda}\right)^2 \mu \epsilon(x, y, \lambda) \mathbf{E}(x, y, \lambda) = 0 \quad (5.1)$$

Implementing Light Trapping on Thin Film, Mesostructured Fe2O3 Photoanodes

with the wavelength, λ , the speed of light, c , the complex permittivity, ϵ , the complex permeability, μ , and the position, (x, y) . Starting from the Maxwell equation for a linear media (assuming that the permittivity, ϵ , and the permeability, μ , do not depend on the electric field \mathbf{E} nor the magnetic field \mathbf{H}), the Poynting theorem can be derived to evaluate the energy absorbed in a material [23]:

$$\begin{aligned}
 & \underbrace{\frac{1}{2} \int_V (\mathbf{E} \cdot \mathbf{J}_s^* + \mathbf{H}^* \cdot \mathbf{M}_s) dv}_{P_s} \\
 &= \underbrace{\frac{1}{2} \oint_S \mathbf{E} \times \mathbf{H}^* \cdot d\mathbf{s}}_{P_o} + \underbrace{\frac{\sigma}{2} \int_V |\mathbf{E}|^2 dv + \frac{\omega}{2} \int_V (\epsilon'' |\mathbf{E}|^2 + \mu'' |\mathbf{H}|^2) dv}_{P_1} \\
 &+ j \underbrace{\frac{\omega}{2} \int_V (\mu' |\mathbf{H}|^2 - \epsilon' |\mathbf{E}|^2) dv}_{2j\omega(W_m - W_e)} \quad (5.2)
 \end{aligned}$$

where \mathbf{J}_s^* is the complex conjugate of the electric source current, σ the conductivity, \mathbf{M}_s is the magnetic source and the superscripts ' and '' indicate the real or complex part respectively of the permittivity and the permeability. Equation (5.2) relates the power delivered by the sources \mathbf{J}_s and \mathbf{M}_s (P_s) to the power flow out of the closed surface (P_o), the time-averaged power dissipated due to conductivity, dielectric and magnetic losses (P_1), and $2j\omega$ times the net reactive energy stored in the volume ($W_m - W_e$).

Taking the real part of Equation (5.2) and considering non-magnetic materials [24] without source terms, the equation simplifies to

$$\text{Re} \left(\frac{1}{2} \oint_S \mathbf{E} \times \mathbf{H}^* \cdot d\mathbf{s} \right) + \frac{\omega}{2} \left(\frac{\sigma}{\omega} + \epsilon'' \right) \int_V |\mathbf{E}|^2 dv = 0 \quad (5.3)$$

Using the complex dielectric function, ϵ [25]:

$$\epsilon'' = \epsilon_0 \text{Im}(m^2) = \epsilon_0 2nk = \frac{\sigma}{\omega} + \epsilon'' \quad (5.4)$$

with the complex refractive index $m=n-ik$ and the permittivity in vacuum, ϵ_0 , the losses in the material can be expressed as

$$P_1 = \frac{\omega}{2} \epsilon_0 2nk \int_V |\mathbf{E}|^2 dv = \int_x \int_y \omega \epsilon_0 nk |\mathbf{E}|^2 dx dy = \int_x \int_y \mathbf{p}_1 dx dy \quad (5.5)$$

This expression is favored over the real part of the divergence of the Poynting vector due to its numerical robustness [26].

To obtain the photogeneration rate, g , the dissipated power normalized by the photon energy is integrated over the wavelength until the bandgap wavelength of the semiconductor (for α -Fe₂O₃ bandgap=2.1 eV; $\lambda=590$ nm) [27].

$$g(x, y) = \int_{\lambda_0}^{\lambda_{Eg}} \frac{\mathbf{p}_1(x, y)}{hc/\lambda} d\lambda = \int_{\lambda_0}^{\lambda_{Eg}} \frac{2\pi\epsilon_0 nk |\mathbf{E}|^2}{h} d\lambda \quad (5.6)$$

From Light Absorption to the Photocurrent Density

The photogeneration rate quantifies the absorbed photons per unit time and unit volume within the semiconductor film. However, in a photoanode, only the minority charge carriers, that reach the front interface with the electrolyte and are forward injected, contribute to the electrochemical reaction quantified by the photocurrent. Bulk recombination in the film, surface recombination at the front interface, and back injection at the current collector reduce the ratio of the photogenerated minority carriers to the final photocurrent. This ratio is described by the internal quantum efficiency (IQE), and a 1D probability model is used to quantify it. Dotan et al. [13] used the same model and could fit it well to experimental data of ultrathin hematite films on reflective coatings.

$$IQE(y) = P_F \Phi e^{-y/L} - P_B (1 - \Phi) e^{-(d-y)/L} \quad (5.7)$$

Implementing Light Trapping on Thin Film, Mesostructured Fe₂O₃ Photoanodes

In this equation, the probability of minority charge carriers being separated from the majority carriers and transported towards the electrolyte interface is described by Φ . The probability of minority charge carriers to reach the surface decreases exponentially with the distance y from the electrolyte interface divided by the material dependent collection length, L . P_F quantifies the probability of a charge carrier at the electrolyte interface to participate in the water splitting process, whereas P_B describes the probability of a minority carrier to be back injected into the current collector and thereby reduces the photocurrent. These parameters are empirical and depend on the doping level and the deposition method of the semiconductor, as well as the operating conditions. Experimentally validated values for thin film Ti-doped α -Fe₂O₃ are: $\Phi=0.74$, $P_F=0.95$, $P_B=1$, and $L=20$ nm. The IQE for these values is shown in Figure 5.2a. For thin films, the probability is generally lower as the backward injection reduces the IQE in the whole film. From a certain thickness, the IQE even becomes negative as the backward injection efficiency is so large. These results show how important it is to photogenerated minority carriers as close as possible to the electrolyte interface.

The photocurrent is then calculated as the product of the photogeneration rate and the IQE, which is integrated over the film thickness times the elementary charge q .

$$i_{\text{photo}} = q \int_0^d \int_x g(x, y) dx \cdot IQE(y) dy \quad (5.8)$$

For the configuration with the wedge, g is first integrated perpendicular to the film thickness as shown in Figure 5.2b, and normalized by the section width, $2d_{sc}$, and then integrated along the film thickness.

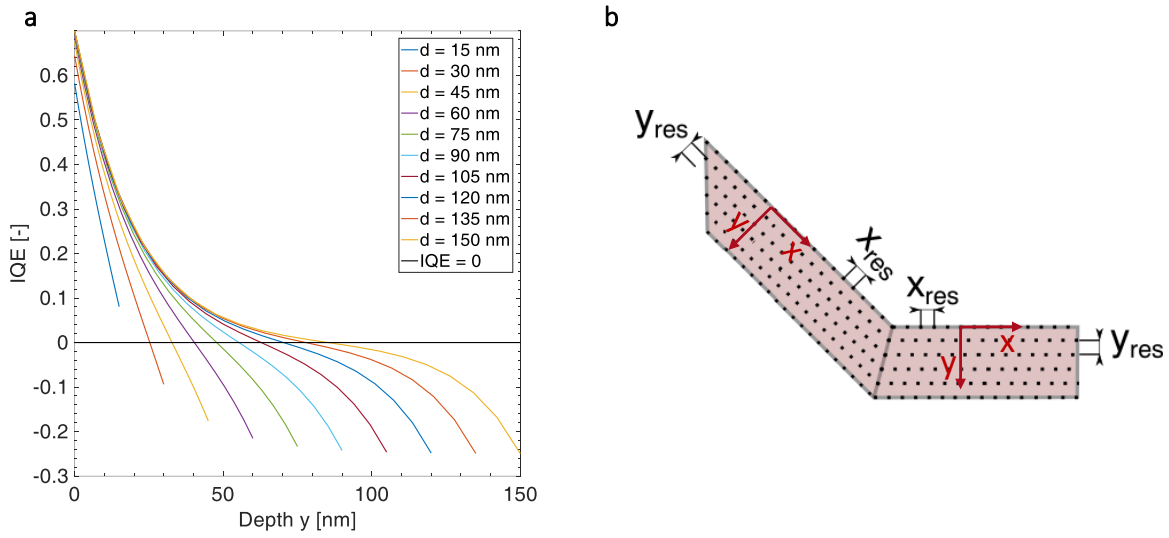


Figure 5.2 (a) Internal quantum efficiency for different film thicknesses as a function of the depth y in the film for empirical parameters: $\Phi=0.74$, $P_F=0.95$, $P_B=1$, and $L=20$ nm. (b) Integration points.

Material Properties and Solar Spectrum

The complex refractive indices for water and $\alpha\text{-Fe}_2\text{O}_3$ were taken from reference [28] and [13], respectively (Figure 5.3a-b). The complex refractive indices for Pt and Ag (on a ultrathin SiO_2 layer), taken from reference [29] and [30], respectively, were compared to values extracted from the measured complex reflection coefficients of $\alpha\text{-Fe}_2\text{O}_3$ on Pt and Ag with a ultrathin SnO_2 layer in between from reference [13] (Figure 5.3c-f). The complex reflection coefficient is defined as a function of m_2 ($\alpha\text{-Fe}_2\text{O}_3$) and m_3 (Pt or Ag):

$$\hat{r}_{23} = \frac{m_2 - m_3}{m_2 + m_3} \quad (5.9)$$

and it can be solved for m_3 . The comparison shows a big discrepancy for the Pt film. As an ultrathin SnO_2 layer is needed in a efficient photoanode, the values extracted from reference [13] were used.

Implementing Light Trapping on Thin Film, Mesostructured Fe₂O₃ Photoanodes

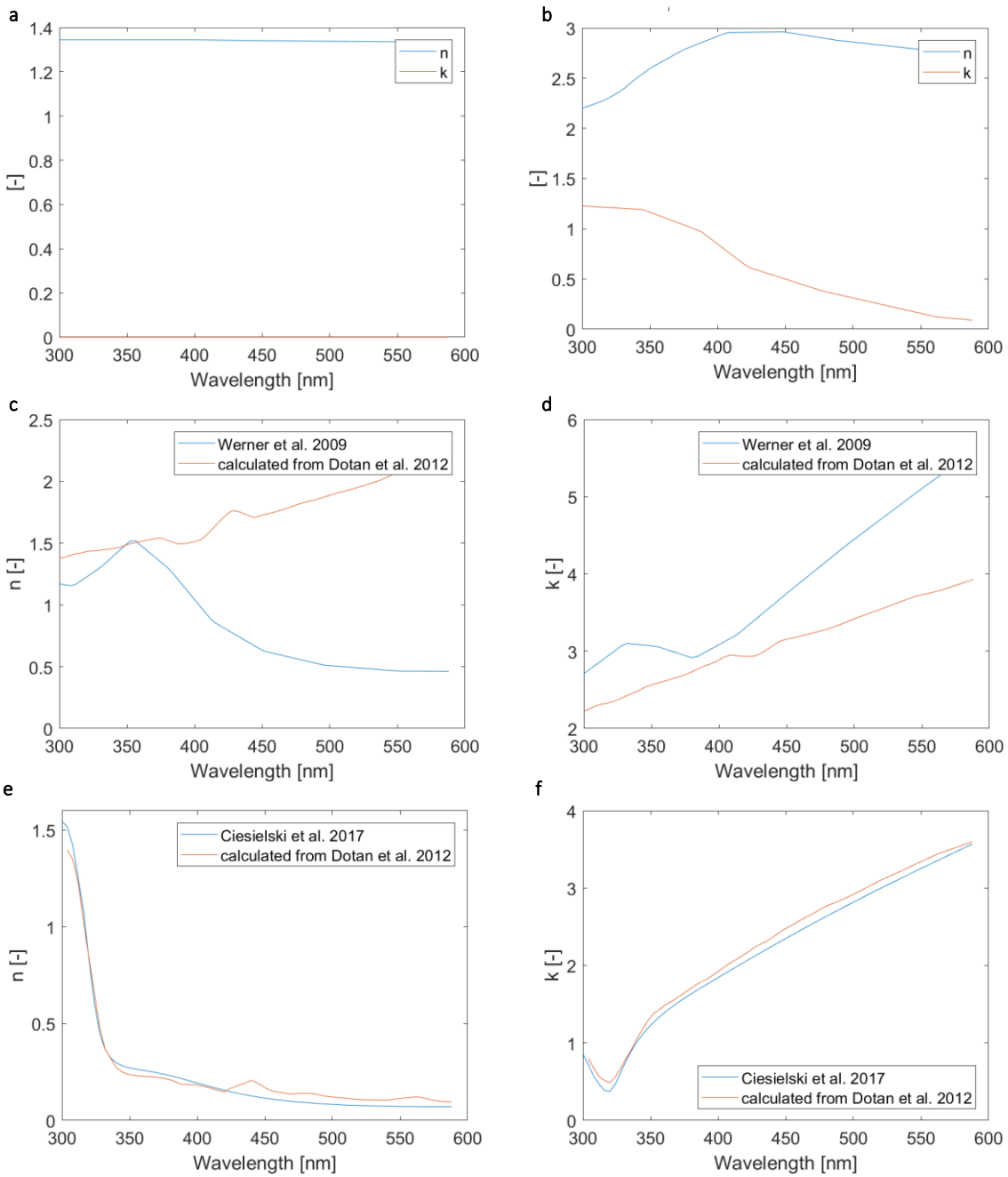


Figure 5.3 Complex refractive indices. (a) water [28], (b) α -Fe₂O₃ [13], (c-d) Pt [29] and Pt on ultrathin SnO₂ [13], (e-f) Ag on ultrathin SiO₂ [30] and Ag on ultrathin SnO₂.

Implementing Light Trapping on Thin Film, Mesostructured Fe₂O₃ Photoanodes

In the Fresnel law, the real part of the refractive indices for air, $n_{\text{air}}=1$, glass, $n_{\text{glass}}=1.47$, and water, $n_{\text{water}}=1.34$, were taken.

The spectrum of the solar irradiation at AM1.5G is shown in Figure 5.4.

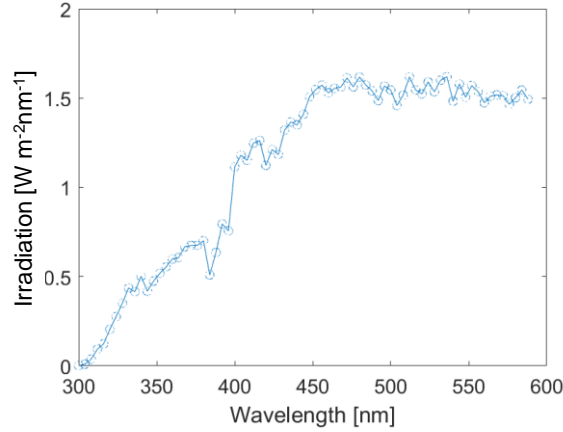


Figure 5.4 Solar spectrum at AM1.5G with $d\lambda=4$ nm.

5.2.2 Results and Discussion

Model Validation

Our results of planar α -Fe₂O₃ photoanodes with an ultrathin SnO₂ layer on a Pt or Ag current collector were compared to values reported by Dotan et al. [13] in order to validate our 2D model of electromagnetic wave propagation and absorption. The data of the referred study were obtained by deriving analytical expressions for the spectral photon flux profiles from the plane-wave solution of the Maxwell equation. They measured the complex refractive index of α -Fe₂O₃ and the reflection coefficient of the hematite-current collector interface and validated their results experimentally with a fitted IQE probability function. For a normal incident solar radiation at AM1.5G, the photogenerated rates in the hematite film were calculated and then integrated and multiplied by the elementary charge to obtain the photogenerated current density $i_{\text{photo,g}} = q \int_0^d \int_x g(x,y) dx dy$. The current density is normalized by the section width, $2d_{\text{SC}}$. Figure 5.5 shows good agreement to the reference model with material properties extracted from the same study. For a Ag reflective layer, the resonant behavior is slightly less pronounced with the photogenerated current density at the peak of the first resonance mode 8% smaller, and 14%

Implementing Light Trapping on Thin Film, Mesostructured Fe₂O₃ Photoanodes

larger at the first minimum compared to the reference model. The maximum is shifted from 26 to 28 nm, but the minimum is in both cases at 60 nm film thickness. A similar trend is seen for an α -Fe₂O₃ film on a platinized substrate, with an 8% larger minimum and positive shifts of 4 and 2 nm in film thickness. The results of the model are sensitive to the values of the complex refractive indices and the measurement errors in reference [13]. The complex refractive indices and the reflection coefficient, as well as random errors when extracting the values, can explain the small discrepancies. However, when using a complex refractive index of platinum, without considering the ultrathin SnO₂ film, much higher photogenerated current densities were obtained. Overall, the differences stayed within acceptable margins, which validates the model.

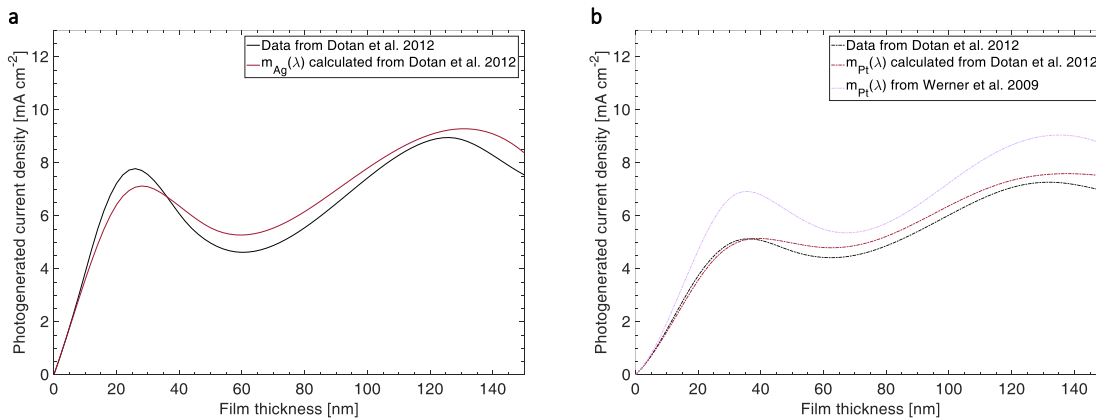


Figure 5.5 Photogenerated current densities for the α -Fe₂O₃ film on (a) an Ag or (b) a Pt reflective layer. Using the complex refractive indices from Dotan et al. [13], the model is validated. A complex refractive index for Pt without considering the ultrathin SnO₂ layer from Werner et al. [29] leads to much higher photogenerated current densities.

Light Absorption

Our strategy is to enhance the light absorption in thin α -Fe₂O₃ films by resonant and geometric light trapping. An α -Fe₂O₃ film on a planar and perfectly transparent ($R=0$) substrate is the reference case to assess the enhancement in light absorption for different electrode configurations. To achieve resonant light trapping, we considered a perfect reflective layer ($R=1$), and metalized Ag and Pt current collectors. The semiconductor film thickness is the one degree of freedom to maximize the effect of the electromagnetic wave resonance and was varied between

15 and 160 nm. Geometric light trapping was investigated using the same semiconductor-current collector stack configurations on a wedge structure. The wedge angle, γ , was varied between 45° and 70° and the aspect ratio, R_w , was altered between 0.65 and 0.95. For the lowest aspect ratio, the distance between the two wedges is 2.1 μm , whereas in the latter case it is reduced to 0.3 μm . The results of the transverse electric (TE) and the transverse magnetic (TM) input waves were averaged for all the calculations shown in this section.

For normal incident light, the calculated photogeneration rates per unit time, unit area (section width, $2d_{sc}$), and unit film thickness are shown in Figure 5.6 for the eight configurations, each at four different film thicknesses. The film thickness is normalized for visualization purposes. The absorbed photon flux is normalized by its maximum value for each configuration and designated by ξ . For the planar, transparent reference configuration, the light is absorbed exponentially, following Beer-Lambert's law. A perfect reflective current collector creates an absorbed photon flux profile that is periodically dependent on the $\alpha\text{-Fe}_2\text{O}_3$ film thickness. For a thin film (16 nm), the incoming and reflected waves interfere destructively, and the light intensity is suppressed, leading to a lower light absorption compared to the reference case. With increasing film thickness, the light absorption increases and reaches the first resonant mode at around 45 nm. The maximum photon flux is three times higher than in an $\alpha\text{-Fe}_2\text{O}_3$ film on a transparent substrate, and the peak is located at the electrolyte interface. At the reflective current collector, the phase shift between the forward and backward propagating wave is π , and the waves cancel each other out. The benefits of this configuration are the substantial light enhancement within the distance of the hole diffusion length [8], and the suppression of minority charge carrier generation near the back contact where backward injection would reduce the photocurrent. There is also a clear optimum as the absorbed photon flux is near a minimum at a film thickness of 90 nm. Similar behavior occurs for not perfect reflective layers like an Ag or Pt coating. The first resonant mode for an Ag current collector is shifted to a lower $\alpha\text{-Fe}_2\text{O}_3$ film thickness. This phenomena has already been reported and is explained by a phase shift larger than π for reflections at the Ag- Fe_2O_3 interface [13]. Furthermore, the highest absorbed photon fluxes are seen in the configuration with the Ag reflective layer. However, they occur at much thinner films, and the overall photogeneration rate will be lower compared to the configuration with the perfect reflective layer. Pt is not a particularly good reflective layer, and the coating absorbs a substantial part of the incoming radiation.

The benefit of geometric light trapping is seen for an $\alpha\text{-Fe}_2\text{O}_3$ -transparent layer stack on a wedge structure with an angle $\gamma=54^\circ$ and an aspect ratio $R_w=0.8$ (Figure 5.6e). The exponential decrease in absorbed photon flux along the film thickness is overlapped by retrapping of reflected photons

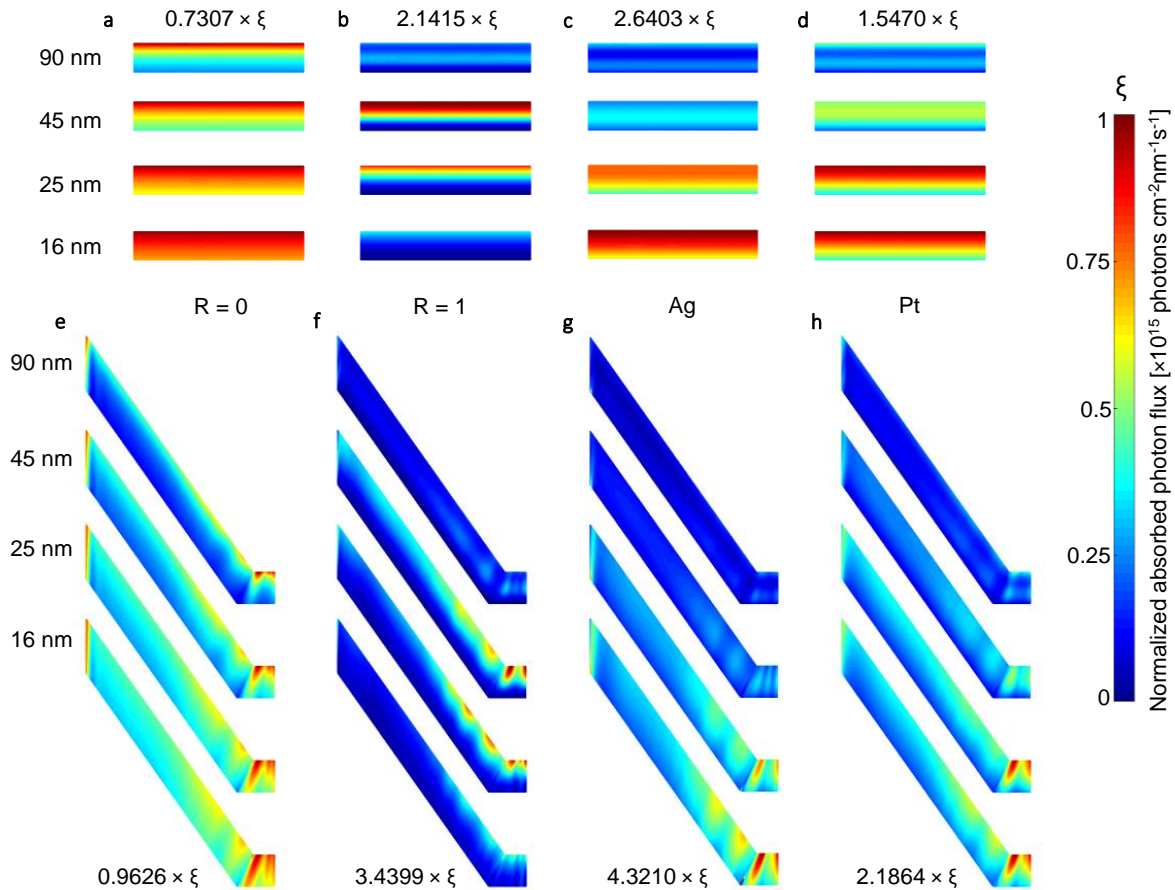


Figure 5.6 Absorbed photon flux maps per unit time, unit area and unit film thickness for four different film thicknesses. The film thicknesses are normalized for visualization purposes. Electrodes stacks with $\alpha\text{-Fe}_2\text{O}_3$ films on planar, (a) perfectly transparent, (b) perfectly reflective, (c) Ag, (d) Pt current collector. Symmetry unit cell of the wedge structure with an $\alpha\text{-Fe}_2\text{O}_3$ film on (e) perfectly transparent, (f) perfectly reflective, (g) Ag, (h) Pt current collector.

from the semiconductor-electrolyte interface. Enhanced light absorption occurs around the wedge base and the tip. Photons reflected from the slope of the wedge hit the flat area between wedges and the slope of the opposite wedge, boosting the overall light absorption. A maximum of two hotspots on the wedge slope and the flat part of the electrode are characteristic for the given wedge parameters. Moreover, the continuous increase of the diameter of the wedge tip offers a space confinement for every wavelength to reach its first resonant mode. These phenomena are observed in all four wedge configurations, resulting in substantially higher

maximum photon fluxes compared to the planar counterparts. However, the inhomogeneity of the resulting photocurrent density distribution at the semiconductor interface could lead to kinetic limitations and should be kept in mind when discussing the results in the next section. The wedge structure with a perfect reflective layer still benefits from the anti-phase wave interference at the current collector and the constructive interference at the electrolyte interface. For an Ag reflective layer, the resonant modes shift again to smaller film thickness, and for the Pt reflective layer, the same observations apply, as in the planar case.

The light absorption in the entire α -Fe₂O₃ film as a function of the film thickness was quantified for the eight configurations by integrating the calculated photogeneration rate over the semiconductor domain for each film thickness. The results for the planar and the wedge ($\gamma=54^\circ$, $R_w=0.8$) configuration are shown in Figure 5.7a as an absorbed photon flux per unit time and unit area. Multiplied by the elementary charge, q , the photogenerated current density, assuming an IQE=1, is obtained. The theoretical maximum for α -Fe₂O₃ at AM1.5G is 12.6 mA cm⁻². The absolute absorbed photon flux of the reference case with the α -Fe₂O₃ film on a planar, transparent substrate increases steadily with the film thickness. By applying geometric light trapping, the light absorption can be enhanced between 18% ($d_{\text{film}}=20$ nm) and 15% ($d_{\text{film}}=160$ nm), as shown in Figure 5.7b, with a gain factor relative to the reference case. All planar configurations with a reflective layer exhibit two resonant modes in the range of the considered film thickness. The first local maximum occurs at a film thickness of 49, 28, and 39 nm for a perfect reflective, an Ag, and a Pt layer, respectively. The first resonant mode is shifted to thicker films when the same stacks are applied on a wedge structure with a maximum at 55 and 34 nm for a perfect reflective and an Ag coating, respectively. No local maximum and minimum exist for a Pt-coated wedge structure. The decrease in light absorption due to destructive interference must be compensated by the retrapping of reflected photons. Overall, the substantial enhancement in the light absorption due to the resonant light trapping strategy is further increased by geometric light trapping. By introducing a wedge structure with $\gamma=54^\circ$, and $R_w=0.8$, the gain factor is increased in a range of 0.23-0.58, 0.23-1.1, and 0.1-0.33 for a perfect reflective, an Ag, and a Pt layer, respectively. The absolute absorbed photon flux at the first maximum compared to the planar counterpart is enhanced by 24% and 25% for a perfect reflective and an Ag layer, respectively. Also, the peaks of the resonant mode are broadened, and the oscillation between the peaks and the valleys are damped, reducing the stringent requirement for the thickness control when fabricating α -Fe₂O₃ films.

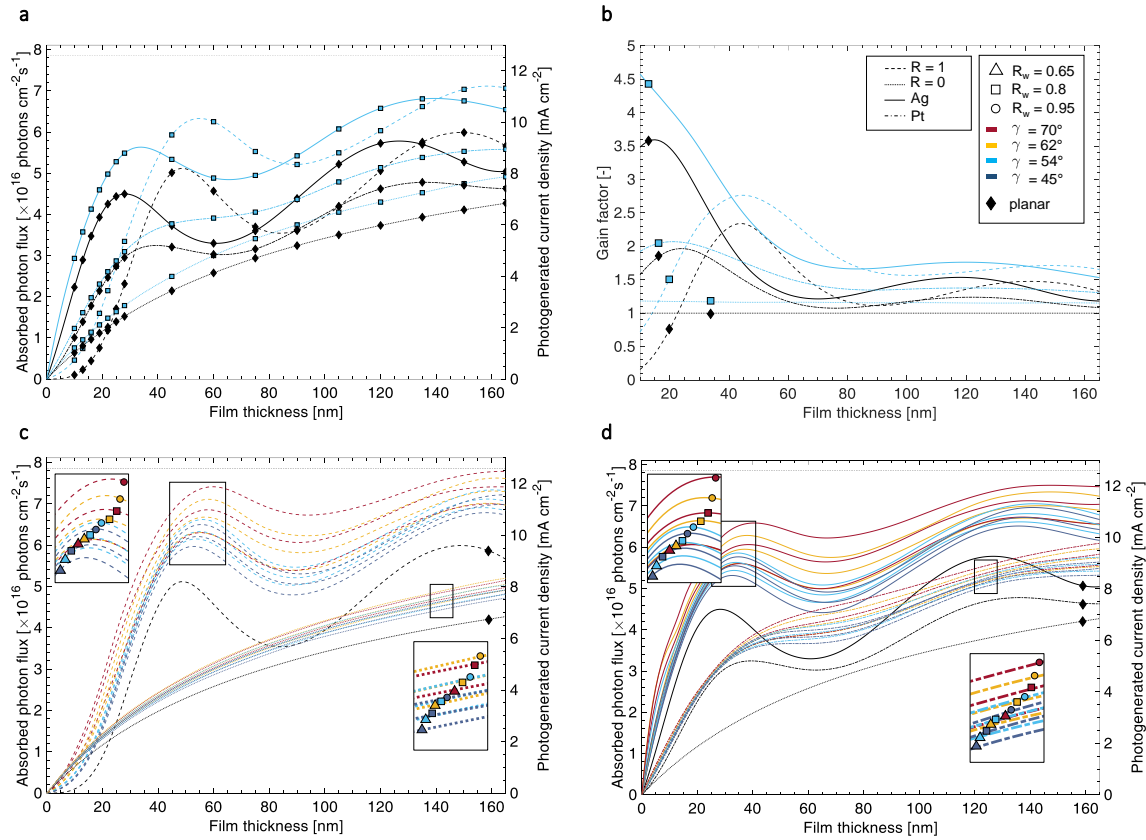


Figure 5.7 Integrated absorbed photon flux profiles as a function of the film thickness. The indicated photogenerated current density assumes an IQE=1. (a) Comparing a wedge structure ($\gamma=54^\circ$, $R_w=0.8$) (blue) to planar electrodes (black) for perfect reflective (dashed), transparent (dotted), Ag (solid), and Pt (dash-dot) current collectors. (b) Gain factors with the planar, transparent current collector as a reference. Flux profiles for wedge structures with different angles, γ , and aspect ratios, R_w , with (c) perfect reflective, and transparent, and (d) Ag, and Pt current collectors. The planar, transparent reference case is also included in (d). All close-up windows are not in scale.

Varying the geometric parameters of the wedge structure has a direct effect on the light trapping, as shown in Figure 5.7c-d. Substantial improvements for the absorbed photon flux are predicted when increasing the steepness of the wedge slope and decreasing the gap between wedges, leading to values near the theoretical limit. The enhancement for the champion structure ($\gamma=70^\circ$, $R_w=0.95$) is 45% and 47%, compared to the absolute absorbed photon flux of the planar counterpart for a perfect reflective and an Ag layer, respectively. The previously discussed trends

Implementing Light Trapping on Thin Film, Mesostructured Fe₂O₃ Photoanodes

of broadened peaks with shifts to thicker films and damped oscillation continue when γ and R_w are increased. It seems that the damping is more sensitive to the wedge angle, and for the Pt-coated substrate, the oscillation disappears for $\gamma=70^\circ$, showing a similar behavior like the transparent substrate. The reflectivity of the Pt coating is low, and the effective light trapping mode is based on the wedge geometry.

Photocurrent

The light absorption calculations predict how many photons are absorbed in the entire α -Fe₂O₃ film. However, it is essential to know where the photons are absorbed as the IQE is not ideal and the charge collection length for α -Fe₂O₃ is in the nanometer range. To predict realistic photocurrent densities, a 1D empirical probability model was applied to take into account losses through bulk and surface recombination, as well as backward-injections into the current collector. In a first approach, we assume ideal forward-injection conditions with the probability of minority charge carriers to be separated from the majority carriers and to be transported towards the electrolyte interface $\Phi=1$ and the probability of a charge carrier at the electrolyte interface to participate in the water-splitting process $P_F=1$. This conditions can be achieved by applying high overpotentials and by implementing strategies to prevent backward-injection of minority carriers with a hole-transport blocking layer [13]. With the chosen parameters, the IQE simplifies to $IQE(y) = e^{-y/L}$ with $y=0$ at the electrolyte interface.

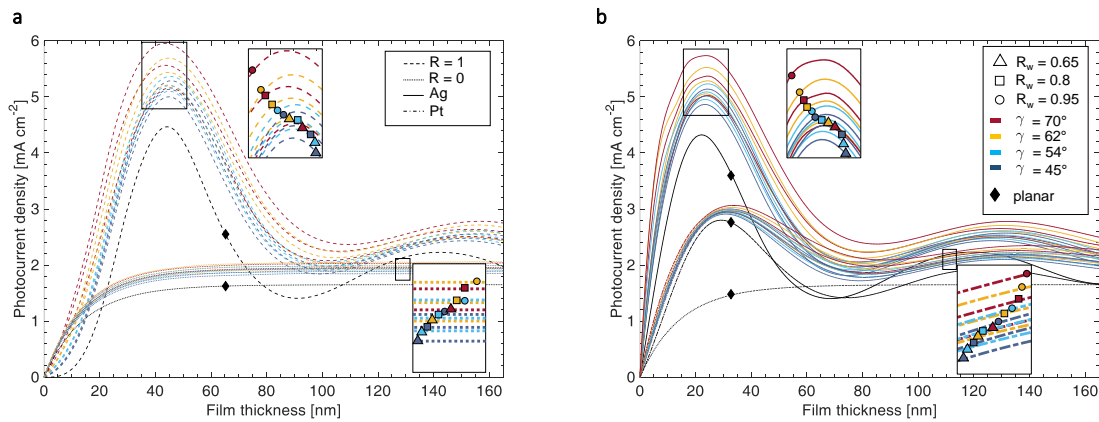


Figure 5.8 Photocurrent densities for ideal forward-injection of minority carriers ($\Phi=1$, $P_F=1$). All photocurrent densities are normalized by the section width, d_{sc} . Planar and wedge structures on (a) transparent (dotted), perfect reflective (dashed), (b) Ag (solid), and Pt (dash-dot) current collectors. All close-up windows are not in scale.

Implementing Light Trapping on Thin Film, Mesostructured Fe₂O₃ Photoanodes

Applying the IQE to the photogeneration rate and integrating it over the film thickness, the photocurrent density, $i_{\text{photo}} = q \int_0^d \int_x g(x, y) dx \cdot IQE(y) dy$, is obtained and shown in Figure 5.8. The photocurrent density is normalized by the section width, $2d_{\text{sc}}$. The photons that are absorbed too far away from the electrolyte interface do not participate in the water-splitting reaction and do not contribute to the photocurrent density. Therefore, the photocurrent density for α -Fe₂O₃ on a planar, transparent substrate reaches a constant value for a film thickness greater than 85 nm. For α -Fe₂O₃ on reflective layers, the maximum predicted photocurrent density is substantially reduced from the predicted photogenerated current density (IQE=1) and shifted to thinner film thickness. The second peaks are even more suppressed and are not of interest for an efficient photoanode. For planar electrodes, the photocurrent density can be boosted through resonant light trapping by 172% when using a perfect reflective layer, by 163% with an Ag-, and by 70% with a Pt-coating. Applying geometric light trapping to those film stacks, the photocurrent density can be further increased with maximum values depending on the geometric parameters of the wedge microstructure. The observed trend from the previous section with better light absorption for steeper wedges and smaller gaps between wedges persists and translates to higher photocurrent densities.

In Figure 5.9, the dependency of the maximum photocurrent density is shown for the four substrate configuration as a function of the wedge angle, γ , and aspect ratio, R_w . The contour plots quantify the gain through geometric light trapping, compared to their planar configuration counterparts. For a transparent current collector, the effect of γ and R_w on the maximum achievable photocurrent density is almost identical. With $\gamma=70^\circ$ and $R_w=0.95$, an increase of 26% is predicted. By using a perfect reflective layer, the improvements for all geometric parameters are enhanced as the number of reflected photons are increased. Furthermore, by having an aspect ratio and angle above 0.75 and 60° , respectively, high gradients for the gain factor are found, with a maximum of 33% in the considered parameter range. α -Fe₂O₃ films on Ag substrates behave very similarly, and the same enhancements are predicted. The shape of the contour plots for Pt-coatings are between the transparent and the perfect reflective layer. Pt absorbs a substantial part of the photons, and thus, the retrapping of photons reflected at the semiconductor-electrolyte interface (like in the transparent configuration) and the photons reflected at the semiconductor-current collector interface (dominant in the configuration with a perfect reflective layer) contribute evenly to the geometric light trapping.

As shown in the previous section, the absorbed photon flux maps for α -Fe₂O₃ films on wedge structures are not homogeneous, and substantial variations in the photocurrent densities along the semiconductor-electrolyte interface are expected. From the results of Figure 5.6, the

Implementing Light Trapping on Thin Film, Mesostructured Fe₂O₃ Photoanodes

maximum could be twice as high as the minimum local photocurrent density. To benefit from the optical gain introduced by the geometric light trapping, the kinetics for the electrochemical reaction at the electrolyte interface need to be high enough. Even though the photocurrent density distribution for the planar electrodes is homogeneous, their values could still be higher compared to their structured counterparts. The surfaces roughness introduce by the wedge structure is between 1.2 and 2.8, as shown in Figure 5.10, which reduces the local photocurrent density.

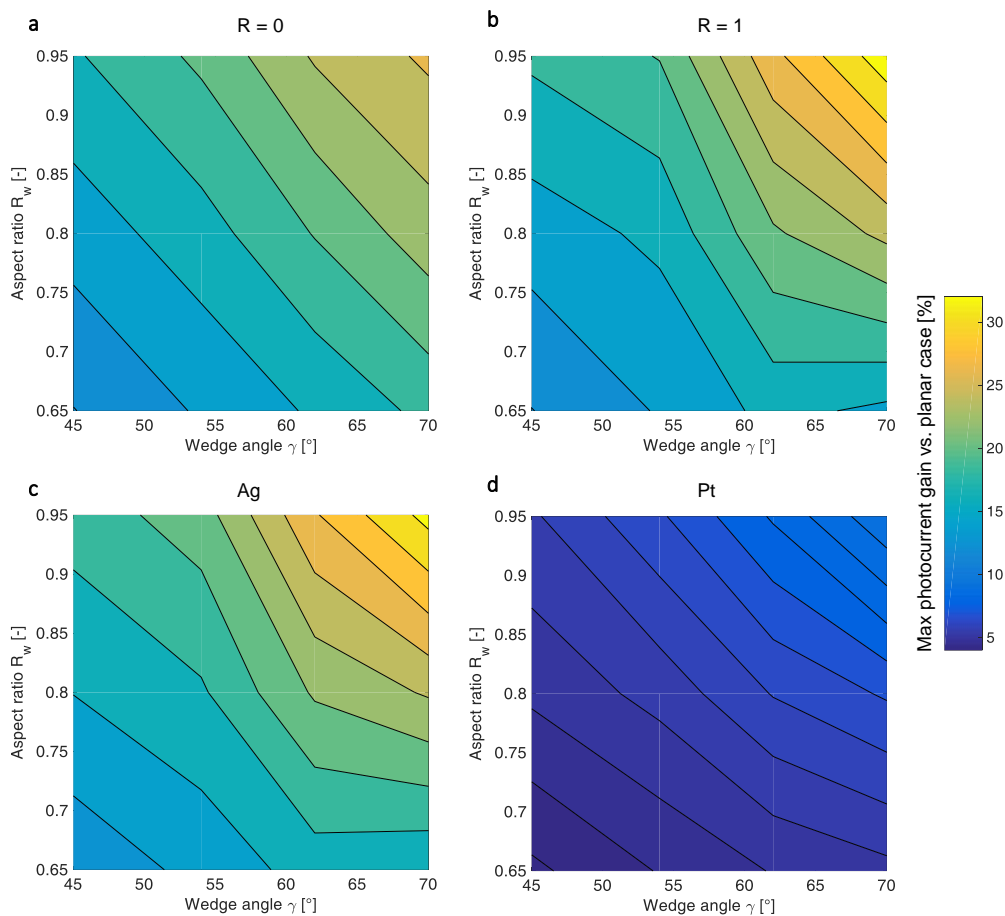


Figure 5.9 Gain of maximum photocurrent through geometric light trapping as a function of the wedge angle, γ , and aspect ratio, R_w . The gain is quantified for wedge structures with (a) transparent, (b) perfect reflective, (c) Ag, and (d) Pt layer compared to their planar configuration counterparts.

Implementing Light Trapping on Thin Film, Mesostructured Fe₂O₃ Photoanodes

If we consider a linear scaling of the surface recombination with the surface area due to surface states [31], the surface roughness should be kept low. Compared to the nanostructured α -Fe₂O₃ photoanodes, the proposed strategy with resonant and geometric light trapping in thin films on wedge structures is predicted to boost the photocurrent density without increasing the surface area substantially.

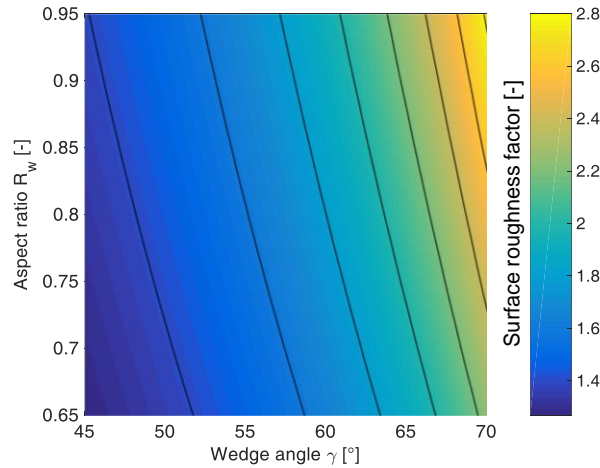


Figure 5.10 Surface roughness factor as a function of the wedge angle, γ , and aspect ratio, R_w . The surface roughness factor is defined as the surface area divided by the projected area (section width, $2d_{sc}$).

Light Incident Angle and Microstructure Dimensions

We now assess the potential of resonant and geometric light trapping for a photoelectrochemical water-splitting device with some more realistic operating conditions. The incoming angle of the solar irradiation (AM1.5G) was varied between 0° (normal incidence) and 80° . The following interfaces of an assembled electrochemical cell were considered: air-glass, glass-water, and water-semiconductor-current collector. The incoming power reduction, due to the reflectance, and the final incident angle after passing the glass were adapted by applying Fresnel's law. Experimentally verified parameters for the IQE probability model were taken from the literature ($\Phi=0.74$, $P_F=0.95$, $P_B=1$, and $L=20$ nm) [13]. The α -Fe₂O₃ film thickness was set at 25 nm and Ag was considered as a reflective current collector. Figure 5.11a quantifies the predicted photocurrent density for a planar, and two wedge structures with $\gamma=54.7^\circ$, $R_w=0.8$ and $\gamma=70^\circ$, $R_w=0.95$. For a

normal incoming light angle, the photocurrent densities of the three configurations are reduced to 46% of their values without an air-glass and glass-water interface under ideal forward-injection conditions (Figure 5.8b). Varying the angle of the incoming light reduces the photocurrent density for all three configurations due to increased reflectance and reduced view factors. The wedge structure with $\gamma=54.7^\circ$, $R_w=0.8$, shows an 18% increased photocurrent density for a normal incoming light angle and the gain reduces to a minimum of 6% at an angle of around 54° before it increases again. At the minimum around 54° , no geometric light trapping is possible as the light hits the wedge slope perpendicularly. The wedge structure with $\gamma=54.7^\circ$, $R_w=0.8$ exhibits an increase of 33% at normal incidence, a maximum of 36% at 10° , and a slow decrease to 29%, before the current density increases again. These results demonstrate that geometric light trapping has a great potential to increase the photocurrent in a practical water-splitting device.

Figure 5.11b assesses the effect of the wedge dimensions on the overall photocurrent density. In the previous sections, the section width, $2d_{SC}$, was set at $3\ \mu\text{m}$. Now, wedge structures with a section width of $1\ \mu\text{m}$ and $5\ \mu\text{m}$ are calculated. As in the previous calculations, the results of the TE and TM wave were averaged to the final value (IX). There is a slight reduction (<5%) in photocurrent for the wedge structure with $\gamma=54.7^\circ$, $R_w=0.8$, when the wedge dimension is decreased. The origin of this behavior is ambiguous. Resonant effects on the wedge tip for specific wedge dimensions might play a role. The photocurrent density is independent of the dimensions of the wedge structure with steep slopes and high aspect ratios ($\gamma=70^\circ$, $R_w=0.95$).

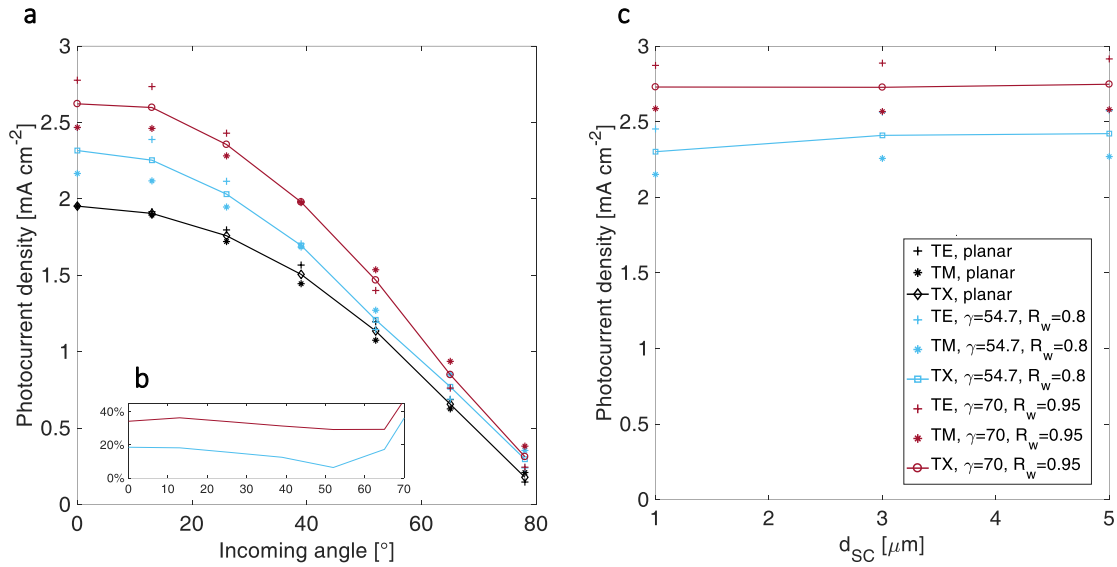


Figure 5.11 (a) Photocurrent density for different incoming light angles, taking into account the reduction of the incoming power and the change of incident angle through the air-glass and glass-water interfaces. Parameters for the IQE probability model are ($\Phi=0.74$, $P_F=0.95$, $P_B=1$, and $L=20$ nm). The results for a planar and two wedge structures on an Ag current collector are compared to a 25nm thick α -Fe₂O₃ film. (b) The relative improvement in the photocurrent compared to the planar configuration. (c) Photocurrent densities for different wedge dimensions.

5.3 Fabrication of Patterned, Thin Film Photoanode through Template-Stripping

In order to achieve resonant light trapping in a thin film photoelectrode, a uniform semiconductor layer with smooth interfaces is required. To further enhance the light absorption through geometric light trapping, vast arrays of wedges or pyramids need to be fabricated with high precision and reliability. Anisotropic etching of silicon in KOH meets both requirements, with a smooth etching profile along the (111) crystallographic planes. Based on our numerical predictions, steep wedge slopes and small gaps between the wedges will lead to high photocurrent densities. The anisotropic etching in KOH results in wedges with slope angles of 54.7°. This etching method is favored over other fabrication processes (e.g., reactive ion etching) that could lead to steeper wedges, but only with a compromise on the surface smoothness. A substantial efficiency boost is expected from resonant and geometric light trapping. However, the required photolithography process to fabricate the etching mask is time-consuming and relatively expensive for a projected large-scale photoelectrode production. It is also not resourceful to use the highly crystalline silicon wafer simply as a mechanical support. The patterned silicon wafer is rather used as a master template to transfer the microstructure onto a cheaper substrate. Subsequently, we propose two process flows and demonstrate how patterned, thin film water splitting electrodes can be fabricated using template-stripping methods.

5.3.1 Process Flow

Master Template

Direct laser lithography and dry etching are used to create a mask layout with a SiO₂ layer on a silicon wafer. Subsequent wet etching in KOH converts the SiO₂ mask layout into 3D structures. Series of parallel bands translate into wedges, whereas arrays of squares lead to inverse pyramids in the wafer. The angles of the wedge/pyramid facets are 54.7°, and the depths of the structures are controlled by the dimensions of the SiO₂ mask openings. The patterned silicon wafer is the master template that can be reused multiple times in the process flows A] and B].

Process Flow A]: “Strip then Deposit”

Polyimide is directly dispensed onto the master template and cured at 300° C. By using spin-coating for the polyimide film dispersion, the wedge/pyramid cavities are filled, and the top of the layer is flat. The adhesion between silicon and polyimide is low enough to strip the two layers by peeling. The silicon template can be cleaned in an oxygen plasma to remove any residuals of the polyimide before reusing it. The patterned polyimide is then used as a substrate to deposit a

Implementing Light Trapping on Thin Film, Mesostructured Fe₂O₃ Photoanodes

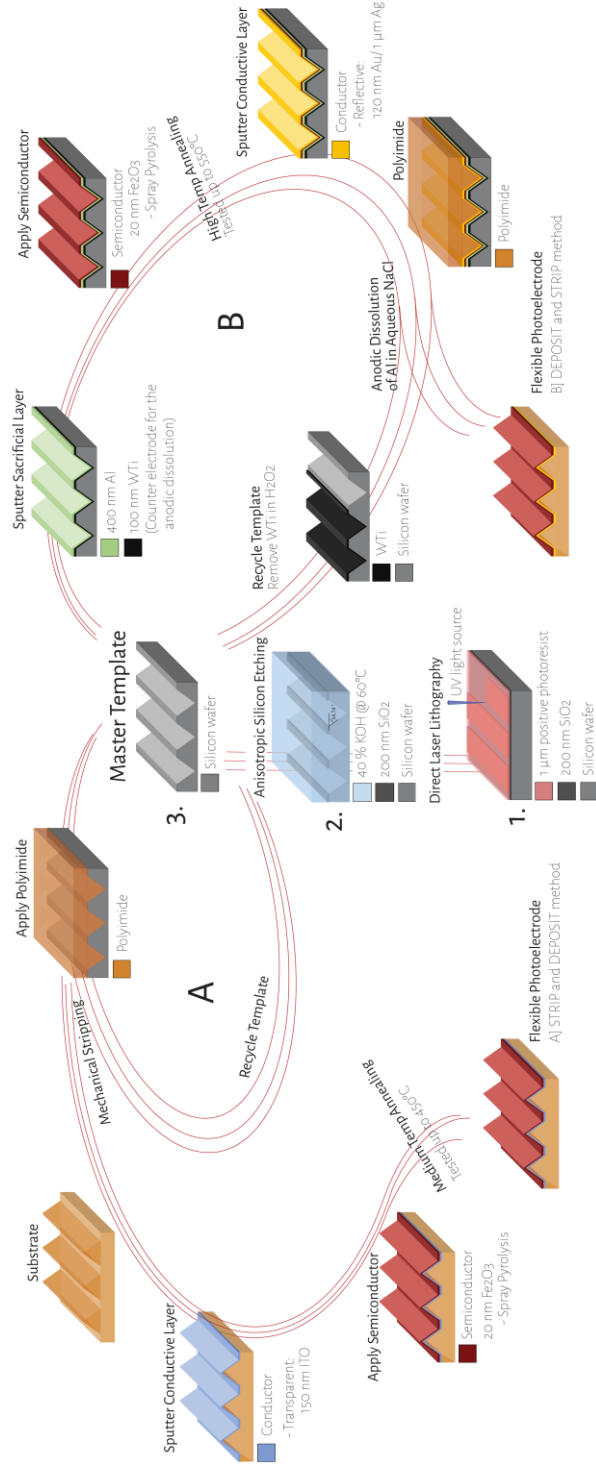


Figure 5.12 Master Template: Direct laser lithography and dry etching are used to create a mask layout with a SiO₂ layer on a silicon wafer. Subsequent wet etching in KOH converts the SiO₂ mask layout into 3D wedge structures. *Process Flow A* “Strip then Deposit”: Polyimide is applied, cured and stripped by peeling. The patterned polyimide is then used as a substrate to deposit a transparent or reflective, conductive layer, followed by the deposition and annealing of the desired semiconductor. *Process Flow B* “Deposit then Strip”: Depositing WTi and the sacrificial Al layer, followed by the electrode stack in reverse order, starting with the semiconductor film. This approach allows higher annealing temperatures. Subsequently, a transparent or reflective conductive layer is deposited, followed by a backing layer. The photoelectrode is stripped from the silicon template by anodic dissolution of the Al in 2 M NaCl solution. For both process flows, the silicon master template can be reused.

transparent or reflective, conductive layer. The last step is the deposition and annealing of the desired semiconductor for light absorption and water splitting.

Process Flow B]: “*Deposit then Strip*”

A thin layer of W:Ti(10%) is deposited onto the silicon template, followed by an Al layer. The WTi serves as a counter electrode in the stripping process, whereas the Al is the sacrificial layer that will be dissolved. In this process flow, the layers of the photoelectrode are deposited in the reversed order, starting with the semiconductor film. This approach allows higher annealing temperatures for the semiconductor film, as the material properties of the current collector and backing layer do not have to be considered. Temperature limitations due to the diffusion of metals or outgassing of the backing layer are avoided. Subsequently, a transparent or reflective conductive layer is deposited, followed by a backing layer. The photoelectrode is stripped from the silicon template by anodic dissolution of the Al in 2 M NaCl solution. A positive potential is applied to the WTi layer, with a grounded Pt electrode in the same electrolyte bath. The photoelectrode is released with the semiconductor as the top layer. The WTi on the silicon wafer is removed with hydrogen peroxide, and the master template can be reused.

5.3.2 Choice of Materials

Silicon wafers were used as a master template substrate as a variety of precise and mature patterning technologies exist to create microstructures with controllable size and shapes [32]. Silicon wafers can also withstand high temperatures, withstand sputtering of metals, and they are chemically stable during the anodic dissolution in an aqueous environment.

Polyimide PI2611 was chosen as a backing layer due to several reasons. The low viscosity of the polyimide before the soft-bake ensures that the microstructure cavities in the template were filled. With a cured film thickness of maximum 9 μm, two deposition layers were sufficient to fabricate a polyimide substrate that could be handled easily after the release process. The polyimide microstructures withstood sputtering, and the anodic dissolution and the electrochemical characterization in an aqueous environment. The maximum processing temperature is given by the curing temperature (300° C) [33], but we tested the polyimide up to 450° C without seeing any bubble formation due to outgassing. Polyimide also has a high light transmittance for wavelengths above 420 nm, making it suitable as a substrate for transparent photoelectrodes in a tandem cell setup [34]. In addition, it is a flexible, low-stress material with a high modulus of elasticity [32], opening the way for new concepts of macroscopic light trapping and tracking of the sun in photoelectrochemical water splitting devices.

Implementing Light Trapping on Thin Film, Mesostructured Fe₂O₃ Photoanodes

The conductive layer is either reflective to enhance light absorption or transparent in case of a tandem photoelectrode setup. Photoelectrodes with a transparent current collector do not benefit from resonant light trapping in the semiconductor film, but will still have a gain in light absorption through the geometric light trapping of the microstructure. Indium tin oxide (ITO) was used as a transparent, and silver as a reflective current collector. The conductive layer will be exposed to the alkaline electrolyte in case of pinholes in the semiconductor layer. ITO is stable in the potential range relevant for water oxidation [35], but Ag is corrosive in this environment [13]. Moreover, the Ag layer has shown to be sensitive to high temperatures, as thermal etching and diffusion of Ag at substrate temperatures of around 450° C reduced the reflectivity substantially [13]. The electrochemical corrosion, as well as the thermal etching, can be reduced by co-sputtering gold together with silver (Ag:90%, Au:10%), and the diffusion of Ag can be limited by having Ag in a sandwich of thin TiN layers [13]. With our equipment, co-sputtering was not possible; therefore, we deposited the multilayers: TiN/Au/Ag/TiN. The assumption was, that at temperatures of 300° C, during the polyimide curing, Au would diffuse into the Ag. For the process flow B), the same multilayer scheme was used, but the maximum process temperature for the current collector was reduced from 450° C to 300° C (polyimide curing).

Iron oxide, deposited by ultrasonic spray pyrolysis (USP), was chosen as the semiconductor layer. Thin photoactive films of a few nanometers have been successfully demonstrated using this method [11]. In order to reduce the backward-injection loss at the semiconductor-current collector interface, a SnO₂ underlayer was introduced.

5.3.3 Experimental Methods

Template Fabrication

4-inch silicon (100) wafers were patterned by anisotropic wet etching after a photolithography process. First, 200nm SiO₂ were grown by wet oxidation (Centrotherm furnace) and coated with 1µm positive photoresist (MicroChemicals, AZ ECI 3007). The thickness of the resist was determined after a series of experiments. A thinner resist thickness allows for a higher resolution in the photolithography process, but if the layer is too thin, it cannot resist the dry etching of the SiO₂. The microstructure layout was directly written onto the photoresist with a UV-light source ($\lambda=405$ nm, Dose=130 mJ/cm², Defocus=0), using a maskless exposure tool (Heidelberg Instruments, MLA150). 16 template layouts were written onto the wafer, with each layout consisting of a 1cm² unexposed flat area joint with a 1 cm² exposed patterned area. In the case of the wedge structures, bands of width equal to $2L_p$ were exposed. The gap between the bands was

Implementing Light Trapping on Thin Film, Mesostuctured Fe₂O₃ Photoanodes

equal to $2L_g$. In the case of the pyramid structures, squares with side edges equal to $2L_p$ and gaps of $2L_g$ were exposed. With the highest laser resolution, the smallest dimensions achievable were $L_p=L_g=0.5\ \mu\text{m}$. The layouts were designed by using the software *L-Edit*.

After developing the photoresist, the photoresist mask was used to etch the underlying SiO₂ in a dry etcher using fluorine chemistry (SPTS APS Dielectric Etcher, Etching time=50 s). The etch ratio for SiO₂ to photoresist was 3:1. The remaining photoresist was removed in an oxygen plasma. The SiO₂ patterns acted as a mask for the subsequent wet etching of the silicon. In potassium hydroxide (KOH) solution, the silicon etching rate depends on crystallographic planes, with the (100) planes etching 200 times faster than the (111) planes. The anisotropic etching is self-terminating when all (111) planes are exposed. The angle between the two crystallographic planes is 54.7° [32]. The etching was done in 40% KOH at 60°C , followed by a 2 h neutralization step in a 37% HCl bath. The SiO₂ mask was removed in buffered hydrofluoric acid (NH₄F 40% + HF 50%, ration 7:1).

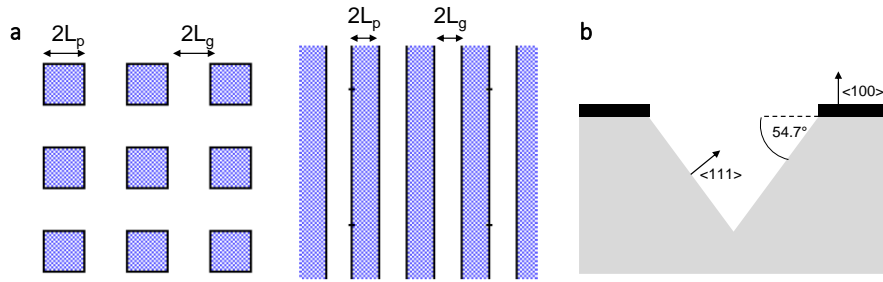


Figure 5.13 (a) Photolithography template layouts for inverse pyramids (left) and wedges (right). (b) Anisotropic silicon etching in KOH. The SiO₂ mask is shown in black.

Multilayer Deposition

Sacrificial layer: For the process flow B], a sacrificial layer for the subsequent release process was deposited. First, a 100 nm thick W:Ti(10%) was sputtered onto the silicon master template. This layer will serve as a counter electrode during the anodic dissolution process. The sacrificial layer was a 400 nm thick Al layer deposited by a DC magnetron sputtering system (Alliance-Concept, DP650). Process flow A] did not need a sacrificial layer, as the adhesion between Si and polyimide is low enough to separate the materials manually.

Implementing Light Trapping on Thin Film, Mesostructured Fe₂O₃ Photoanodes

Semiconductor: Three deposition methods for hematite have been applied. (i) Ultrasonic spray pyrolysis of Fe(acac)₃ solution, (ii) atomic layer deposition using ferrocene and ozone, and (iii) pulsed laser deposition from a Ti-doped iron oxide target.

(i) Ultrasonic spray pyrolysis (USP):

10mM Fe(acac)₃ solution was sprayed through an ultrasonic spray nozzle. The fine mist was deposited on the sample at a surface temperature of 450 °C (10 mM Fe(acac)₃ (99.9%) solution; 1 ml every 30 s, 15m l) to create iron oxide. The growth rate was approximately 1.5 nm/ml, and a hematite thickness of approximately 20 nm was deposited. After the deposition was complete, the samples were held at 450 °C for 1 min before cooling down to room temperature.

(ii) Atomic Layer Deposition (ALD):

Fe(Cp)₂ was heated to 80° C and exposed alternating to Ozone [36]. The conditions in the ALD chamber included a pressure of around 0.5 mbar and a N₂ flow of 20 sccm. The following sequence was used: [Fe(Cp)₂-Pulse/Exposure/Purge/O₃-Pulse/Exposure/Purge], with pulse times of 0.02 s (Fe(Cp)₂) and 0.01 s (Ozone). The substrate holder was kept at 230° C and the cycle duration was 180 s. 300 cycles resulted in α-Fe₂O₃ film of around 20 nm thickness [12].

(iii) Pulsed Laser Deposition (PLD):

α-Fe₂O₃ films were deposited with a KrF excimer laser from a Ti-doped Fe₂O₃ target. The laser fluence was at 1 J/cm² with a repetition rate of 5 Hz. The substrate was at a distance of 70 mm. The heater setpoint was at 600° C, corresponding to a substrate temperature of 450° C. The chamber pressure was under an oxygen flow of 30 mTorr. 2000 laser pulses are needed for a 20 nm thick α-Fe₂O₃ film [13].

Underlayer: Between the semiconductor and current collector, an underlayer was deposited to reduce the injection of holes into the conductive layer. In combination with the hematite deposition (USP and ALD), SnO₂ was deposited at 118° C by ALD, using Tetrakis(dimethylamino)tin(IV) and ozone. In combination with the PLD of hematite, two layers of SnO₂ were deposited. First, a high-temperature undoped SnO₂ film (deposited by PLD using 250 laser pulses, at a setpoint temperature of 500° C and under oxygen flow at a pressure of 55 mTorr). Second, a low-temperature undoped SnO₂ film (deposited by PLD using 100 laser pulses, at a setpoint temperature of 300° C and under oxygen flow at a pressure of 25 mTorr).

Implementing Light Trapping on Thin Film, Mesostructured Fe₂O₃ Photoanodes

Current collector/Reflector: For the process flow A], 150 nm of indium tin oxide (ITO; In₂O₃:90%, SnO₂:10%) was sputtered (Pfeiffer, Spider 600) as a transparent current collector. For the process flow B], silver was chosen as a current collector and reflective layer. To increase the chemical stability of silver in case of exposure to the electrolyte, we deposited first a thin layer of gold, which diffused into the silver layer at the curing temperature of the polyimide. The following materials were sputtered onto SnO₂ in this order: 1nm TiN, 120 nm Au, 1080 nm Ag, 10 nm Ti, 8 nm TiN and 10 nm Ti. TiN was applied as a diffusion barrier for gold and silver. Ti was used to improve adhesion between Ag and TiN, as well as TiN and polyimide.

Backing layer: The polyimide PI2611 (MicroSystems) was used as a backing layer and substrate. For the process flow A], the polyimide is directly spin coated and cured on the silicon master template. For the process flow B], the backing layer is applied as the last layer before curing and the anodic dissolution. In both cases, the surface was dehydrated on a hotplate at 130° C for 3 min. 5-10 ml of the adhesion promotor VM-651 was applied. The product was given 30 s to react, then the spinner and the N₂ flow were turned on to dry the sample. Polyimide PI2611 was defrosted 1-hour before application in order to reach room temperature, which is an optimal viscosity condition. After another dehydration step at 130° C, approximately half of the sample surface was covered with polyimide. The avoidance of bubble formation is crucial, as discontinuities can reduce the uniformity of the layer. The spinner (Sawatec, LSM200) followed the subsequent profile:

S1: 5 s from 0 to 500 rpm

S2: 5 s at 500 rpm

S3: 10 s to 1500 rpm

S4: 40 s at 1500 rpm

S5: 1 s at 2500 rpm

S6: 1 s to 1500 rpm

S7: 5 s at 1500 rpm

S8: 15 s to 0 rpm

The spin coating process was repeated a second time, leading to two layers of polyimide, each approximately 9 μm thick.

A soft-bake at 65° C for 3 min and 130° C for another 3 min solidified the polyimide and simplified the sample handling. Hard-baking was done at 300° C under N₂ environment. The temperature profile of the oven (Heraeus, T6060) was:

Implementing Light Trapping on Thin Film, Mesostructured Fe₂O₃ Photoanodes

- S1: 50°C to 200° C in 40 min
- S2: at 200° C for 60 min
- S3: 200° C to 300° C in 25 min, N₂ flow on
- S4: at 300° C for 60 min, N₂ flow on
- S5: cool down

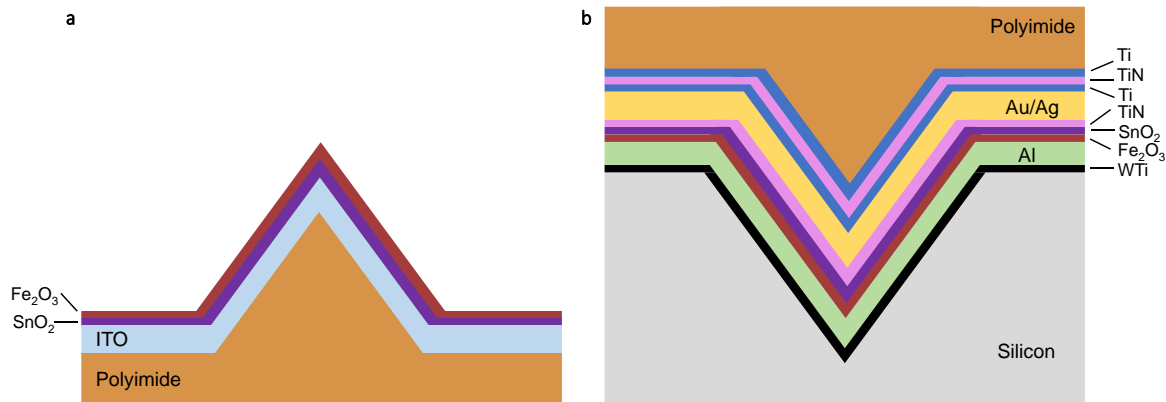


Figure 5.14 Multilayer stacks for (a) process flow A], and (b) process flow B].

Release Process

For the process flow A], the polyimide was mechanically released from the silicon wafer. The polyimide layer was cut with a razor blade along the circumference of the designed patterns and submerged in deionized water for 12 hours. The soaking in water helped to further reduce the adhesion, so then the patterned polyimide films could be peeled off the silicon wafer with a tweezer.

For the process flow B], the sacrificial Al layer was dissolved in 2 M NaCl solution. The polyimide was cut along three sides of the designed patterns. The polyimide and the layers underneath were scratch with a razor blade to access the W/Ti layer. Silver paste was used to ensure good electric conductivity between the W/Ti and a copper tape. The W/Ti was kept at 0.2 V, whereas the ground terminal of the voltage source was connected to a silicon wafer covered by 100 nm Pt. The Al was electrochemically etched, and the patterned electrodes were released. The electrodes were washed in deionized water.

The wafer template could be reused after cleaning in HCl for 15 min to remove NaCl residuals, followed by a 2-3 hour etching of the WTi in hydrogen peroxide.

Photoelectrochemical Characterization

The released electrodes from both process flows were placed on a glass slide and the edges were covered with epoxy. The hematite was scratch on the flat side of the electrode and the electric contact to the current collector was created using silver paste and copper tape. The area of the electric contact was then also covered by epoxy. All hematite surfaces, except the active area, were covered by a copper tape in an epoxy sandwich to guarantee that no light could penetrate through the epoxy. The photoelectrochemical characterization of the electrodes was done in a three-electrode configuration, with a Pt wire counter electrode and an Ag/AgCl (sat. KCl) reference electrode. The electrolyte was 1 M NaOH (pH 13.6) and the applied potential was converted to RHE. AM1.5G sunlight in the visible and near-infrared region (400-1100 nm, 76 mW cm⁻²) was simulated with the VeraSol-2 solar simulator from Oriel. The potential was swept at a scan rate of 10 mV s⁻¹ and the light was chopped at a frequency of 2 Hz.

5.3.4 Characterization of Fabricated Electrodes

A silicon wafer with wedge structures was used as a template to demonstrate the feasibility of the process flow A]. The layout for the pattern was designed with a wedge base of 2 μm (=2 L_w) and a gap between the wedges of 2 μm (=2 L_g). A transparent current collector, consisting of 150 nm ITO, was deposited, and the iron oxide film was approximately 20 nm thick. Figure 5.15a shows an SEM image of the uniform wedges at the edge of the patterned area. The wedges had a base length of 2.4 μm and a gap distance of 1.6 μm. Figure 5.15b shows the whole photoelectrode with the patterned active area (1 x 1 cm²) and the planar area (1 x 1 cm²) used to connect to the potentiostat. The electrode was later glued onto a glass slide to keep the active area flat. Figure 5.15a proves the successful transfer of the template microstructure to the polyimide substrate with high precision. The photoresist was slightly overexposed during the photolithography process, leading to a broader wedge base of 2.1 μm. The 150 nm thick ITO layer increased the wedge base further to 2.4 μm. The sputtering of the ITO onto the smooth polyimide surface formed a nanostructure, with clusters of around 100 nm diameter, comparable to morphologies observed in other applications of sputtered ITO [37]. Despite the rough surface, the transparent photoelectrode could still benefit from the geometric light trapping due to the wedge structures. The ultra-thin iron oxide film deposited by USP cannot be identified in the shown SEM image.

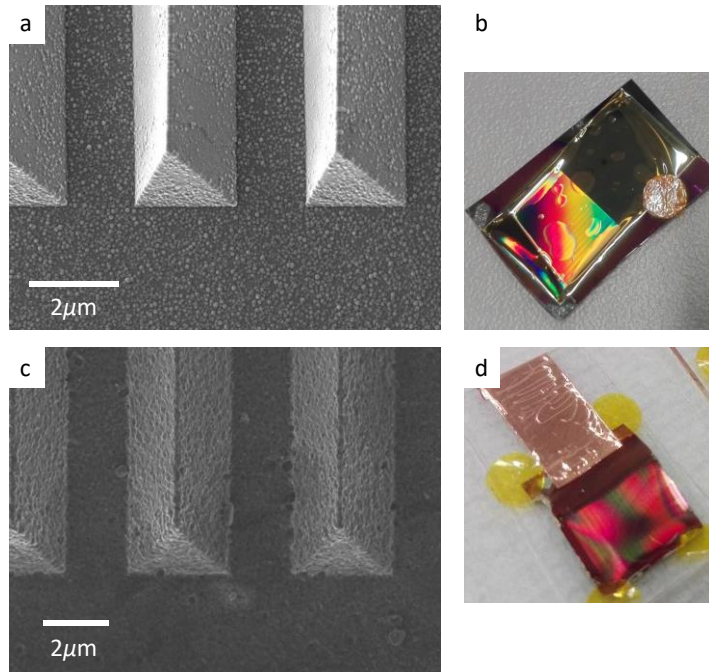


Figure 5.15 *Process Flow A*]: Wedge structure transferred to a polyimide layer and coated with an ITO, SnO₂ and a α -Fe₂O₃ film. (a) SEM images and (b) photograph. Size of electrode = 1 x 2 cm². *Process Flow B*]: Multilayer (α -Fe₂O₃/SnO₂/TiN/Au/Ag/Ti/TiN/Ti/Polyimide) deposited onto a wedge structure and released by anodic dissolution of Al. (c) SEM images and (d) photograph. Size of electrode = 1 x 1 cm².

The process flow B] was implemented using a template microstructure on the silicon wafer with a wedge base of 3 μ m and a gap between the wedges of 2 μ m. A reflective current collector was chosen with the following multilayer stack on top of the polyimide: Ti/TiN/Ti/Ag/Au/TiN. The iron oxide film was again approximately 20 nm thick. An SEM image of the photoelectrode after the release from the template by anodic dissolution is shown in Figure 5.15c. Once more, a large patterned area of 1 x 1 cm² was released, contacted with copper tape (Figure 5.15d), and later encapsulated with epoxy. Besides the same increase of 100 nm in the wedge base due to overexposure, the microstructure turned out as designed ($2 L_p=3.1 \mu$ m, $2 L_g=1.9 \mu$ m). The sputtering of the 100 nm thick WTi and 400 nm thick Al layers were uniform and did not distort the wedges. However, the morphology of the Al layer was directly transferred from the template to the final surface of the photoelectrode film. Figure 5.16 reveals the same surface structure on the template, as seen on the α -Fe₂O₃ in Figure 5.15c. Overall, we demonstrated the successful

Implementing Light Trapping on Thin Film, Mesostructured Fe₂O₃ Photoanodes

transfer of the microstructure to the multilayer electrode with a polyimide backing layer following the template-stripping process B]. The structure withstood the anodic dissolution of the Al layer and based on the red color of the electrode; the iron oxide layer remained intact.

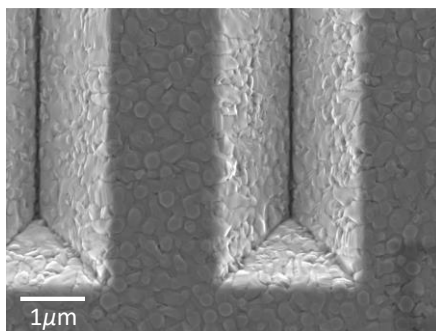


Figure 5.16 Silicon master template sputtered with 100 nm WTi and 400 nm Al.

Photoelectrodes fabricated via process flow A] with a transparent current collector, and via process flow B] with a reflective current collector were characterized regarding their photoelectrochemical response. Besides the microstructures with the previously quantified parameters, electrodes following the same process flow, but with a planar template wafer, were fabricated and tested. As a reference, iron oxide was deposited by USP on an FTO glass. Figure 5.17 shows the voltage-current curves under dark and illumination for the best performing electrode of each fabrication method vs. RHE. The reference photoelectrode has the best onset potential of all the electrodes at 1.1 V and reaches a plateau current density of 0.2 mA/cm² (at 1.6 V). Besides the shift in onset potential, the planar, transparent electrode (A] planar) has a comparable photocurrent plateau. The photocurrent plateau increases by around 30% when introducing the wedge microstructure. The planar, transparent electrode and the reference photoelectrode have the same light absorption, whereas the electrode with the microstructure can also absorb light that was initially reflected at the electrolyte-semiconductor interface. For the two electrodes fabricated by the process flow B], resonant and geometric light trapping was expected to lead to the highest plateau photocurrents. Indeed, the highest photocurrent was measured for the photoelectrode with a reflective current collector and a microstructure. However, the potentials needed to draw these currents are substantially higher than what is needed for the reference photoelectrode and close to the onset potentials of the dark currents. Shifts of the photocurrents to higher potentials, while keeping the same photocurrent plateau, can be

Implementing Light Trapping on Thin Film, Mesostructured Fe₂O₃ Photoanodes

correlated to an increase in surface states [11]. For both our process flows, the materials and morphologies of the substrate layer (ITO or Al) for the iron oxide deposition are different from the reference photoelectrode (FTO) and might influence the density of surface states. In addition, the anodic dissolution of Al in the process flow B] might also affect the semiconductor-electrolyte interface.

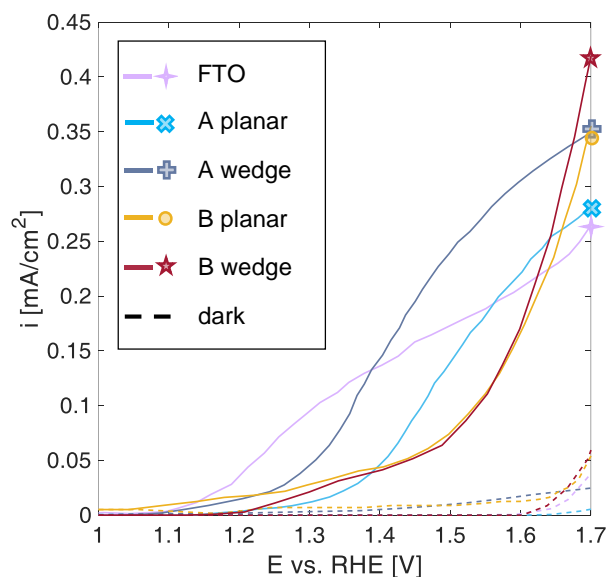


Figure 5.17 Photoelectrochemical characterization in 1M NaOH of fabricated electrodes under simulated AM1.5G irradiation. Planar (light blue) and microstructured (dark blue) electrodes fabricated according to process flow A] with a transparent current collector. Planar (yellow) and microstructured (red) electrodes fabricated according to process flow b] with a reflective current collector. α -Fe₂O₃ deposited on an FTO glass as a reference configuration.

Overall, planar and microstructured thin film α -Fe₂O₃ photoanodes demonstrated photoactivity and were fabricated according to the two proposed process flows. Improvement in the maximum photocurrent for the microstructure electrodes compared to their planar counterparts were seen; however, high onset potentials were observed and it is difficult to confirm systematic improvements based on resonant and geometric light trapping. The main concerns are the surface roughness and the inhomogeneity of the α -Fe₂O₃ films deposited by USP. Also, for our reference configuration with α -Fe₂O₃ on an FTO glass, the measured photocurrent density is much smaller with a larger onset potential compared to reported results in the literature [11]. Figure 5.18a shows

a photograph of the silicon master template after the USP deposition. The inhomogeneity of the α -Fe₂O₃ film can be seen by eye and the SEM image of the microstructure (Figure 5.18b) also indicates material density variations.

5.3.5 Improvements

The numerical calculations on resonant and geometric light trapping predicted a substantial enhancement of the photocurrent densities and the two newly proposed process flows were successful in fabricating highly ordered, microstructured α -Fe₂O₃ film that showed photoactivity. The main issue that prevented the demonstration of efficient photoanodes seemed to be the inhomogeneity of the USP deposited α -Fe₂O₃ film. Moreover, it is not clear if all of the deposited hematite is photoactive.

In order to fabricate much more uniform α -Fe₂O₃ films, atomic layer deposition was employed. Following a reported recipe from the literature [36], α -Fe₂O₃ films were deposited from ferrocene and ozone in an ALD chamber at 230°C. The fabrication according to the process flow B] was used. Also, a few nanometer thick Al₂O₃ was deposited between the Al and the Fe₂O₃ films. This film protected the hematite during the anodic dissolution and was later dissolved in 1M NaOH. Figure 5.18b demonstrates a photograph of the template wafer right after the ALD deposition. Ellipsometry measurements confirmed a layer thickness of 20 nm. Figure 5.18d exhibits an SEM image of a homogeneously covered pyramid array after stripping the electrode by anodic dissolution. Unfortunately, the Fe₂O₃ films of the photoanodes were not photoactive. Furthermore, reference depositions on FTO did not show any photoresponse. The failure of the ALD deposition was due to a dysfunctioning ozone generator.

Another experimental campaign was started with Ti-doped Fe₂O₃ films deposited by PLD. This method has been proven to fabricate thin and homogeneous films that allow for resonant light trapping [13]. Preliminary results of the fabrication process following the process flow B] are promising. Intact multilayers could be released from the template silicon wafer for photoelectrodes with an Ag or a Pt reflective layer.

Implementing Light Trapping on Thin Film, Mesostructured Fe₂O₃ Photoanodes

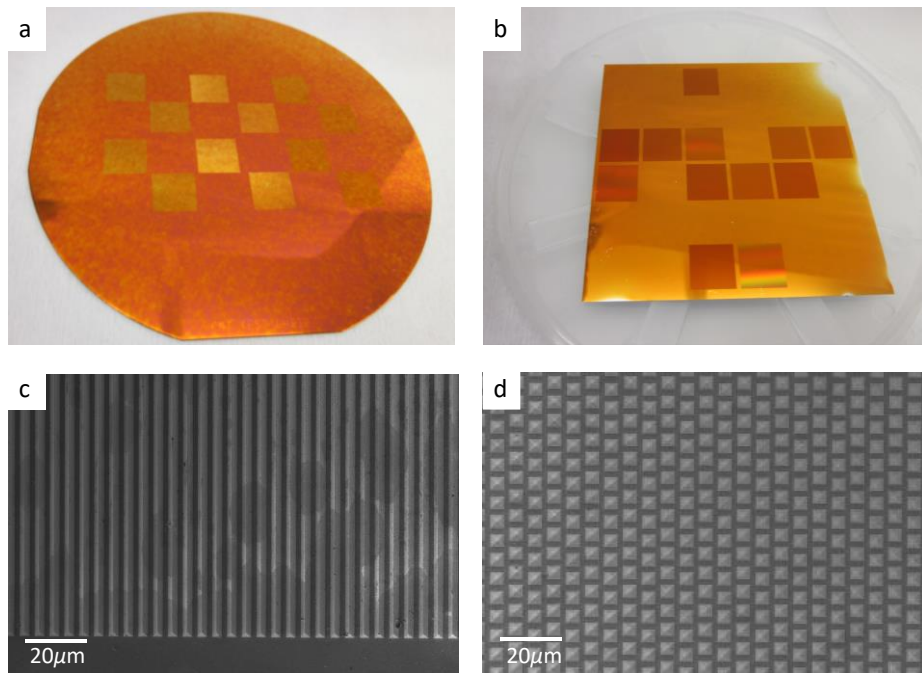


Figure 5.18 Photographs of the silicon template wafer after the deposition of Fe₂O₃ by (a) USP and (b) ALD. SEM images of the stripped microstructure following the process flow B] for Fe₂O₃ deposited by (c) USP and (d) ALD.

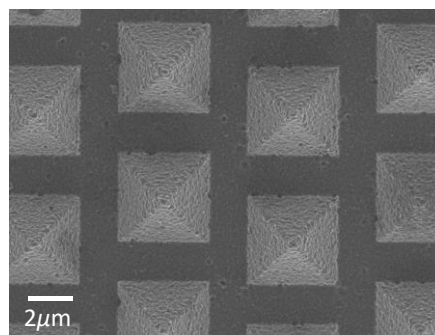


Figure 5.19 Detailed view on a stripped array of micro-pyramids following the process flow B] for Fe₂O₃ deposited by ALD.

5.4 Conclusions

We demonstrated that a combination of resonant and geometric light trapping could substantially enhance the light absorption and boost the photocurrent density. The microstructures suitable for these light trapping schemes were successfully fabricated using a template-stripping method. Electromagnetic wave propagation simulations of planar α -Fe₂O₃ films on reflective current collectors were used to validate our 2D finite element model. For normal incident light, resonance modes were predicted, and the optimum α -Fe₂O₃ film thicknesses for a maximum light absorption on a perfect reflective, an Ag and a Pt substrate were determined. The same multilayer stacks applied to wedge structures also exhibited a periodic dependency of the absorbed photon flux on the α -Fe₂O₃ film thickness. The peaks of local maximum light absorption were broader and shifted to higher thicknesses, losing the stringent requirements to fabricate highly uniform α -Fe₂O₃ films with a thickness tolerance of a few nanometers. Geometric light trapping, through the harvest of reflected photons on the flat section between the wedges or the opposite wedge slope, enhanced the maximum absorbed photon flux considerably. For a microstructure with a wedge angle of $\gamma=54^\circ$, and an aspect ratio of $R_w=0.8$, the gain through geometric light trapping on an electrode with a transparent current collector was in the range of 15-18%, compared to a transparent and planar reference configuration. In comparison to the same reference, the first resonance peak for microstructures with a perfect reflective or an Ag layer was increased, due to a combination of resonant and geometric light trapping, by 159% or 220%, respectively. Retrapping of photons were responsible for an increase of 58% or 73%, respectively. Varying the geometric parameters of the wedges, namely the wedge angle, γ , and the aspect ratio, R_w , had a direct effect on the overall light trapping efficiency. Steep wedge slopes with a minimal gap between wedges were found to produce the most significant enhancement. Taking into account the short charge carrier collection length in α -Fe₂O₃ by an empirical probability model for the internal quantum efficiency, photocurrent densities at the semiconductor-electrolyte interface were predicted. Under the ideal forward-injection condition, maximum photocurrent densities, normalized by the projected area, of 2.0, 6.0, 5.7, and 3.1 mA/cm² were predicted for microstructured and transparent, perfect reflective, Ag, or Pt current collectors, respectively. Considering an α -Fe₂O₃ film on a transparent substrate in a tandem photoelectrochemical water-splitting device, micro-structuring and, consequently, geometric light trapping can boost the photocurrent density by 24%. Ag was found to enhance both resonant and geometric light trapping, and behaviors similar to photoelectrodes with a perfect reflective layer were predicted. Pt, on the other hand, is not suitable for resonant light trapping due to its low reflectivity.

Implementing Light Trapping on Thin Film, Mesostructured Fe₂O₃ Photoanodes

We designed process flows to fabricate the proposed thin film α -Fe₂O₃ photoanodes on microstructured transparent or reflective current collectors. For the micro-patterning, anisotropic etching of silicon in KOH solution was chosen, due to the excellent control over the feature sizes, the high reproducibility rate, as well as the smooth etching surfaces along the crystallographic planes of silicon. The patterned silicon wafers were then used as a master template to fabricate α -Fe₂O₃ photoanodes on a flexible substrate. The first process flow is called “strip then deposit”, where the micro-pattern is transferred to a polyimide film, followed by the deposition of the current collector and the semiconductor. The second process flow is called “deposit then strip”, and the layers are deposited in reverse order and stripped in the end. For the latter approach, the deposition and annealing temperatures of the α -Fe₂O₃ could be much higher, as the temperature sensitive reflective layer and substrate layer were added in a later process step. We successfully demonstrated the fabrication of intact and photoactive photoanodes for both proposed process flows. Improved photocurrents were measured for the microstructured electrodes with transparent and reflective current collectors compared to their planar counterparts. However, the substantial potential in photocurrent gain predicted by the numerical model was not achieved. The main concerns were the homogeneity and photoactivity of the deposited α -Fe₂O₃ films. More controllable deposition methods (e.g., pulsed laser deposition) need to be explored to achieve homogeneous and reproducible thin α -Fe₂O₃ films, before the photocurrent gains from resonant and geometric light trapping in our photoanodes can be systematically evaluated.

We provided design guidelines for thin film α -Fe₂O₃ photoanodes on wedge structures to optimize the light absorption in order to maximize the photocurrent density. Fabrication methods for such photoanodes were proposed, and their feasibility demonstrated. The process flows based on template-stripping from a silicon master opens up the way for the fabrication of a wide range of microstructures. Numerous wet and dry etching processes exist to pattern silicon wafers. Wedges or pyramids with steep slopes and small distances between them can certainly be achieved, and photocurrent densities close to the numerically predicted values should be possible. Lastly, the strategy of a combined resonant and geometric light trapping is not only valid for α -Fe₂O₃, but can also be applied to other materials, such as BiVO₄ or Cu₂O.

5.5 References

- [1] D. Bae, B. Seger, O. Hansen, P. C. K. Vesborg, and I. Chorkendorff, “Durability Testing of Photoelectrochemical Hydrogen Production under Day/Night Light Cycled Conditions,” *ChemElectroChem*, pp. 106–109, 2018.
- [2] K. Sivula, F. Le Formal, and M. Grätzel, “Solar water splitting: progress using hematite (α -Fe₂O₃) photoelectrodes,” *ChemSusChem*, vol. 4, no. 4, pp. 432–49, Apr. 2011.
- [3] Z. Chen *et al.*, “Accelerating materials development for photoelectrochemical hydrogen production: Standards for methods, definitions, and reporting protocols,” *J. Mater. Res.*, vol. 25, no. 01, pp. 3–16, Jan. 2011.
- [4] R. Van De Krol, Y. Liang, and J. Schoonman, “Solar hydrogen production with nanostructured metal oxides,” *J. Mater. Chem.*, vol. 18, no. 20, pp. 2311–2320, 2008.
- [5] A. G. Tamirat, J. Rick, A. A. Dubale, W.-N. Su, and B.-J. Hwang, “Using hematite for photoelectrochemical water splitting: a review of current progress and challenges,” *Nanoscale Horiz.*, vol. 1, no. 4, pp. 243–267, 2016.
- [6] A. Kay, I. Cesar, and M. Grätzel, “New benchmark for water photooxidation by nanostructured α -Fe₂O₃ films,” *J. Am. Chem. Soc.*, vol. 128, no. 49, pp. 15714–21, 2006.
- [7] S. D. Tilley, M. Cornuz, K. Sivula, and M. Grätzel, “Light-Induced Water Splitting with Hematite: Improved Nanostructure and Iridium Oxide Catalysis,” *Angew. Chemie*, vol. 122, no. 36, pp. 6549–6552, Aug. 2010.
- [8] J. H. Kennedy, “Photooxidation of Water at α -Fe₂O₃ Electrodes,” *J. Electrochem. Soc.*, vol. 125, no. 5, p. 709, 1978.
- [9] Y. Ling, G. Wang, D. A. Wheeler, J. Z. Zhang, and Y. Li, “Sn-doped hematite nanostructures for photoelectrochemical water splitting,” *Nano Lett.*, vol. 11, no. 5, pp. 2119–2125, 2011.
- [10] S. C. Warren *et al.*, “Identifying champion nanostructures for solar water-splitting,” *Nat. Mater.*, vol. 12, no. 9, pp. 842–9, 2013.
- [11] L. Steier *et al.*, “Understanding the role of underlayers and overlayers in thin film hematite photoanodes,” *Adv. Funct. Mater.*, vol. 24, no. 48, pp. 7681–7688, 2014.
- [12] L. Steier, J. Luo, M. Schreier, M. T. Mayer, T. Sajavaara, and M. Grätzel, “Low-Temperature Atomic Layer Deposition of Crystalline and Photoactive Ultrathin Hematite Films for Solar Water Splitting,” *ACS Nano*, vol. 9, no. 12, pp. 11775–11783, 2015.
- [13] H. Dotan *et al.*, “Resonant light trapping in ultrathin films for water splitting,” *Nat. Mater.*, vol. 12, no. 2, pp. 158–64, 2012.

- [14] D. Danaei, R. Saeidi, and A. Dabirian, “Light trapping in hematite-coated transparent particles for solar fuel generation,” *RSC Adv.*, vol. 5, no. 16, pp. 11946–11951, 2015.
- [15] B. Eftekharinia, A. Moshaii, and A. Dabiriana, “Design rules of nanostructured transparent conductive electrodes for light trapping in hematite photoanodes,” *J. Photonics Energy*, vol. 7, no. 3, 2017.
- [16] K. X. Wang, Z. Yu, V. Liu, M. L. Brongersma, T. F. Jaramillo, and S. Fan, “Nearly Total Solar Absorption in Ultrathin Nanostructured Iron Oxide for Efficient Photoelectrochemical Water Splitting,” *ACS Photonics*, vol. 1, no. 3, pp. 235–240, 2014.
- [17] P. Campbell and M. A. Green, “Light trapping properties of pyramidally textured surfaces,” *J. Appl. Phys.*, vol. 62, no. 1, pp. 243–249, 1987.
- [18] J. D. Hylton, A. R. Burgers, and W. C. Sinke, “Alkaline Etching for Reflectance Reduction in Multicrystalline Silicon Solar Cells,” *J. Electrochem. Soc.*, vol. 151, no. 6, p. G408, 2004.
- [19] H. Park, S. Kwon, J. S. Lee, H. J. Lim, S. Yoon, and D. Kim, “Improvement on surface texturing of single crystalline silicon for solar cells by saw-damage etching using an acidic solution,” *Sol. Energy Mater. Sol. Cells*, vol. 93, no. 10, pp. 1773–1778, 2009.
- [20] A. Kay *et al.*, “Film Flip and Transfer Process to Enhance Light Harvesting in Ultrathin Absorber Films on Specular Back-Reflectors,” *Adv. Mater.*, vol. 30, no. 35, pp. 1–7, 2018.
- [21] J. H. Park, P. Nagpal, K. M. McPeak, N. C. Lindquist, S. H. Oh, and D. J. Norris, “Fabrication of smooth patterned structures of refractory metals, semiconductors, and oxides via template stripping,” *ACS Appl. Mater. Interfaces*, vol. 5, no. 19, pp. 9701–9708, 2013.
- [22] D. Yoo, T. W. Johnson, S. Cherukulappurath, D. J. Norris, and S. H. Oh, “Template-Stripped Tunable Plasmonic Devices on Stretchable and Rollable Substrates,” *ACS Nano*, vol. 9, no. 11, pp. 10647–10654, 2015.
- [23] D. M. Pozar, *Microwave engineering*, 4th editio. Hoboken: Wiley & Sons, 2011.
- [24] M. Hotta, M. Hayashi, M. T. Lanagan, D. K. Agrawal, and K. Nagata, “Complex Permittivity of Graphite, Carbon Black and Coal Powders in the Ranges of X-band Frequencies (8.2 to 12.4 GHz) and between 1 and 10 GHz,” *ISIJ Int.*, vol. 51, no. 11, pp. 1766–1772, 2011.
- [25] M. F. Modest, “Radiative Property Predictions From Electromagnetic Wave Theory,” *Radiat. Heat Transf.*, pp. 31–60, 2013.
- [26] Y. K. Gaudy and S. Haussener, “Utilizing modeling, experiments, and statistics for the analysis of water-splitting photoelectrodes,” *J. Mater. Chem. A*, vol. 4, no. 8, pp. 3100–3114, 2016.

- [27] R. Dewan, M. Marinkovic, R. Noriega, S. Phadke, A. Salleo, and D. Knipp, "Light trapping in thin-film silicon solar cells with submicron surface texture," *Opt. Express*, vol. 17, no. 25, p. 23058, 2009.
- [28] G. M. Hale and M. R. Querry, "Optical Constants of Water in the 200-nm to 200- μ m Wavelength Region," *Appl. Opt.*, vol. 12, no. 3, p. 555, 1973.
- [29] W. S. M. Werner, K. Glantschnig, and C. Ambrosch-Draxl, "Optical constants and inelastic electron-scattering data for 17 elemental metals," *J. Phys. Chem. Ref. Data*, vol. 38, no. 4, pp. 1013–1092, 2009.
- [30] A. Ciesielski, L. Skowronski, M. Trzcinski, and T. Szoplik, "Controlling the optical parameters of self-assembled silver films with wetting layers and annealing," *Appl. Surf. Sci.*, vol. 421, pp. 349–356, 2017.
- [31] N. Yatom, O. Neufeld, and M. Caspary Toroker, "Toward Settling the Debate on the Role of Fe₂O₃ Surface States for Water Splitting," *J. Phys. Chem. C*, vol. 119, no. 44, pp. 24789–24795, 2015.
- [32] M. J. Madou, *Fundamentals of microfabrication and nanotechnology*, Third ed. Boca Raton: CRC, 2012.
- [33] M. Ahmed and D. P. Butler, "Flexible substrate and release layer for flexible MEMS devices," *J. Vac. Sci. Technol. B Microelectron. Nanom. Struct.*, vol. 31, no. 5, p. 050602, 2013.
- [34] A. Georgiev, D. Dimov, E. Spassova, J. Assa, P. Dineff, and G. Danev, "Chemical and Physical Properties of Polyimides: Biomedical and Engineering Applications," in *High Performance Polymers - Polyimides Based - From Chemistry to Applications*, M. J. M. Abadie, Ed. InTech, 2012.
- [35] J. D. Benck, B. a. Pinaud, Y. Gorlin, and T. F. Jaramillo, "Substrate Selection for Fundamental Studies of Electrocatalysts and Photoelectrodes: Inert Potential Windows in Acidic, Neutral, and Basic Electrolyte," *PLoS One*, vol. 9, no. 10, p. e107942, 2014.
- [36] A. B. F. Martinson *et al.*, "Atomic layer deposition of Fe₂O₃ using ferrocene and ozone," *J. Phys. Chem. C*, vol. 115, no. 10, pp. 4333–4339, 2011.
- [37] S. H. Yang, D. M. Lee, J. K. Kim, J. W. Kang, and J. M. Lee, "Enhanced optical and electrical properties of ITO on a PET substrate by hydrogen plasma and HCl treatment," *J. Phys. D. Appl. Phys.*, vol. 46, no. 12, 2013.

Conclusions and Prospects

In this thesis, the link between the morphology and multi-physical transport in (photo-) electrochemical fuel production was investigated. Micro- and nanostructuring of electrode materials is a widely applied strategy to overcome limiting bulk transport properties. However, the concern with changing the morphology is that it may reduce transport limitations of one physical phenomenon at the expense of creating obstacles for another. In order to systematically study the effects of the electrode morphology on the overall device efficiency, numerical and experimental tools were developed and applied to electrodes used in photoelectrochemical water-splitting and electrochemical carbon dioxide reduction.

In this thesis, the first step of each study was to measure and parameterize the morphology of all the electrodes of interest. A great emphasis was put on an accurate digital representation of the morphology to build detailed 2D and 3D models. The governing equations of the essential physics were discretized and the partial differential equations were solved by finite volume or element solvers. Parameter studies of the material properties and the morphology parameters were used to quantify the influence of the morphology on the modeled transport phenomena in the electrode. Transport limitations were identified and either attributed to the morphology or the material bulk properties. Based on those results, design guidelines for the electrode morphology were developed with the aim to improve the device performance. The guidelines provide direction on how to modify the morphology and how to quantify the predicted improvements in fuel production efficiency or selectivity. Moreover, conclusions on ideal material properties and operating conditions were drawn. Based on the improved understanding of how

Conclusions and Prospects

the morphology and multi-physical transport are linked, new concepts of electrode architectures were introduced and experimentally demonstrated.

In the following sections, the conclusions of chapters 2 to 5 will be discussed individually, in addition to the prospects of the developed numerical and experimental tools.

In *Chapter 2*, the characterization of complex, anisotropic electrode morphologies with feature sizes in the micro- and nanometer range was discussed. A particle-based lanthanum titanium oxynitride (LTON) and a ‘cauliflower-like’ structured hematite (α -Fe₂O₃) electrode, both used in solar-driven water-splitting, exhibited highly irregular morphologies that have never been characterized in the fully assembled state. The morphological analysis of building blocks, like a single particle, have been reported, but the modeling of multi-physical transport requires the exact geometry of the electrode for an area of several square micrometers in order to obtain statistically meaningful results. We used a combined experimental-numerical approach in which we obtained the exact structural information of the electrodes by destructive, ex-situ FIB-SEM (focus ion beam scanning electron microscope) tomography. This method was applied for the first time in this field to acquire the morphology of photoelectrodes. We used various computational algorithms to quantify the morphological properties on multiple scales: *i*) the solid phase material distribution along the electrode thickness, specific surface, mean feature dimensions, and film homogeneity on the meso-scale; *ii*) particle shapes, surfaces, volumes and orientations on the micro-scale; and *iii*) nano-pore volumes and orientations on the nano-scale. Advanced segmentation of the tomography data, based on machine learning algorithms that can distinguish between different grey value patterns, led to the identification and localization of the TiO₂ necking phase, which is responsible for the inter-particle majority charge carrier transport in the LTON electrode.

Overall, the FIB-SEM tomography proved to be a suitable method to acquire the morphology of micro- or nanostructured electrodes over the range of micrometers with a resolution as high as 4 x 4 x 4 nm³. Based on the developed protocols for the sample preparation, data acquisition, the post-processing, and segmentation, the method can readily be applied to other structured electrodes used in the (photo-) electrochemical fuel community. LTON connected by multiwall carbon nanotubes and porous Nb₂O₅ films were investigated, but are not discussed in this thesis. The same applies to the numerical tools developed for the meso-scale. The introduced ellipsoid-fitting algorithm is only applicable to particle-based electrodes, and the nano-pore characterization tools were explicitly tailored to the LTON electrode. Preliminary experiments explored the possibility to do energy-dispersive X-ray spectroscopy during the FIB-SEM run, and

acquired 3D elemental maps in the LTON morphology. The gathered information would simplify the segmentation process of any multi-component electrode and improve the understanding of compositional variations within the sample. The material composition could be studied for different electrode synthesis processes, or to investigate degradation after electrochemical measurements.

The acquired LTON morphology was used in *Chapter 3* to characterize the multi-physical transport by direct pore-level simulations. The exact 3D morphological geometry was used to investigate light absorption in the semiconductor and mass transport through the liquid domain (electrolyte) of the LTON particle network. Current densities for front and back illumination were calculated and imposed as a boundary condition at the semiconductor-electrolyte interface. The light absorptance of the LTON film was predicted to be 72.3%, and with the observed loose particle stacking, much thicker films would be required to increase this value substantially. However, this would shift the location of the mean photogeneration rate further away from the FTO back contact and create long transport paths through multiple particles for the electrons. Therefore, new experimental approaches are needed to stack the LTON particles more densely and to guarantee the electron transport to the current collector. From an operational point of view, stronger light absorption close to the FTO back contact can be achieved by the illumination from the back side. Our simulations have shown an increased stacking-density of the LTON particles, and thus a higher generation rate of electron-hole pairs for back illumination at the bottom of the LTON films. However, the gain in efficiency can be reduced by limits in the ion transport through the mesoporous electrode. Therefore, mass transport calculations were conducted on multiple scales, simulating the purely diffusive transport of reactants through the stagnant pore space and correcting the result with a Sherwood correlation in order to take into account the concentration gradients in the macroscopic hydrodynamic boundary layer. The electrode performance, defined as the absorbed-light-to-charge-transfer-rate-conversion (ALCC), was described as a function of the semiconductor and electrolyte material properties. Finally, a correlation was defined that quantified the link between the morphology and the ALCC. Based on this correlation, the conditions at which the performance of the electrode decreased due to mass transport limitations, were quantified and correlated to bulk electrolyte concentrations, and flow conditions of a flow cell setup. Local concentration distributions of OH⁻ ions on the semiconductor-electrolyte interface were quantified for various ALCC values and diffusion coefficients. These results gave a unique insight into the local pH values within the mesoporous electrode. In the regime of limited mass transport, a substantial fraction of the semiconductor-

Conclusions and Prospects

electrolyte surface area was exposed to much more acidic pH values compared to the bulk electrolyte.

It has been demonstrated that the morphological data acquired by FIB-SEM tomography can be discretized and used for finite volume simulations, taking into account the detailed geometry in the micro- and nano-range. Despite the complexity of the morphology, statistically meaningful results for the photogeneration rate distribution in the semiconductor, the ion transport and pH distribution in the electrolyte, as well as tortuosities of the pore space were obtained. The strength of the proposed method lies in the spatial resolution of the calculated local distributions, which cannot be measured experimentally. Based on the local distributions, the heterogeneity in a photoelectrode can be analyzed to design morphologies with a more homogeneous performance (e.g., local current density). The main challenges were the meshing of the complex geometries based on the tomography data, the data management and the convergence control of the calculations. The routines implemented in *Ansys CFX* are robust and can be run on multi-cores. However, limits were reached when introducing new physics in addition to the mass transport. Our calculations could be extended with a more accurate light absorption model, taking into account the scattering effects of the particles. Furthermore, semiconductor physics that describe the minority charge transport, considering recombination in the LTON particles, would allow for the prediction of more accurate photocurrent densities besides the best possible case with an internal quantum efficiency of one. It is advisable to implement those calculations in a modeling environment tailored to incorporate multi-physical phenomena. The unsolved issues are the meshing of the tomography data to make the discretized data compatible with other solvers.

In *Chapter 4*, the mass transport calculations were extended to model multiple species with chemical buffer reactions in the electrolyte and electrochemical reactions at the electrode-electrolyte interface. Electrochemical CO₂ reduction on a mesoporous inverse opal Ag (Ag-IO) electrode in aqueous KHCO₃ solution was studied. As seen in the previous chapter, the strength of transport simulations on an accurate representation of the morphology lies in the detailed, space-resolved quantification of ion concentrations and local current densities. For the LTON electrode, that information was used to predict conditions for which mass transport limitations would reduce the performance of the water-splitting reaction. In the mesoporous Ag electrode, mass transport limitations of individual species can be used to tailor the product selectivity of competing reactions. Thus, understanding the link between morphology and mass transport is essential to optimize the performance of this CO₂ reduction device. As the complexity of the modeled physics was increased, the complexity of the morphology was reduced by modeling an idealized, perfectly periodic, inverse opal geometry. However, this simplification was valid

considering the structural regularity of reported Ag-IO electrodes in the literature. Through the parameterization of the geometry, the morphology could be optimized for a maximum product selectivity of the CO₂ reduction reaction towards CO. We have demonstrated that the dramatic suppression of the undesirable H₂ evolution reaction rate and the promotion of the CO evolution reaction rate, as a function of the roughness factor, can be modeled by an inverse OH⁻ concentration dependency of the H₂ evolution exchange current density and a proportional dependency of the CO evolution exchange current density on the CO₃²⁻ concentration. The model was validated with experimental data from the literature. For a 0.1M KHCO₃ electrolyte, saturated with CO₂, the considered operation conditions for a maximum CO faradaic selectivity were far away from the mass transport limit of CO₂(aq). However, the CO faradaic efficiency of a mesostructured Ag electrode was reduced significantly in the top half of the catalytic film, due to a high mass transport rate. The maximal achievable CO selectivity was dictated by the pore diameter and the film thickness. Both parameters directly influenced the surface area, which was found to be the fundamental property to boost the CO faradaic efficiency. For a mesostructured Ag electrode with a pore diameter of 200 nm, a thickness of at least 10 μm was required to reach a CO selectivity above 90%. Based on the detailed insights from the model, we proposed a strategy to further increase the CO faradaic efficiency by adding an inert diffusion layer on top of the Ag electrode. Depositing a non-catalytic material with the same template morphology on top could increase the CO selectivity from 60% to more than 90% for a given Ag film thickness.

A complete and validated model to predict the product selectivity and CO₂ reduction efficiency on a mesoporous Ag electrode was introduced. Besides the valuable insights into the species concentrations in the pore space, the model was detailed enough to hypothesize about the reaction order of the involved species for the H₂ and CO evolution reactions. Based on a parameter study on the morphology, design guidelines for highly product-selective mesoporous Ag electrodes have been developed. Newly proposed electrode architectures with an additional inert diffusion layer would boost the CO selectivity, while reducing the amount of Ag catalyst needed. Experiments to prove this concept, as well as experimental characterization of the concentration-dependent Butler-Volmer correlations for other catalysts (e.g., Cu), are recommended next steps. The developed model could then be used to optimize multi-layered mesostructured electrode morphologies, where the CO evolution on the Ag surface could be further converted to hydrocarbons on a Cu surface.

In *Chapter 5*, an experimental platform was developed where numerically engineered photoelectrode designs were accurately transferred to the fabrication process. The focus of the study was to enhance light absorption in thin film semiconductors through the geometry of the

Conclusions and Prospects

device. For chemically stable metal-oxides used in photoelectrochemical water-splitting, the scale difference of light absorption length and minority charge carrier collection length is often solved through nanostructuring of the electrode material. However, as seen in the previous chapters, mass transport in the electrolyte or majority charge carrier transport in mesoporous electrodes can be limiting. Further, the surface area is largely increased which leads to higher recombination rates. We followed a fundamentally different route by keeping the semiconductor thin and uniform, but enhanced the light absorption by resonant and geometric light trapping. The approach required a fabrication process with excellent control over the micro-structuring of the electrode in order to benefit from the light trapping strategy. At the same time, it allowed for the numerical optimization of the structure before the electrodes were fabricated. α -Fe₂O₃ films on transparent and reflective current collectors were considered. For normal incident light, resonance modes were predicted, and the optimum α -Fe₂O₃ film thicknesses for a maximum light absorption on a perfect reflective, an Ag and a Pt substrate, were determined. The same multilayer stacks, that were applied to wedge structures, also exhibited a periodic dependency of the absorbed photon flux on the α -Fe₂O₃ film thickness. Geometric light trapping, through the harvest of reflected photons on the flat section between the wedges or the opposite wedge slope, enhanced the maximum absorbed photon flux considerably. For a microstructure with a wedge angle of $\gamma=54^\circ$, and an aspect ratio of $R_w=0.8$, the gain through geometric light trapping on an electrode with a transparent current collector, was in the range of 15-18% compared to a transparent and planar reference configuration. In comparison to the same reference, the first resonance peak for microstructures with a perfect reflective or an Ag layer was increased, due to a combination of resonant and geometric light trapping, by 159% or 220%, respectively. Retrapping of photons was responsible for an increase of 58% or 73%, respectively. Taking into account the short charge carrier collection length in α -Fe₂O₃ by an empirical probability model for the internal quantum efficiency, photocurrent densities at the semiconductor-electrolyte interface were predicted. Under the ideal forward-injection condition, maximum photocurrent densities, normalized by the projected area, of 2.0, 6.0, 5.7, and 3.1 mA/cm² were predicted for microstructured and transparent, perfect reflective, Ag, or Pt current collectors, respectively. For the physical implementation of the micro-patterning, anisotropic etching of silicon in KOH solution was chosen, due to the excellent control over the feature sizes, the high reproducibility rate, as well as the smooth etching surfaces along the crystallographic planes of silicon. The patterned silicon wafers were then used as a master template to fabricate α -Fe₂O₃ photoanodes on a flexible substrate. We successfully demonstrated the fabrication of intact and photoactive anodes. Improved photocurrents were measured for the microstructured electrodes with transparent and reflective current collectors compared to their planar counterparts. However, the

substantial potential in photocurrent gain predicted by the numerical model was not achieved. The main concerns were the homogeneity and photoactivity of the deposited α -Fe₂O₃ films.

A numerical model to predict electromagnetic wave propagation in wedge structured thin film α -Fe₂O₃ photoanodes and an experimental process flows to fabricate such electrodes were developed. This platform builds a strong base for the fabrication of numerically engineered photoelectrode structures in the future. The template-stripping methods have been proven to transfer microstructures onto a flexible substrate. Further work is needed to improve the homogeneity and photoactivity of the α -Fe₂O₃ film. Nevertheless, our developed approach opens the way for new microstructured photoelectrodes fabricated by a wide range of silicon patterning processes. Furthermore, the strategy of a combined resonant and geometric light trapping is not only valid for α -Fe₂O₃, but can be applied to other materials (e.g., BiVO₄, Cu₂O). From an engineering point of view, the flexible nature of the polyimide substrates could be used in innovative ways to improve efficiency. For example, the curvature of a thin film photoelectrode could be adjusted to track the sun.

Overall, the influence of the morphology on the multi-physical transport has been studied in detail for a variety of electrodes used in photoelectrochemical water-splitting or electrochemical CO₂ reduction. The tools developed in this thesis helped to draw essential conclusions and propose design guidelines for structured electrodes with enhanced performance and selectivity. Novel approaches for the fabrication of microstructured photoelectrodes were introduced. They are also thought of as a platform for further development using machine learning or other sophisticated approaches to design the best morphologies for optimum performance.

Curriculum Vitae

Silvan SUTER

PERSONAL INFORMATION silvan.suter.ch@gmail.com
Date of Birth : May 8, 1987
Nationality : Swiss

EDUCATION **Swiss Federal Institute of Technology Lausanne (EPFL), Switzerland** Aug. 2014-
Mar. 2019
Ph.D in Mechanical Engineering, Doctoral Program in Energy

- Linking Morphology and Multi-Physical Transport in Structured Electrodes

Swiss Federal Institute of Technology Zürich (ETHZ), Switzerland Sep 2010 -
Jan 2013
Master of Science in Mechanical Engineering

- Master's Thesis: Pore-engineering to increase performance of solar driven thermochemical energy conversion

Swiss Federal Institute of Technology Zürich (ETHZ), Switzerland Sep 2006 -
June 2009
Bachelor of Science in Mechanical Engineering

JOURNAL PUBLICATIONS

- S. Suter, D. Moreno García, R. Graf and S. Haussener, "Template-Stripped Thin Film Water-Splitting Devices Using Light Trapping," in preparation for submission, Mar 2019.

- S. Suter and S. Haussener, “Optimizing Mesoporous Silver Catalyst for Selective Carbon Dioxide Conversion into Fuels,” in preparation for submission, Feb 2019.
 - S. Suter, M. Cantoni, Y. K. Gaudy, S. Pokrant, and S. Haussener, “Linking morphology and multi-physical transport in structured photoelectrodes,” *Sustain. Energy Fuels*, pp. 2661–2673, 2018.
 - S. Suter, A. Steinfeld, and S. Haussener, “Pore-level engineering of macroporous media for increased performance of solar-driven thermochemical fuel processing,” *Int. J. Heat Mass Transf.*, vol. 78, pp. 688–698, 2014.
 - S. Suter and S. Haussener, “Morphology Engineering of Porous Media for Enhanced Solar Fuel and Power Production,” *Jom*, vol. 65, no. 12, pp. 1702–1709, Oct. 2013.
- INTL .
CONFERENCES
- nanoGe Fall Meeting, Torremolinos, 2018
Oral Presentation: “Linking Morphology and Multi-Physical Transport in Porous Silver Electrodes.”
 - MRS Fall Meeting, Boston, 2017
Oral Presentation: “Linking Morphology and Multi-Physical Transport in Morphologically-Complex Photoelectrodes.”
Poster: “Fabrication of Micropatterned, Flexible, Transparent or Reflective, Thin Film Photoelectrodes via a Template-Stripping Method for Enhanced Light Absorption.”
 - nanoGe Fall Meeting, Barcelona, 2017
Oral Presentation: “Quantitative Structural and Transport Analysis of Morphologically-Complex Photoelectrodes.”
 - nanoGe Fall Meeting, Berlin, 2016
Poster: “Geometrical analysis of morphologically-complex photoelectrodes using focused ion beam nanotomography.”
 - International Solar Fuels Conference, Uppsala, 2016
Poster: “Photoelectrochemical hydrogen evolution at a TiO₂-stabilised silicon cathode.”
- AWARDS
- Hans-Eggenberger-Preis 2013
For the Master’s Thesis: “Pore-Engineering to Increase Performance of Solar Driven Thermochemical Energy Conversion.”
plus Scholarship for Ph.D studies.

